Interdigital Sensors and Transducers

ALEXANDER V. MAMISHEV, MEMBER, IEEE,
KISHORE SUNDARA-RAJAN, STUDENT MEMBER, IEEE, FUMIN YANG, STUDENT MEMBER, IEEE,
YANQING DU, MEMBER, IEEE, AND MARKUS ZAHN, FELLOW, IEEE

Invited Paper

This review paper focuses on interdigital electrodes—a geometric structure encountered in a wide variety of sensor and transducer designs. Physical and chemical principles behind the operation of these devices vary so much across different fields of science and technology that the common features present in all devices are often overlooked. This paper attempts to bring under one umbrella capacitive, inductive, dielectric, piezoacoustic, chemical, biological, and microelectromechanical interdigital sensors and transducers. The paper also provides historical perspective, discusses fabrication techniques, modeling of sensor parameters, application examples, and directions of future research.

Keywords*—Dielectric measurements, interdigital sensors, nondestructive testing (NDT), sensor design, sensor modeling, spectroscopy, surface acoustic waves (SAWs), transducers.*

I. INTRODUCTION

A. Motivation for This Paper

Interdigital electrodes are among the most commonly used periodic electrode structures. Recent advances in such fields as nondestructive testing (NDT), microelectromechanical systems (MEMS), telecommunications, chemical sensing, piezoacoustics, and biotechnology involve interdigital electrodes in very different ways. At the same time, a number of common features are shared among these applications. The purpose of this paper is to outline common features and to highlight the differences of sensor geometry, manufacturing techniques, choice of materials, analytical and numerical modeling, design optimization, system integration, and data analysis. It is difficult and perhaps even excessive to maintain equally deep and comprehensive treatment of all these subjects. Instead, the fringing electric field sensors are given the deepest emphasis in this manuscript. Significant aspects of other types of sensors are discussed, while repetition is avoided. References are provided to major review papers and books in each section devoted to a particular field of interdigital electrode applications, such as dielectric imaging, acoustic sensors, and MEMS.

It is not possible to develop a universal sensor and a universal parameter estimation algorithm that would provide the maximum information about material properties in all applications. Each application requires a judicious choice of sensor design and associated parameter estimation algorithms. As a technical system develops, the requirements for each element become clearer and affect the requirements for each element of the trinity shown in Fig. 1. For example, it may become clear during the development stage that the one-sided access to the material under test (MUT) is not necessary due to the specifics of the manufacturing process. In this case, the electrode layout design should not be limited to interdigital structures only. The dual-sided access has advantages of larger, easily measurable capacitances and a more uniform field distribution. The examples of appropriate matching of sensors and parameter estimation algorithms with different applications are encountered throughout this paper.

B. Terminology

The explosion in the quantity of scientific information has brought its share of confusion to the subject of interdigital sensors. As a result, lack of coordination of research efforts is not uncommon in this field. For example, theoretical

Manuscript received February 16, 2003; revised December 30, 2003. This work was supported in part by the National Science Foundation under CAREER Award 0093716, in part by the Center for Process Analytical Chemistry, in part by the Electric Power Research Institute, in part by the University of Washington Royalty Research Fund, in part by the Link Foundation, in part by the Air Force Office of Sponsored Research, and in part by the American Public Power Association.

A. V. Mamishev, K. Sundara-Rajan, and F. Yang are with the Sensors, Energy, and Automation Laboratory (SEAL), Department of Electrical Engineering, University of Washington, Seattle, WA 98195 USA (e-mail: mamishev@ee.washington.edu; kishore@ee.washington.edu; fuminy@ee.washington.edu).

Y. Du is with Underwriters Laboratories, Santa Clara, CA 95050 USA (e-mail: Yanqing.Du@us.ul.com).

M. Zahn is with the Department of Electrical Engineering and Computer Science, Massachusetts Institute of Technology, Cambridge, MA 02139 USA (e-mail: zahn@mit.edu).

Digital Object Identifier 10.1109/JPROC.2004.826603

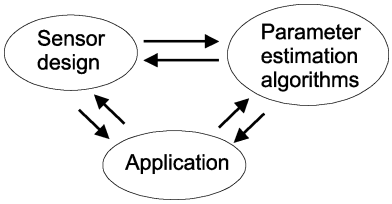

Fig. 1. Every sensing application requires an optimum combination of inherently dependent elements of the measurement system comprising sensor design and parameter estimation algorithms.

expressions obtained for capacitance of interdigital piezoelectric sensors are rarely mentioned in papers published in the fields of dielectrometry or MEMS; researchers in one country are often unaware of efforts in other countries; and sensor designers repeat mistakes of previous generations. Ambiguity of terminology does not help this situation: not everyone associates periodic microstrip electrode structures with interdigital patterns. Moreover, the word "interdigital" itself does not have direct analogs in other languages. Thus, this most frequent term is often replaced by such equivalents as "periodic," "microstrip," "comb," and "grating," as well as such variations as "interdigitated" and "combed." The overlap of the terms is not complete, for example, not every microstrip circuit is interdigital, and not every interdigital circuit is strictly periodic.

The term *interdigital*, selected for use throughout this paper, refers to a digitlike or fingerlike periodic pattern of parallel in-plane electrodes used to build up the capacitance associated with the electric fields that penetrate into the material sample or sensitive coating.

Another term frequently misunderstood in context of interdigital sensors is *wavelength*. One should distinguish between the radiation wavelength of electromagnetic waves and the wavelength of the spatial periodicity, or spatial wavelength, of the geometrical structure. The former is the wavelength λ_e with the frequency equal to the frequency of the voltage source applied to the sensor electrodes

$$\lambda_e = \frac{c}{f} \tag{1}$$

where c is the speed of light and f is the frequency of the voltage source. This variable is typically discussed in context of radio frequency (RF) and microwave circuits. For example, a 600-MHz electromagnetic wave has the wavelength of 50 cm. The spatial wavelength of the periodic interdigital structure is the distance between the centerlines of the adjacent fingers belonging to the same electrode.

Using the terms *capacitance* and *conductance* for the description of terminal characteristics of an interdigital sensor may be misleading, especially when one encounters effective negative values of capacitance or conductance. Strictly speaking, these are mutual capacitance (or *transcapacitance*) and mutual conductance (or *transconductance*), as defined in multielectrode circuits. For the overwhelming majority of cases, this distinction is not important enough to justify the use of longer, more cumbersome terms.

Sensors, *transducers*, and *detectors*, as explained below, are related; hence, these terms are often used interchangeably. The choice of the term usually depends on the function of the device that one wants to emphasize.

A *sensor* is a device whose output can be quantified and changes with one or more physical phenomena. This output information can be used for process monitoring and control. A *transducer* is a device that converts one form of energy into another form. The measurement of physical variables associated with the resulting form of energy allows estimation of the physical variables associated with the input energy. A *detector* is a device indicating presence, absence, or change of the signal qualitatively, either as a binary signal or as a low resolution signal with several states.

C. Historical Perspective

Historically, the first and still the most common reason for making an interdigital electrode structure is to increase the effective length, and, therefore, the capacitance between the electrodes. Perhaps the earliest example of interdigital electrode design is found in the patent of N. Tesla, issued in 1891 [1]. In this example, each "finger" is a rectangular plate, immersed in an insulating liquid. The total capacitance of the "electrical condenser" proposed by Tesla increases approximately linearly with the number of plates. This principle is sometimes used in modern capacitors as well. Theoretical expressions for calculation of capacitance between coplanar strips appeared in the 1920s [2]. Antenna designers use such periodic strip patterns to control the radiation patterns. The technology, later named *microdielectrometry*, started more than 20 years ago as a modification of the charge-flow transistor (CFT), originally developed for monitoring the sheet resistance of thin-film materials [3]. The CFT was an MOS-compatible device based on contemporary principles of transistor electronics [4], [5]. In this device, the time delay between the application of the gate voltage and a complete inversion of the channel region is dependent on the sheet resistance of the MUT. Subsequent experiments demonstrated that bulk conduction effects can be separated from surface conduction. The separation of these two phenomena gave additional valuable insights into the conduction properties of the materials under test. Extensive use of interdigital electrodes for sensing applications started in the 1960s [6] along with other forms of coplanar electrode structures [7]. Later, independent dielectrometry studies with single [3], and multiple [8], [9] penetration depths using interdigital electrodes have continued in several countries. Commercialization of multiple penetration depth dielectrometry in the United States had been initiated in the 1980s and 1990s [10], [11].

The existence of surface acoustic waves (SAWs) in an isotropic material was first demonstrated by Lord Rayleigh in 1885 [12]. SAW technology, as applied to modern electronic systems, arose originally from radar technology. In 1965, White and Voltmer [13] demonstrated the basic SAW delay line structure by depositing two thin-metal interdigital transducers (IDTs) on a polished piezoelectric plate. Until the 1980s, this technology has been mainly used for military

applications. Starting from the 1980s, SAW devices began to be used for consumer electronics and in telecommunications. SAW devices have been made to meet the needs of acoustic filter technology [6], [14] and later spanned fields of communication, signal processing, chemical sensing, nondestructive evaluation, and biomedical applications. Extensive reviews of acoustic sensor technology have been written [15], [16] and somewhat reduce the need for the acoustic sensor technology coverage in this paper.

D. Common Features

One-side access. Several inherent advantages of the planar interdigital geometry attract device designers. One of the most important ones, especially for the NDT sensors and piezoacoustic transducers, is that only a single-side access to the test material is required. One can penetrate the sample with electric, magnetic, or acoustic fields from one side of the sample, leaving the other side open to the environment which can allow absorption of gas, moisture, or chemicals, which can change electrical properties of the MUT. A sensitive layer of chemical or biological nature deposited over the electrodes can also interact with a gas or liquid environment, allowing monitoring of concentration of chemicals in such materials as air, transformer oil, or the human body. In some situations, the other side of the material sample may be too far away or inaccessible due to design limitations for an electrode so that one-sided access is essential.

Control of signal strength. By changing the area of the sensor, the number of fingers, and the spacing between them, one can control the strength of the output signal. A tradeoff between the signal-to-noise ratio and the minimum sensing area is selected based on the application requirements. In microchip sensors, the size of the sensitive area is usually of little consequence, whereas in imaging devices it plays a major role.

Imaging capability. A relatively new field of research is interdigital frequency-wavelength dielectrometry, a close relative of electrical impedance tomography. This technology employs interdigital electrode pairs of variable spatial periodicity. The depth of penetration of quasi-static electric field lines into the material is frequency independent and proportional to the spatial wavelength, defined as the distance between the centerlines of neighboring electrodes of the same polarity. The differing penetration depths of multiple wavelengths make possible spatial profiling of dielectric and conduction properties and geometry of semi-insulating materials. That is, properties of individual layers across the thickness of a stratified medium can be determined without direct access to each layer. Movement of the sensor along the material surface with subsequent signal processing makes possible, in principle, three-dimensional (3-D) imaging of dielectric properties of insulating materials. The dielectric properties can be related to many other physical properties, such as porosity, density, structural integrity, and chemical content of materials under test. At very high radian frequency ω, the skin depth $\delta = \sqrt{2/(\omega\mu\sigma)}$ further limits the penetration of electric and magnetic fields into a medium with conductivity σ and magnetic permeability μ.

Multiple physical effects in the same structure. In addition to sensing applications, fringing electric fields are used increasingly to generate mechanical forces, especially in MEMS. Scaling of motors and actuators to the distances on the order of tens of micrometers make electric fields a feasible choice for actuation of moving parts, whereas magnetic fields dominate the traditional macro scale designs. A strong electric field enhancement at the ends of interdigital electrodes generates a lateral force, which is used for comb displacement. Electrical force levitation is achievable using fringing fields in the direction perpendicular to the interdigital pattern plane.

Simplified modeling. When the aspect ratio of the electrode finger length to the spatial wavelength is large, the numerical simulation and theoretical modeling is greatly simplified because it can be done in the approximate two-dimensional (2-D) limit rather than in 3-D. For this reason, interdigital electrodes are popular when extensive modeling is required for the interpretation of experimental results. For example, elaborate models of electrical or acoustical interactions of interdigital sensors and transducers with stratified media are often developed using 2-D approximations. There is a trend, however, toward full 3-D simulations, taking advantage of continuing dramatic increases in computer speed.

Spectrum. Fig. 2 shows the frequency spectrum for acoustic and electromagnetic phenomena and instrumentation ranges. The lowest frequencies, starting at 1 μHz are used for laboratory measurement of conduction properties, where low-level conduction phenomena are difficult to otherwise measure. The frequencies below 1 Hz are not suitable for real-time industrial monitoring and are used mostly in the laboratory studies of physical phenomena. The characteristics of wave propagation drive the selection of frequency ranges above 1 Hz. Especially significant are such properties as spatial resolution, penetration depth, attenuation, and external interference.

II. Physical Principles

A. Electric Field Sensing

A fringing field dielectrometry sensor has the same principle of operation as the more conventional parallel-plate or coaxial cylinder dielectric sensor cell. The voltage is applied to the electrodes, and the impedance across the electrodes is measured. However, unlike the parallel-plate cell, the fringing field sensor does not require two-sided access to the MUT. Fig. 3 shows a gradual transition from the parallel-plate capacitor to a fringing field capacitor. In all three cases, electric field lines pass through the MUT; therefore, the capacitance and conductance between the two electrodes depends on the material dielectric properties as well as on the electrode and material geometry.

Interdigital dielectrometry is a subset of interdigital electrode sensor applications that relies on direct measurement

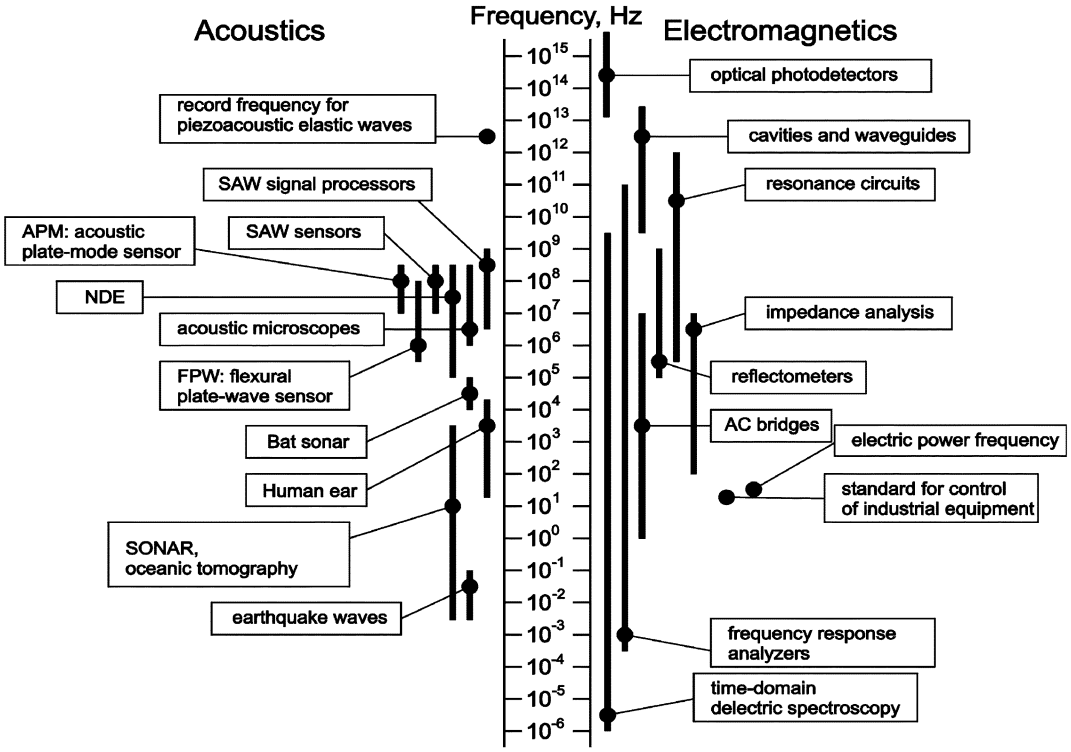

Fig. 2. Frequency spectrum for acoustic and electromagnetic interdigital sensors (partly based on [16], [192], and [193]).

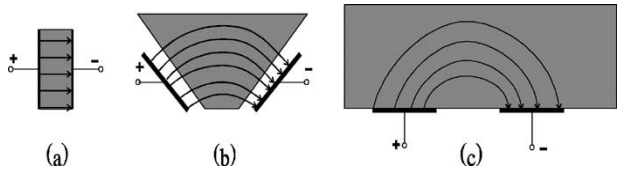

Fig. 3. A fringing field dielectrometry sensor can be visualized as: (a) a parallel-plate capacitor whose (b) electrodes open up to provide (c) a one-sided access to the MUT.

of dielectric properties of insulating and semi-insulating materials from one side [17]–[19]. The basic idea is to apply a spatially periodic electrical potential to the surface of the MUT. The combination of signals produced by variation of the spatial period of the interdigital comb electrodes combined with the variation of electrical excitation frequency potentially provides extensive information about the spatial profiles and dielectric spectroscopy of the MUT. Since the changes in the dielectric properties are usually induced by changes in various physical, chemical, or structural properties of materials, the dielectrometry measurements provide effective means for indirect nondestructive evaluation of vital parameters in a variety of industrial and scientific applications [10], [20].

Usually, the capacitance between two coplanar strips, as shown in Fig. 3(c), is comparable to the stray capacitance of the leads (conductors that connect the electrodes with the electrical excitation source). Therefore, in order to build up an easily measurable electrode structure, the coplanar strip pattern may be repeated many times.

The art and science of designing sensors with multiple interdigital electrode pairs and processing the output signals to gain knowledge about the MUT is the subject of multiwavelength interdigital frequency wavenumber (ω-k) dielectrometry which has been under development for about three decades. The penetration depth of the fringing quasi-static electric fields above the interdigital electrodes is proportional to the spacing between the centerlines of the sensing and the driven fingers and is independent of frequency. Overviews of important concepts related to this technology are available in [11] and [20]–[25].

One of the most attractive features of multiwavelength dielectrometry is the ability to measure complex spatially inhomogeneous distributions of properties from one side. As the complexity of spatial distribution grows and the number of unknown variables in each experiment increases, the parameter estimation algorithms become more complicated, computationally intensive, and less accurate and reliable. Ultimately, every major type of spatial distribution of material properties requires a different parameter estimation algorithm. The types of spatial distributions include, but are not limited to, homogeneous materials, multiple-layer materials, local discontinuities (such as cracks and electrical trees), global discontinuities of microstructure (such as grains or fibers forming the material), and, finally, smoothly varying properties. On the electrical properties side, materials under test may be purely insulating or weakly conductive. Various phenomena may affect sensor response, including frequency dispersion, electrode polarization due to an electrochemical double layer, quality of interfacial contact, and many others.

A conceptual schematic of an ω-k dielectrometry sensor measurement is presented in Fig. 4. For a homogeneous lossy dielectric medium of semi-infinite extent, periodic variation

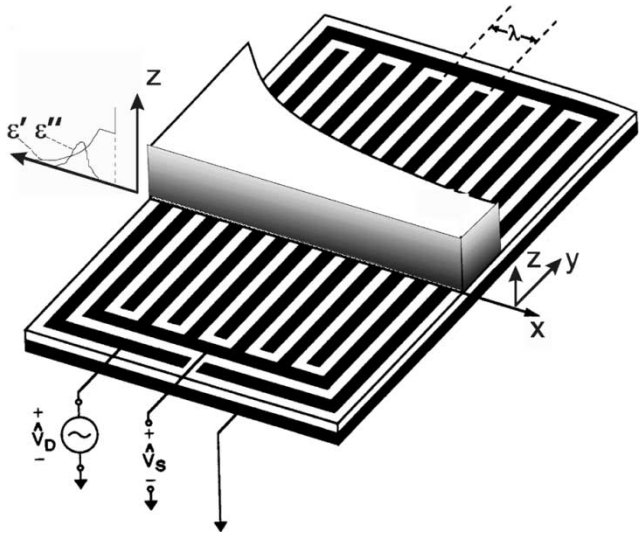

Fig. 4. A generic interdigital dielectrometry sensor [25], [50].

of quasi-static electric potential along the surface in the x direction produces an exponentially decaying pattern of electric fields penetrating into the medium in the z direction. The variation of shade in the MUT indicates the possible variation of material properties and, thus, variations in the complex dielectric permittivity ε^* with the distance z from the surface.

Concepts of the forward and the inverse problems are widely used in the literature related to this technology. Here, the forward problem is defined as the task of determining the electric field distribution and the interelectrode admittance matrix when the geometry, material properties, and external excitations are given. Correspondingly, the inverse problem requires determining either material properties or associated geometry, or both, when the imposed excitations and experimental values of the sensor admittance matrix are available. Each application that involves theoretical modeling usually requires solving the forward problem.

The forward problem can be solved using several approaches. One of them is to use a continuum model [26]. From the electro-quasi-static field point of view, in a homogeneous lossy dielectric, the electric scalar potential of the field excited by the driven electrode is a solution to Laplace's equation. At any constant z position, the electric field distribution far away from the sensor edges is periodic in the x direction and assumed uniform in the y direction. For a homogeneous dielectric of semi-infinite extent, the scalar potential can be written as an infinite series of sinusoidal Fourier modes of fundamental spatial wavelength λ that decays away in the z direction

$$\Phi = \sum_{n=0}^{\infty} \Phi_n e^{-k_n z}(A_n \sin k_n x + B_n \cos k_n x) \qquad (2)$$

where $k_n = 2\pi n/\lambda$ is the wavenumber of each mode. For $e^{\mathrm{j}\omega \mathrm{t}}$ excitations at radian frequency ω, such that $\Phi_n = \Re\{\hat{\Phi}_n e^{\mathrm{j}\omega \mathrm{t}}\}$, the complex surface capacitance density $\hat{C}_n$ relates $\varepsilon^* \hat{E}_{\mathrm{zn}}$ at a planar surface

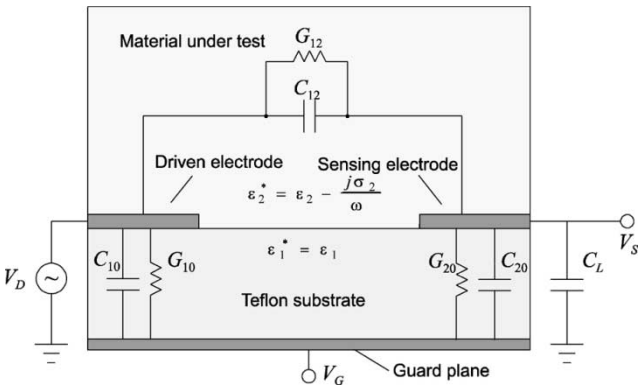

Fig. 5. Half-wavelength cross section with a superimposed equivalent π-circuit model.

$z =$ constant to the potential $\hat{\Phi}_n$ at that surface for the nth Fourier mode of the homogeneous dielectric of semi-infinite extent as

$$\hat{C}_n = \frac{\varepsilon^* \hat{E}_{\mathrm{zn}}}{\hat{\Phi}_n} \qquad (3)$$

where

$$\varepsilon^* = \varepsilon - j\left(\frac{\sigma}{\omega}\right) \qquad (4)$$

is the complex permittivity with ε as material dielectric permittivity and σ as ohmic conductivity. Then, knowledge of $\hat{C}_n$ at the electrode surface lets us calculate the terminal current from the potential distribution at that surface. It is also possible to solve the forward problem with commercial finite-element software [27], with finite-difference techniques, or by using analytical approximations [28].

Fig. 5 shows the equivalent circuit of the sensor superimposed onto the schematic view of a sensor half-wavelength. Note that each wavelength has an opposite conducting guard plane at the bottom of the substrate. For each wavelength, a follower op-amp drives the guard plane at the substrate bottom at the voltage $V_G = V_S$, thus eliminating any current between the sensing and guard electrodes through the substrate. Therefore, the effect of G_{20} and C_{20} on circuit response is eliminated, which simplifies response analysis and improves device sensitivity.

The concept of imposed frequency wavenumber (ω-k) goes beyond dielectrometry applications. Earlier studies led by J. R. Melcher employed interdigital electrodes to study electrohydrodynamic surface waves and instabilities [29], effects on static electrification in insulating liquids [30], [31], and electromechanics of electrochemical double layers in liquid electrolytes [32].

The penetration depth of the fringing electric fields above the interdigital electrodes is proportional to the spacing $\lambda/2$ between the centerlines of the sensing and the driven fingers. Fig. 6 illustrates the idea of multiple penetration depths for a three-wavelength sensor. The variation of the material properties across the thickness of the MUT in the z direction can be approximately found by simultaneously solving three complex equations describing this three-wavelength experimental arrangement as a piecewise three-layer system.

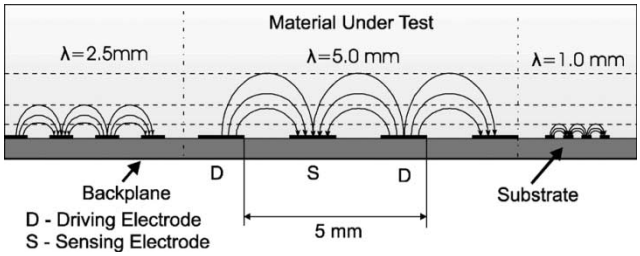

Fig. 6. A conceptual view of multiwavelength dielectrometry. The penetration depth of electric field lines is proportional to the electrode spatial period λ.

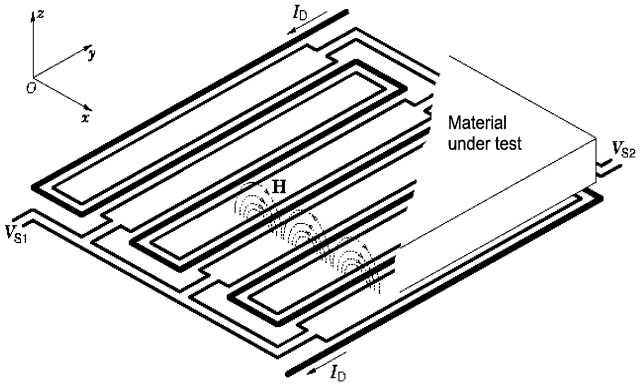

Fig. 7. A meandering winding magnetometer is a magneto-quasi-static field sensor analogous to fringing electric field sensors for measuring high conductivity and/or magnetic materials [36].

B. Magnetic Field Sensing

Low-frequency interdigital sensors that measure capacitance and conductance operate in the region of electro-quasi-static approximation to Maxwell equations. Worth mentioning is a magneto-quasi-static analog of these sensors, most frequently called meandering winding magnetometers [9], [10], [33]–[36]. Fig. 7 shows a generic architecture of this type of sensors. The interdigital pattern is taken by the insulating substrate and windings rather than by conducting electrodes. When electric current passes through the windings, it induces eddy currents in the conducting MUT. Variation of material properties results in the change of mutual inductance between secondary and primary windings. The secondary winding voltage is given by the time rate of change of magnetic flux passing through the secondary winding from the current in the primary winding. At low frequencies, the induced voltage can become very small. To overcome this low-frequency limitation, one can replace the secondary winding with a magnetoresistive sensor that can operate at very low frequencies, down to dc. Operation at low frequencies is required when testing materials for deeply buried flaws, which are otherwise hidden by the skin-depth decay [37]. Similarly to their capacitive analogs, magnetometry sensors can be used as spectroscopy devices, because the frequency of ac current can be varied with the external source. A combined use of magnetometry and dielectrometry sensors for detection landmines is discussed in [34]. The sensor fusion approach allows detection of high metal content, low metal content, and nonmetal landmines.

C. Acoustic Sensing

Piezoacoustic IDTs are a key component of SAW devices, which are most frequently used for measurement of material properties and signal processing [38]. Several books contain chapters dedicated to SAW devices that use interdigital structures [39]–[42].

1) Properties of SAWs: The most important and attractive property of a SAW is associated with the confinement of acoustic energy near the surface of a solid. This implies that the wave can be tapped or modified when it is propagating on the solid surface. High versatility can be achieved because of this feature. Another important property of the SAW is its extremely low velocity, about 10^{-5} times that of electromagnetic waves [41]. This property makes an acoustic wave structure ideal for long delay lines. Because of this low velocity, acoustic waves have very small wavelengths, which offer dramatic reductions in the size of SAW devices. Also, SAWs have low loss during propagation.

2) SAW Devices: IDTs are the building blocks of surface wave filters. Normally, two IDTs are used to build a SAW sensor. One IDT is photodeposited on the highly polished surface of a precisely oriented piezoelectric crystal. When a voltage is applied to the contact pads, an electric field distribution is established between spatially periodic electrodes. Because of the piezoelectric effect, an elastic strain distribution with periodicity is generated. The transducer operates with the highest efficiency when the excitation frequency is such that the physical distance between alternate lines corresponds to the wavelength of the surface wave. The SAW propagates in two opposite directions because of the symmetric structure of IDTs. A second IDT is deposited on the other end of the substrate to detect the SAWs. Detection occurs through inverse piezoelectric coupling. RF signals are generated at the output of the second IDT. Acoustic terminations are designed at each end of the substrate to absorb the bidirectionally launched surface wave.

The frequency, bandwidth, and time response of the IDT are variables that can be controlled by the number of finger electrode pairs in both transducers, the distance between the generating and receiving transducers, the overlap region of the fingers, and the width and spacing of adjacent fingers [43]. The frequency range of operation of SAW transducers is between 50 MHz and several GHz [44]. The velocity of these waves depends on the dielectric and mechanical properties of the MUT. The phase shift ϕ of the transducer signal is

$$\phi = \omega \frac{L}{v} \tag{5}$$

where v is the wave speed, ω is the frequency of excitation, and L is the length of the transducer. Normally, the electroacoustic wave propagation characteristics are only weakly influenced by the dielectric properties of the sensitive layer or MUT [45].

The most common IDT is a uniform IDT, whose finger length and overlap of finger projections onto a line parallel to the each finger do not vary. When a SAW sensor is used for bandpass filters and pulse compression filters,

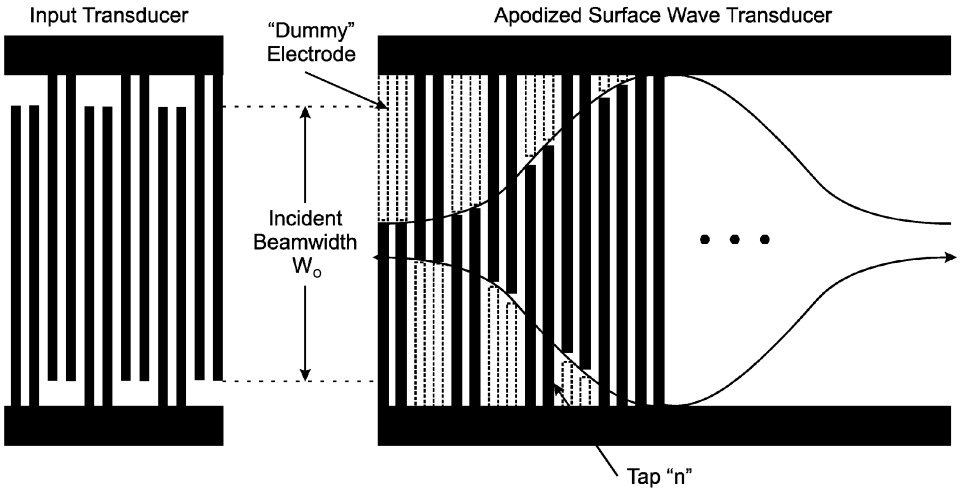

Fig. 8. Typical filter geometry employing one apodized and one uniform transducer [41].

the structure is nonuniform—the finger projection overlap varies. This structure change is called apodization. When an impulse voltage is applied to the apodized transducer, a group of generated SAWs propagate along the substrate, following the outline of the finger projection overlap. At the receiving transducer, each waveform generates a voltage corresponding to the overlap. An apodized transducer increases the versatility of the SAW device, since it allows the synthesis of a diversity of sophisticated filters. Also, the customization of electrode configuration can provide a desired transfer function for a SAW device.

The usage of apodized transducers causes the problem of decreasing surface wave velocity with propagation through metal electrodes. Let us consider the electrodes indicated by solid bars in the long transducer in Fig. 8. The surface wave propagating along the middle of this transducer crosses more electrodes, so it is slowed much more than a wave propagating closer to the contact pads. Severe distortion of the wave profile takes place after it propagates through the apodized transducer. "Dummy" electrodes are sometimes utilized for the remedy of this problem, which is shown in Fig. 8 by the dashed bars. This kind of electrode does not affect the electrical properties of the transducer, but makes the SAW velocity remain uniform when propagating through transducer electrodes.

III. Sensor Fabrication

A. Substrates

1) Physical Properties:

Flexible versus rigid. The choice of substrate thickness and the degree of substrate flexibility depends on the application. Flexible substrates with thin electrodes are advantageous when the sensor head is expected to conform to the surface of the MUT. Representative applications of such a design include measurements performed at an airfoil surface, turbine blades, aircraft rotor blades [46], and curved transformer pressboard insulation [47].

On the other hand, rigid substrates or rigid electrode designs are advantageous in noncontact measurements. In this case, it is important to maintain a well-defined geometry of the electrode structure in order to be able to take advantage of model-based parameter estimation algorithms.

Hydrophilic versus hydrophobic. Direct measurement of moisture or other material properties in the bulk of material typically suggests use of hydrophobic substrates, especially for imaging applications. Absorption of moisture by the substrate is undesirable because it adds another disturbance factor to measurements. On the other hand, measurements of moisture in liquid materials are often accomplished through the use of a hydrophilic substrate and by correlating the change of substrate properties with the change of material properties. This method adds delay to measurements because the substrate and the MUT must be in equilibrium to achieve correct readings.

2) Centimeter and Millimeter Scale Substrates:

Kapton. Polyimide is a frequent choice of the sensor substrate, especially for flexible sensor heads. Polyimides are omnipresent in the modern printed circuit board industry. The manufacturing techniques for them are well developed, and their properties have been investigated under many different conditions and reported in a large number of publications. Examples of designs and use of sensors manufactured with polyimide substrates are reported in [19], [25], and [48]–[51].

Polyimide sensors can operate in temperatures up to 350 °C, which makes them an attractive choice for a power transformer environment where operating temperatures reach 100 °C [52]. Polyimide is a slightly hydrophilic material, being able to absorb moisture up to 3% of its dry weight [24], [50]. Because of the high dielectric permittivity of water ($\varepsilon_r \approx 80$) in comparison with the dielectric permittivity of dry polyimide ($\varepsilon_r \approx 3$), even relatively small amounts of water increase the dielectric permittivity of polyimide by as much as 30% [53], [54]. Table 1 shows the variation of the electrical properties of Kapton with relative humidity at room temperature, assuming that the material has been allowed enough time to achieve moisture concentration equilibrium with the ambient environment. For calculations involving absolute water content at room

Table 1
Relative Humidity Versus Electrical Properties of Kapton at Room Temperature at 1 kHz. Type HN Film, 25 μm (1 mil) [53]

Relative Humidity, %	Dielectric Strength, AC, (kV/mm)	Dielectric Constant, ε_r	Dissipation Factor, tan δ
0	339	3.0	0.0015
30	315	3.3	0.0017
50	303	3.5	0.0020
80	280	3.7	0.0027
100	268	3.8	0.0035

Table 2
CuFlon Microwave Substrate Data Sheet [59]

Property	Units	Typical Value	Test Method
Relative Dielectric Constant, 18 GHz	-	2.10	ASTM D 3380
Dissipation Factor, 18 GHz	-	.00045	ASTM D 3380
Dielectric Strength, 5 mils	V/mil	2000	ASTM D 149
Volume Resistivity (ρ)	ohm-cm	$1 \cdot 10^{16}$	ASTM D 257
Tensile Strength	psi	3500	ASTM D638
Peel Strength	lb/in	8	MIL-S-13949
Water Absorption, 24hrs @ 23°C	%	< .01%	ASTM D 570
Coefficient of Thermal Expansion	ppm/°C	129	ASTM E 831

temperature, 50% relative humidity in this study is equal to 1.8% water by weight in the Kapton film and 100% relative humidity is equal to 2.8% water by weight, the maximum room temperature adsorption possible regardless of the driving force.

The hydrophilic nature of polyimides can be used for the detection of moisture. A number of studies reported successful results with capacitive humidity sensors that use polyimide as a sensitive substrate [55]–[58]. Commercial sensors are available for measurement of moisture in air, transformer oil, and gasoline. For dielectrometry studies, a hydrophilic substrate material like Kapton is often undesirable because the substrate dielectric properties change with ambient humidity and temperature.

Teflon. Polyflon manufactures copper-clad polytetrafluoroethylene (PTFE) substrates, including CuFlon, using a proprietary electroplating process to produce a metal-coated dielectric substrate with exceptional insulation and hydrophobic characteristics [59]. Representative properties are listed in Table 2. This process ensures a strong molecular bond between the PTFE dielectric and the conductive metal layer. Electroplated PTFE withstands continuous temperatures of 175 °C and 225 °C short term without damage to the plated material, dielectric, or the bond between them. Electroplated PTFE also performs well at low temperatures, even under cryogenic conditions. Unlike hydrophilic Kapton, hydrophobic Teflon substrate dielectrometry sensors have been developed which avoid changes in dielectric properties as ambient humidity changes.

Standard thickness of boards available from Polyflon in mils are 0.25 to 5 mils for a standard sheet size of 9 in by 9 in and 10 to 125 mils for standard sheet sizes of 12 in by 18 in.

Kapton/Teflon combination. DuPont has recently introduced a new type of insulating substrate for flexible circuits, Kapton Type FN. In this product, a thin layer Kapton film is sandwiched between Teflon fluorinated ethylene propylene (FEP) fluorocarbon resin coatings. The Kapton core provides mechanical strength and improves thermal stability, whereas the hydrophobic Teflon layers prevent moisture absorption by the Kapton film. Potentially, this material could be used in dielectric sensing applications without fear of measurement results being contaminated by moisture absorption.

G10 board. A regular fiberglass circuit board used for most electronic applications is suitable for dielectrometry sensor heads when a rigid design is advantageous and the low-frequency losses are not of concern. Since masking and patterning of regular circuit boards is most economical in an industrial environment, it can be used for rapid prototype development. The G10 circuit board has proven to be too conductive as a substrate for our dielectrometry measurements.

Conductive polymers. Polymers are organic macromolecules that exist in nature (e.g., in rubber) and can be also manufactured. Conductive polymers were discovered fairly recently, and quickly received attention due to their tunable characteristics and application potential in many technological areas. As far as sensor substrates are concerned, there are two major approaches in forming them. In one, the entire bulk of the polymer is conductive, while in the other, the conductive coating is applied to a nonconducting substrate. The bulk of the polymeric substrate can be made conductive by introducing carbon fibers [60], doping, and addition of other conducting materials [61]. To obtain a conductive coating on a polymer substrate, metal alloys such as tin oxide (SnO_2) [62], zinc oxide (ZnO) [62], and indium tin oxide (ITO) [63] are sputtered or plasma deposited. The coating is then patterned using standard etching techniques to form electrodes of desired dimensions. Polymer substrates are flexible and, hence, can be molded to conform to any curved or irregular surface.

3) Acoustic Substrates: The substrates used in acoustic sensors are primarily piezoelectric materials. Piezoelectric materials are those which, when subjected to physical deformation, generate surface charges proportional to the applied mechanical stress. When centrosymmetric materials, such as silicon and germanium, are strained, the centers of the positive and negative charges do not move with respect to each other, thus preventing the formation of dipoles, a prerequisite for piezoelectricity. The III-V and II-VI compounds, such as gallium arsenide (GaAs), cadmium sulphide (CdS), and zinc oxide (ZnO), have partly covalent bonds and are partly ionic in nature and, hence, are good choices for use as acoustic substrates [64]. Quartz (SiO_2) [65], lithium tantalate ($LiTaO_3$) [66], lithium niobate ($LiNbO_3$) [66], [67], ferroelectric lead [plumbum (Pb)] zirconate titanate (PZT) [68], and polyvinylidene fluoride (PVDF) [69] are the most commonly used acoustic substrates.

Quartz. Quartz is a mineral composed of SiO_2. The structure of quartz consists of helical chains of silicon tetrahedrons. The chains are aligned along the C axis of the crystal and interconnected to two other chains at each tetrahedron making quartz a true tectosilicate. The most prominent acoustic quality of quartz is the dependence of the temperature coefficient of quartz on the cut angle and the direction of wave propagation [65]. With proper selection, it is possible to minimize or maximize the first order effects of temperature. A quartz substrate with Y, X orientation

has a temperature coefficient of -24 ppm/°C, while that for ST-cut quartz is 0 ppm/°C. Hence, an acoustic wave temperature sensor would use a quartz substrate with a Y, X orientation, while a mass sensor would use a ST-cut quartz substrate to eliminate the effect of temperature.

PVDF. PVDF, commercially known as Kynar, was the first piezopolymer to be discovered that exhibited strong piezoelectric effect [69]. PVDF is a semicrystalline polymer consisting of long-chain molecules with the repeat unit CF_2-CH_2, which has a relatively strong dipole moment. At present, there are four known crystalline forms of PVDF, of which three are polar [70]. A PVDF film by its nature has a random distribution of crystallite orientation and, hence, does not have a net polarization. However, the material can be made to exhibit net polarization by a number of physical and chemical processes such as direct application of high electric fields, corona charging, and by stretching the film uniaxially prior to poling [70].

PZT. PZT ceramics, close to the morphotropic phase boundary, exhibit excellent dielectric and piezoelectric properties [68]. It is the most commonly used ceramic piezoelectric substrate. Reference [71] discusses in detail the properties of PZT and other ceramic piezoelectric substrates. The major disadvantages of PZT are relatively low mechanical properties, temperature dependence, and exhibition of aging when approaching the Curie temperature [72]. Recently, PZT doped with ZrO_2 [73], Ag [74], and oxides [68] have been investigated and shown to exhibit better material properties.

4) Microtechnology Substrates: Numerous authoritative references offer a comprehensive treatment of microtechnology substrates. Reference [64] details the qualities of substrates used for different kinds of transducers. Reference [72] offers encyclopedic description of individual substrate materials.

Common materials in the semiconductor industry, oxidized silicon and silicon nitride, are frequent choices for microsensors and on-chip sensor arrays. The resistivity of high-quality silicon dioxide exceeds 10^{14} Ohm · cm. The details of manufacturing of interdigital sensors with a silicon dioxide substrate are described in [75].

Many other substrate materials are becoming available as the semiconductor industry, polymer industry, and basic chemical engineering and materials science research adopt new technologies, such as Si, Ge, SiGe, SiC, GaP, InP, and AlN. A separate paper could be written to cover every major possible substrate material, and it would become outdated within a few years. We would like to mention one particularly promising chemical sensor material: aluminum oxide. Thick-film printing on Al_2O_3 with gold electrodes is an inexpensive conventional process well suited for manufacturing of chemical gas sensors [76].

Borosilicate glass substrate [77] and silica glass substrate [45] are common materials in thin-film technology. Often, there is a strong correlation between surface condition properties and sensor response. For measurements with highly insulating materials, the surface conductivity control is extremely important. Contaminated surface conditions can be detected by measurements in dry air or vacuum, prior to application of the sensor to the surface of the MUT. Organic contaminants can be removed from the glass surface using acid based cleaners, such as "piranha" ($3:1$, H_2SO_4:H_2O_2) [77].

The glass substrate can be made hydrophobic by immersing into octadecyltriethoxysilane–benzene solution [78]. Usually the glass substrates are brittle, which makes them unsuitable for those applications where conformity to the sample surface is essential. However, these substrates perform very well in fluid environments.

Table 3
Typical Electrical Properties of Parylene [194]

	Parylene N	Parylene C	Parylene D
Dielectric strength, short time, volts/mil at 1 mil	7,000	5,600	5,500
Volume Resistivity, 23ºC, 50% RH, ohm·cm	$1{\cdot}10^{17}$	$6{\cdot}10^{16}$	$2{\cdot}10^{16}$
Surface Resistivity, 23ºC, 50% RH, ohms	$1{\cdot}10^{13}$	$1{\cdot}10^{14}$	$5{\cdot}10^{16}$
Dielectric constant			
60 Hz	2.65	3.15	2.84
1 kHz	2.65	3.10	2.82
1 kHz	2.65	2.95	2.80
Dissipation factor			
60 Hz	0.0002	0.020	0.004
1 kHz	0.0002	0.019	0.003
1 MHz	0.0006	0.013	0.002

B. Coatings

General requirements. The sensor coating or the substrate itself can be used as a selective sensitive layer that responds to the changes in the concentration of certain specific types of molecules and ions present in the ambient fluid through adsorption and absorption processes, possibly combined with diffusion and mass transfer.

The reversibility of sensor response is of major concern when the sensitive layer or substrate is used for augmentation of signal strength. Irreversible changes, sometimes referred to as film poisoning [79] reduce sensor lifetime and reliability. In some cases, recycling of previously used sensors is possible by vacuum, temperature, or chemical [80] treatment.

Parylene coating. Parylene is a generic name for members of a specific polymer series. The basic member of the series, called parylene N, is poly-p-xylylene, a completely linear, highly crystalline material. Parylene C, the second member of the series, is produced by the same monomer modified only by the substitution of a chlorine atom for one of the aromatic hydrogen atoms. The third member of the series is parylene D and contains two chlorine atoms on the benzene ring [81].

Parylene N is a primary dielectric, exhibiting a very low dissipation factor, high dielectric strength, and a dielectric constant invariant with frequency. Parylene C has a useful combination of electrical and physical properties plus a very low permeability to moisture and other corrosive substances (see Table 3). Along with its ability to provide a true pinhole-free conformal insulation, parylene C is the material of choice for the coating of critical electronic assemblies. Parylene D forms the hardest surface, and it has the least

elongation ability and the greatest temperature stability. Its molecular structure also gives it the best chemical resistance. Due to the uniqueness of the vapor phase deposition, the parylene polymers can be formed as structurally continuous films from 100 nm to 1 mm.

Parylene is expected to survive continuous exposure to air at 100 °C for ten years. In inert atmospheres or in vacuum, Parylene is expected to withstand continuous exposure at 220 °C for ten years.

Most conformal coatings on the macro scale are sprayed or dipped and have a tendency to pull away from edges, bridge components, or wick into unwanted locales. Parylene deposits void free and pinhole free. It does not edge, bridge, or gap, and because the vapor deposition process is not line of sight, everything within the chamber gets coated uniformly. Kapton substrate dielectrometry sensors were coated with parylene to prevent moisture diffusion into the Kapton that would change its dielectric properties [50].

Hydrogels. Highly hydrophilic polymer gels (hydrogels) have been used as the sensitive layer for a conductimetric interdigital microsensor [82]. In this case, the hydrogel itself has to be characterized by its water content, which may vary from 30% to 99% by mass. Hydrogels undergo reversible swelling with moisture uptake, so that conductivity and linear dimensions of the layer change during the experiment. Due to an increasing use of such materials for medical and biological applications, *in vivo* applications of auxiliary interdigital sensors for biological and chemical parameter monitoring are of great potential interest.

Other materials. Numerous advanced sensing applications are based on the use of so-called smart materials, applied to the sensor surface as an active coating. Such coatings change material properties, geometry, mechanical, or electromagnetic characteristics in response to changes in the environment [83]. A few examples are listed below.

Semiconductive thin films based on ZnO_x were used to detect the presence of oxygen in a gas mixture [84]. A sensitive layer of an electron-beam evaporated copper phthalocyanine (CuPc) thin film has been used to detect part-per-billion concentration levels of nitrogen dioxide (NO_2) and diisopropyl methylphosphonate (DIMP) [85]. Another hygroscopic polymer, crosslinked cellulose acetate butyrate (CAB), has been used for humidity sensing [86]. A combination of CuO, $BaTiO_3$, La_2O_3 and $CaCO_3$ has been used to detect CO_2 concentration changes [76]. A frequently used SO_2-sensitive material heteropolysiloxane (NND/PTMS) has been used with great success in combined dielectrometry and piezoacoustic measurements [45] as well as in impedance spectroscopy measurements [87].

Porous cellulose products, such as ethylcellulose, cellulose–acetate, and cellulose–propionate are good sensitive layer candidates for detection of organic compounds (ketones, alkanes, alcohols, and aromatic and chlorinated hydrocarbons) in the gas phase. Absorption of organic molecules changes density and bulk dielectric permittivity that can be detected with microbalance oscillators and interdigital capacitors (IDCs) [88]. Particularly successful experimental results were obtained with ethylcellulose interacting with chloroform, tetrachloromethane, trichloroethylene, tetrachloroethylene, tetrachloroethane, octane, benzene, toluene, and nitrobenzene. Other sensitive low-conduction polymers include polyethylcellulose, polycyanomethylsiloxane, and polyurethane [89].

Increasing success of biotechnology applications is exhibited in a variety of sensor applications. Lipid bilayers, which constitute the basic structure of all biological membranes, have been used to monitor pH changes in surrounding fluids [90]. A thin layer of polypyrrole coating was found to change its conductivity with the concentration of penicillin that affected the pH response of penicillinase membrane [78].

C. Electrodes

The choice of manufacturing technique for electrode fabrication depends on the required feature size of the electrode mask, substrate material properties, and expected environmental working conditions, such as temperature, acidity, pressure, economic factors, and limitations of parameter estimation algorithms. The latter may put restrictions on certain electrode features. For example, the earlier continuum model by Zaretsky and Melcher [25] required the electrodes to be nearly infinitely thin. Later, this model was modified to account for electrode thickness [91]. In general, the entire manufacturing arsenal of the electronics industry is available to the designer at a fairly low cost. Extensive sources dedicated to the description of various manufacturing technologies are available (e.g., [92]). The following selective overview is not intended to cover every manufacturing technique available. Instead, it emphasizes characteristic features of a few commonly used manufacturing technologies that lead to successful designs of interdigital sensors.

Screen printing of electrodes with silver and silver–palladium inks on thick films makes possible deposition of interdigital structures on the MUT. The advantage of this approach is an intimate contact between the electrodes and the substrate, which in this case also serves as a sensitive layer [93]. An electron beam thermal evaporation process followed by a conventional mask etching allows control of both the deposition rate and the thickness of the films [77], [85]. Gold and platinum electrodes normally used in the electronics industry offer the advantage of being inert and flexible [94]. Silver and NiCr electrodes may also be used [90].

Electroplating. Electroplating has been used by Polyflon to deposit a uniform layer of copper on the surface of the Cu-Flon substrate. This proprietary technique involves preprocess surface treatment, and provides uniformity of the copper layer adequate for most applications explored in our laboratory. Additional electroplating with nickel and gold has been used in several cases to prevent corrosion of the electrode surface. The additional thickness due to the gold layer did not exceed 1 μm.

Micrometer and submicrometer technology. Selection of material and fabrication technique of microelectrodes is determined by the required accuracy, overall fabrication

process limitations, and degree of integration between the sensing elements and electronics elements in the same chip package. Most often, the electrodes are formed by patterning sputtered or vaporized metal coatings Al, NiCr, Au [45], [95], and Pt [78]. The spin-coating technique is preferred for formation of very thin layers of material [96]. There are two principal ways to pattern metals: liftoff and etching. In liftoff, a sacrificial layer is first deposited and patterned. The metal is then deposited using sputtering, vaporization, or electroless deposition. When the sacrificial layer is removed, the metal deposited in the exposed area is retained, thus forming patterned electrodes. In the other method, a thin film of metal is deposited followed by a patterned masking layer. The structure is then subjected to an etching process, which removes the metal in the exposed areas. The mask is then stripped, leaving the patterned metal behind. The minimum feature size that can be manufactured is limited by the wavelength of the source used for the lithography step. Electrode widths as small as 24 nm have been reported [97]. Advances in nanotechnology are making fabrication of nanoelectrodes feasible using entirely new methods, for example, through self-assembly and manipulation of nanotubes.

IV. Sensor Design

A. Circuit Design

1) General Principles: Aside from specifying what functions should be performed by the electronic circuitry, one has to select an optimum partitioning between on-board and off-board design [98]. This decision is particularly important for sensors based on semiconductor technology. Signal processing electronics placed in the same housing as the sensing elements offers advantages of removing lead parasitic effects, reducing measurement noise [99], or providing wireless communication with the data acquisition system [100]. The major disadvantage in this case is the increased complexity of chip design and vulnerability of the sensor.

The currents in microdielectrometry measurements can be as low as tens of femtoamperes. At such low levels, the reduction of electrical noise through electromagnetic shielding and digital filtering of the sensor output signal becomes particularly important [101]. A strong dependence of dielectric properties of polyimides on ambient moisture concentration introduces difficulties to some applications of microdielectrometry. The control of ambient moisture may be necessary for achieving reproducible results with sensors that use a Kapton substrate [101]. An extensive review of the dependence of Kapton properties on moisture and ionic contaminants is provided in [102].

A wide class of phenomena is referred to as "history" or "memory" effects in the polymer literature. Sometimes, history effects arise because charge accumulation in a previous experiment can influence the current distribution in subsequent experiments [101].

Under any type of sensor geometric arrangement and electronic control, the dielectric properties of materials are evaluated by measuring terminal quantities defined by an equivalent lumped-element circuit and relating these quantities to the distributions of complex dielectric permittivity. The measurement of profiles of other physical variables, e.g., the distribution of moisture concentration, requires a calibration mapping that relates the complex permittivity to the physical variable. Appropriate choice of measurable quantities may significantly simplify this task. Possible variations of the measurement setup compared here are the following.

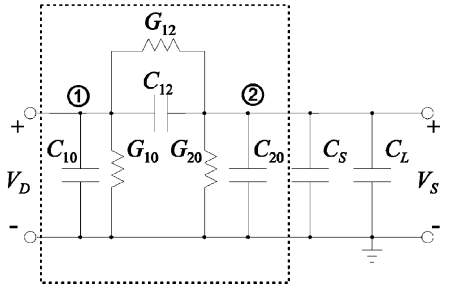

Fig. 9. Floating voltage measurement with a grounded backplane and an impedance divider.

- Floating voltage measurement with backplane held at earth ground potential.
- Floating voltage measurement with backplane and guard fingers (if existing) held at guard potential equal to sensing electrode potential.
- Short-circuit current measurement with backplane and guard fingers (if existing) held at virtual ground potential.
- Combinations of the above three approaches.

The following sections provide a detailed description of the first two, most frequently used, approaches, along with their inherent advantages and disadvantages.

2) Floating Voltage With Ground Plane: The circuit schematic for this measurement mode is presented in Fig. 9. Node 1 corresponds to the driven electrode, and node 2 to the sensing electrode. Basically, an impedance divider is formed by the sensor's equivalent lumped elements and by the known load capacitance C_L. Strictly speaking, the load capacitance is not necessary, since the admittance to the ground plane is connected in parallel. However, it is useful to minimize the effects of the unknown stray capacitance C_S, to optimize the amplitude of the complex gain, and to select the frequency breakpoint between high and low frequency behavior. The complex gain between the driven and the sensing voltage at frequency ω is given by

$$\hat{G}=\frac{\hat{V}_S}{\hat{V}_D}=\frac{G_{12}+j\omega C_{12}}{G_{12}+G_{20}+j\omega(C_{12}+C_{20})+j\omega(C_L+C_S)} \tag{6}$$

where $\hat{V}_S$ is the phasor voltage of the sensing electrode and $\hat{V}_D$ is the phasor voltage of the driven electrode. It should be remembered that elements G_{12}, G_{20}, C_{12}, and C_{20} are frequency dependent, as they represent an equivalent network of distributed elements that differs topologically from the actual sensor. C_S represents the combined effects of the stray capacitance of the sensor leads, gate of the operational amplifier, fringing fields to the surrounding objects, etc. The sum

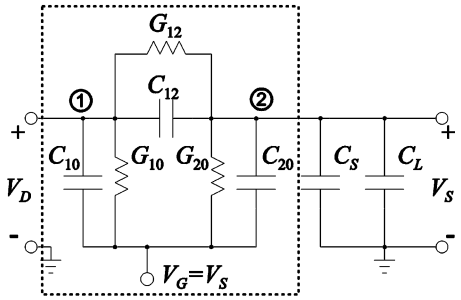

Fig. 10. Floating voltage mode measurement of gain, phase, C_{12}, and G_{12} with actively driven backplane voltage equal to the sensing voltage.

$C_{20} + C_L$ is usually one or two orders of magnitude larger than C_S.

One disadvantage of this measurement approach is that the complex gain values cannot be converted in a straightforward way to the equivalent network element values. One complex equation can be solved for at most two real unknowns, while (6) has four unknowns (G_{12}, G_{20}, C_{12}, and C_{20}) when the complex gain is known from measurements. Even though G_{20} and C_{20} may be predominantly determined by known substrate properties, fringing fields through the unknown material have a significant effect on G_{20} and C_{20}.

A similar argument applies to the high-frequency limit, where equivalent conductance G_{12}, G_{20} can be ignored compared to the imaginary part of all admittances. In this case, only one equation with two unknowns is available

$$G = \frac{V_S}{V_D} = \frac{C_{12}}{C_{12} + C_{20} + C'_L} \tag{7}$$

where the gain G is now real and C_S was incorporated into $C'_L = C_L + C_S$.

Although the number of equations is not sufficient to solve for equivalent capacitances and conductance directly, the solution can be found by iterative solution of the electric potential distribution either by a continuum model or by finite-element techniques. That is, the solution to the inverse problem can still be found by employing two additional implicit functional dependencies $G_{12}(\varepsilon, \sigma, \omega)$ and $C_{12}(\varepsilon, \sigma, \omega)$ obtained from the solution to Laplace's equation for the electric scalar potential. This approach is not necessarily reliable, due to a high sensitivity to error and possible existence of multiple solutions.

One way to simplify the relationships between measurable quantities and equivalent admittance values is to drive the backplane at the same potential as the sensing voltage. A detailed description of this approach follows.

3) Floating Voltage With Guard Plane: When a potential equal to that of the floating sensing electrode is applied to the backplane $V_G = V_S$ as shown in Fig. 10, the equivalent circuit elements G_{20} and C_{20} no longer affect the complex gain of the impedance divider, so that (6) reduces to

$$\hat{G} = \frac{\hat{V}_S}{\hat{V}_D} = \frac{G_{12} + j\omega C_{12}}{G_{12} + j\omega C_{12} + j\omega(C_L + C_S)}. \tag{8}$$

This simplification allows the sequence of the inverse problem solution process to be changed. The equivalent admittance between the driven and sensing electrodes can now easily be found by solving a system of two linear equations with two unknowns. Relating the value of the complex interelectrode admittance to the complex dielectric permittivity ε^* of the tested material can be achieved in several ways, which are discussed in the following sections.

There are several consequences in changing the measurement approach, which affect the design of the sensor. Since the backplane has to be driven at the guard voltage, and this voltage is different for each wavelength, it is no longer possible to have a common backplane, as was implemented in the previous design. This is why the new design has three separate backplanes (shown in gray in Fig. 12). Also, any grounded electrodes, such as a shielding case, must be placed sufficiently far from the sensing electrode, so that the elimination of C_{20} in (8) is valid. In addition, separation of the driven electrode for each of the three wavelengths units is desirable if precise measurements are needed by avoiding cross coupling with other wavelengths. In this case, only one wavelength at a time performs active measurements, and all other wavelengths are held at the guard potential of the active wavelength.

B. Examples of Sensor Head Designs

Dielectrometry applications for imaging or profiling of the MUT typically employ sensors with a small number of fingers, from 2 to 20, because the ultimate penetration depth of the sensor is expected to be of the same order of magnitude as the sensor size. Chemical sensing applications, on the other hand, typically use more fingers, 20 to 200, because the sensing layer can be very thin relative to the sensor size and it is important to build up capacitance to increase the signal magnitude. The following examples focus on profiling applications, as the design of electrode layout is more difficult than in the case of chemical sensors.

1) Three-Wavelength Sensor on a Kapton Substrate: The design of this three-wavelength sensor has been thoroughly described in [20], [49], [50], and [103]. The planar view of this design is shown in Fig. 11. This sensor consists of three sets of copper electrodes on a flexible polyimide substrate (Kapton) with wavelengths of 1.0, 2.5, and 5.0 mm. The sensing electrodes are shielded in the plane of the sensor by guard electrodes driven by a buffer stage in the interface circuit, and the guard electrodes are shielded by ground electrodes. In-plane shielding of the sensor leads is not sufficient when the capacitance C_{12} between the sensing and driven electrodes is relatively low.

A thin passivating layer of parylene (5 μm) covers the sensor on both sides to prevent moisture absorption by the hydrophilic Kapton substrate. In general, the presence of moisture in the volume of a polyimide causes significant variations in its complex dielectric permittivity. A grounded backplane deposited on the bottom side of the substrate provides shielding from external perturbations, defines ground potential, and predominantly confines the electric field to the upper half-space.

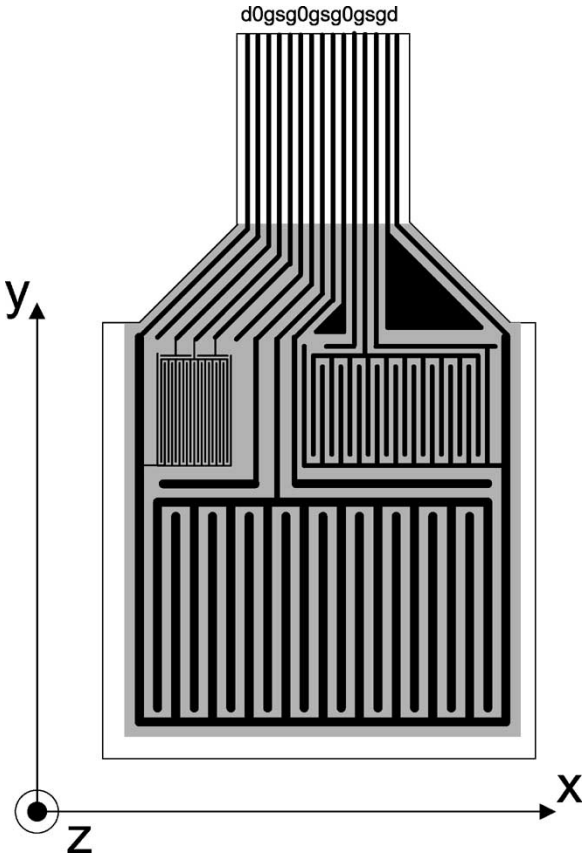

Fig. 11. The three-wavelength Kapton substrate sensor with wavelengths of 1, 2.5, and 5 mm. Legend of electrode contacts: d—driven, 0—ground, g—guard, s—sensing [50].

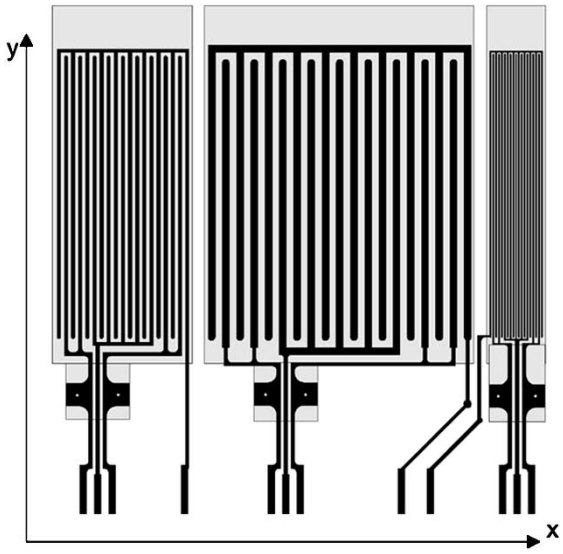

Fig. 12. Improved design of the three-wavelength interdigital sensor over the Kapton sensor of Fig. 11 using a Teflon substrate. Scale 1 : 1. In this design, the finger length to wavelength aspect ratio is increased, the cross coupling between the wavelengths is reduced by moving them farther apart and adding guard electrodes, the infinite periodicity is approximated with guard fingers, and the substrate material was changed from hydrophilic Kapton to hydrophobic Teflon. The three separate guard planes on the back surface replaced the single ground plane in order to facilitate independent measurements of each wavelength.

Table 4
Comparisons of Three-Wavelength Sensor Capacitance Matrix in Air From Fourier Series Continuum Model, Finite-Element Simulation, and Measurements. Capacitances Were Measured by Measuring the Current Between the Pair of Electrodes of Interest While Connecting the Remaining Electrodes in the Guard Mode. The Higher Measured Values are Observed Because the Actual Device Deviated From 50% Metallization Ratio and Because the Lead Capacitance Is Not Taken Into Account in Simulations

	$\lambda = 1.0$ mm		$\lambda = 2.5$ mm		$\lambda = 5.0$ mm	
Capacitance (pF)	C_{20}	C_{12}	C_{20}	C_{12}	C_{20}	C_{12}
Continuum Model	11.8	1.19	24.6	0.54	89.1	0.8
FEM (*Maxwell*)	10.7	1.01	23.4	0.56	88.8	0.8
Direct Measurement	17.1	1.24	32.8	0.67	112.0	0.82

The idealized model, for which closed-form expressions for the electric field exist, requires the electrodes to be modeled as an infinitely long and wide array of zero-height metal microstrips placed on the surface of the insulating substrate. The most important contributors to the discrepancies between the theoretical model and actual measurement data are the finite length and finite number of finger electrodes, the capacitance of the leads of the electrodes to ground and to each other, the metallization ratio (described as the ratio of the area covered with copper to the total area of the sensor, 50% for the sensors in Figs. 5, 11, and 12, and the fluid (typically air or liquid dielectric) trapped between the sensor's surface and the surface of the tested specimen. The finite thickness of the copper electrodes (35 or 17.5 μm for different sensor designs) may also contribute to these differences; however, recent computational models take the thickness of electrodes into account [91].

Comparisons given in Table 4 for the three-wavelength sensor in air demonstrate that although the continuum model of the interdigital sensor is theoretically adequate, the results of actual measurements may differ from predicted values by more than 30%. Several factors contribute to this phenomenon, such as inaccurate estimation of electrode width, nonzero metallization thickness of the electrodes, and, sometimes, poor contact between the materials on the sensor–specimen boundary. The difference for C_{20} is even larger because the driven electrode used for the measurement of C_{12} has additional metallization of the leads, connections between individual fingers, and is strongly affected by inaccuracy in estimation of the metallization ratio.

2) Three-Wavelength Sensor on a Teflon Substrate: The improved design structure of the three-wavelength interdigital sensor used in subsequent experiments is shown in Fig. 12. The major parameters, namely, the number of wavelengths (three) and their spatial periodicities of 1.0, 2.5, and 5.0 mm, were kept the same as in the previous Kapton sensor design. The substrate material was changed from Kapton to Teflon. The superior hydrophobic characteristics of Teflon necessitated this choice, as it eliminated the need of the moisture barrier coating (such as Parylene), although Kapton outperforms Teflon in its thermal endurance and mechanical stability. The recent introduction by DuPont of Kapton-F material, which consists of a Kapton core with a Teflon-like coating, may make it possible to manufacture a sensor on a substrate that combines advantages of both materials.

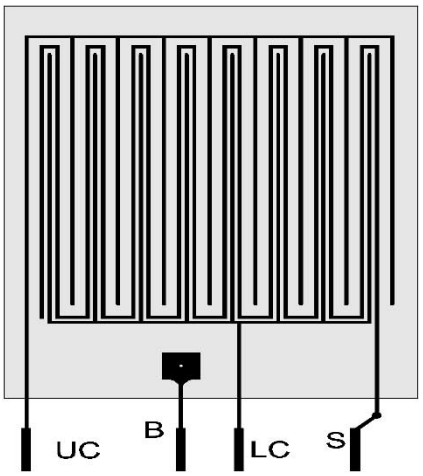

Fig. 13. CSC sensor with 0.5-mm finger width and 6-mm fundamental wavelength. Scale 1:1. Legend: LC—lower comb, UC—upper comb, S—serpentine, B—backplane.

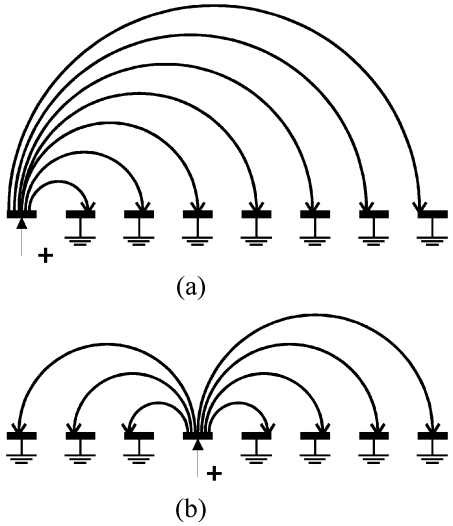

Fig. 14. Schematic excitation patterns for a linear sensor array. (a) The leftmost electrode is excited; the rest are grounded. (b) The fourth electrode from the left is excited; the rest are grounded. (Adapted from [104].)

Guard fingers are introduced on each side of the active sensing area to make the sensor look "infinite" in the x direction. The nominal meander length represents the total length of the capacitor composed of the meandering dielectric path between the sensing and the driven electrodes, which is approximately equal to twice the total length of the sensor electrode fingers. The factor of two is necessary because each electrode forms a capacitor on both sides.

The guard electrodes are also known to be used to minimize stray surface leakage currents [85]. Our application did not require a guard ring covering the entire nonactive area of the substrate, because of the high surface resistance of the Teflon substrate under experimental conditions reported here.

3) Comb–Serpentine–Comb (CSC) Sensor: Multiwavelength interdigital dielectrometry is highly susceptible to the quality of contact between the sensor and the MUT. It has been determined that the change of capacitance due to the contact quality is far more significant than the change due to the finite thickness of the electrodes. Numerical simulations and measurements with the sensor shown in Fig. 12 demonstrated that the equivalent air gap has to be as high as 20 to 50 μm in order to produce the reduction in the capacitance indicated by differences between the theoretical and the measured values.

This problem is known to exist in many fields, including the usage of ultrasonic transducers, eddy current sensors, high voltage electrodes, and magnetometry sensors. Experience from other fields of engineering shows that it is unlikely to completely eliminate the microgaps that form between the sensor electrodes and the MUT. Techniques to reduce the error introduced by the microgaps include increase of the contact force, using a flexible substrate and/or rubber padding, allowing a uniform period for mechanical relaxation, and statistical analysis.

Fig. 13 shows the conceptual picture of one alternative design. The arrangement of the electrodes shown in this diagram allows connection of excitation and measurement circuits of the interface box to the electrodes using only single plane connections. That is, there is no need to drill holes through the substrate except for the ground/guard backplane hookup. Each wavelength sees the same dielectric circuit under test rather than for the three independent wavelength sensors in Figs. 11 and 12, which measure different dielectric regions.

Ideally, the interface circuit should provide independent switching for each electrode, so that each electrode can serve in the capacity of the driven, sensing, or guard electrode. Each penetration depth requires a unique combination of these roles. For each measurement, one of the electrodes is driven, one is sensing, and one is guard. This type of switching is quite cumbersome for highly insulating measurements, because a large number of reed relays would have to be employed. However, for the measurements at higher frequency, solid-state switches can be used, which would significantly simplify the design of the interface circuit. Two wavelengths, rather than one wavelength, would detect any discontinuity, such as the presence of a dust particle several micrometers in diameter.

4) Capacitive Sensor Arrays: Naturally, the shape of coplanar microstrips does not have to be limited to pairs of interdigital combs. In fact, any pair of coplanar electrodes can be used to generate fringing electric fields. Provided that the measurement sensitivity is adequate, the information about material properties can be extracted from such measurements. A simple example, extracted from [104], is shown in Fig. 14. The excitation of one of the electrodes of the capacitive array produces fringing field patterns that contribute to capacitance matrix entries associated with the given array. The total number M of independent two-electrode measurements is

$$M = \frac{N(N-1)}{2} \tag{9}$$

where N is the number of electrodes in the array. For example, the three-sensor system allows three independent measurements, and the eight-sensor system allows 28 independent measurements.

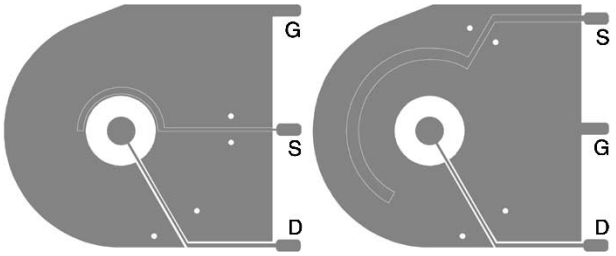

Fig. 15. Layout of two circular dielectric sensors with different depths of sensitivity determined by the position of the sensing electrode. Ignoring the effect of the narrow gap between the virtually grounded sensing electrode and the ground electrode, the electric field is identical for both sensors. The three electrodes are driven (D), sensing (S), and ground (G) [37], [105].

5) Nonorthogonal Layouts: Planar electrodes of any shape can generate fringing fields into the MUT. Different electrode shapes may be used to increase the capacitance, to concentrate the electric field at a specific location, to optimize specific spatial Fourier components of the electric potential in order to change the effective penetration depth, or to exploit symmetry of the MUT. A top view of cylindrical geometry dielectrometry sensors is shown in Fig. 15 [37], [105]. The inner circular drive electrode is driven at a known voltage and frequency while the outer region is grounded. The sensing electrode is formed as a 180° cutout from this ground plane, with as small a gap as practically possible, and is kept at virtual ground potential. The entire bottom of the sensor substrate is grounded. Such sensors have application where components have circular symmetry, such as holes and fasteners, and enables the design of families of circularly symmetric dielectrometers with the "model-based" methodology, replacing the Fourier series analysis with a Fourier–Bessel series [37], [105]. The circular geometry completely eliminates the y direction edge effect because the counterpart of y in cylindrical coordinates is the angle ϕ.

Other electrode shapes may require 3-D modeling. For example, planar coaxial and planar square spiral electrodes were modeled with 3-D finite-element software and compared to the interdigital layout of the same area [106]. The square spiral electrode layout had a slightly higher interelectrode capacitance due to a higher influence of end effects.

V. Modeling

The task of finding the complex impedance between interdigital electrodes is not a trivial one. Traditional analytical methods can provide closed-form solutions only for a limited number of classic electrode shapes, such as parallel-plate, cylindrical, and spherical electrodes [107].

Even a 2-D approximation of the interdigital structure results in the electric field distribution that is too complex to be described rigorously by simple algebraic expressions. The potential distribution along the sensor–material interface between the driven and sensing electrodes is not known in advance, and depends on the material properties and geometric parameters of the structure. The potential distribution must be calculated by satisfying charge conservation at the interfaces.

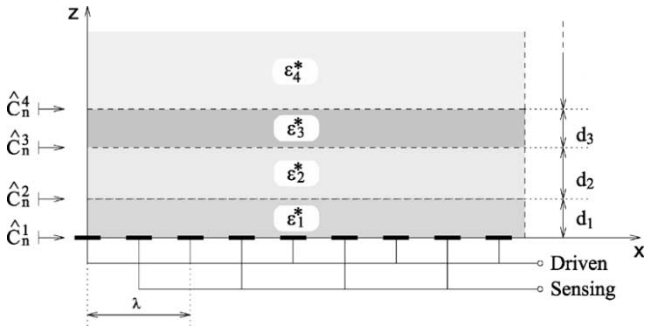

Fig. 16. Interdigitated electrode structure with a number of homogeneous layers above it [20].

A major portion of the earlier development efforts of frequency-wavelength dielectrometry was dedicated to solving the forward problem with a "continuum model." This model provides a mathematical description of the stratified media in terms of known values of the complex dielectric permittivity, defined in (4), for each layer.

A. Capacitance and Conductance

1) Continuum Model: From the electro-quasi-static field point of view, in a homogeneous medium, the electric scalar potential of the field excited by the driven electrodes is a solution to Laplace's equation. At any constant z position, the electric field distribution far away from the sensor edges of Fig. 4 is periodic in the x direction and assumed uniform in the y direction. In this case, the scalar potential of (2) can be written as an infinite series of sinusoidal Fourier modes from the fundamental spatial wavelength λ. This approach, called the continuum model, was developed in the 1980s and the 1990s [18], [20], [25], [26], [50]. The representation of electric potential with spatial Fourier modes falls between closed-form analytical solutions given by (2) and numerical techniques to solve the conservation of charge boundary condition between electrodes. It is less computationally expensive than traditional numerical approaches, but it does not offer analytical expressions suitable for extensive manipulation, for example, to calculate the analytical form of a Jacobian matrix associated with a given electrode geometry. Being limited to multiple-layer problems, the continuum model does not possess the generality of numerical techniques that allow computation of electric fields associated with arbitrary shapes. On the other hand, it is easier to incorporate a problem-specific individually written computer code implementation of a continuum model as a subroutine to a variety of inverse problem algorithms.

Fig. 16 shows the idealized view of the interdigital structure with a multilayered material above it. In order to validate a 2-D analysis, the electrodes are assumed to be infinitely long in the y direction and possess infinite periodicity in the x direction.

An additional idealized assumption in the original model was the negligible thickness of the sensor electrodes. This assumption introduces a nonnegligible error into parameter estimation algorithms. If desired, it can be removed by assuming an additional dielectric layer between the side walls of interdigital electrodes that have finite thickness [91]. Also,

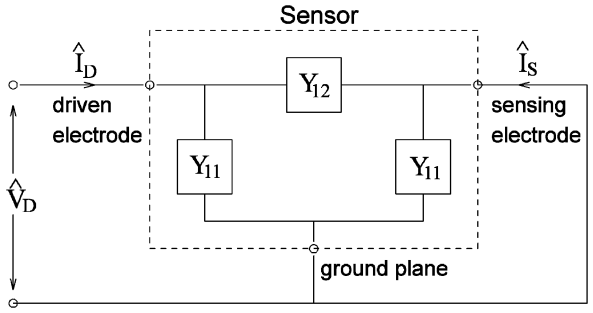

Fig. 17. Lumped circuit model for the interdigitated sensor structure within the dashed box and shown with grounded sensing electrode [50].

the surface layer analysis in the continuum model can be achieved by specifying a very thin layer with bulk properties that lead to equivalent total conduction. Since the model does not involve finite elements, the error due to small layer thickness is not significant.

For the simplicity of discussion, the following model also assumes that there is no surface conductivity at the interfaces between material layers. The reader is referred to [25] to learn how surface conductivity can be incorporated into the continuum model.

The continuum model was developed for steady-state ac excitation. Impulse or step responses are of great interest because they provide equivalent information to that received from the ac excitation frequency sweep while significantly reducing the required measurement time. The issues related to transformation between time and frequency domains are treated separately. In this discussion we use the following convention: All quantities are complex, since only a single time sinusoidal mode $e^{\mathrm{j}\omega\mathrm{t}}$ is assumed. The remaining complex amplitudes that are functions of space are denoted by a tilde ($\sim$). The complete time and space dependence of the corresponding physical quantity is obtained from

$$F(x,z,t) = \Re\left\{\widetilde{F}(x,z)e^{\mathrm{j}\omega\mathrm{t}}\right\} \tag{10}$$

where ω is the steady-state radian frequency. If a quantity's spatial x dependence is also sinusoidal, then it can be represented by a complex phasor denoted by a "hat" ($\widehat{\ }$)

$$\tilde{F}(x,z) = \widehat{F}(z)e^{-jkx} \tag{11}$$

$$F(x,z,t) = \Re\left\{\widehat{F}(z)e^{j(\omega t - kx)}\right\} \tag{12}$$

where k is the wavenumber, related to the wavelength λ as

$$k = \frac{2\pi}{\lambda}. \tag{13}$$

Many designs of interdigital sensors and associated electronic circuitry use the three-terminal symmetrical pi-equivalent circuit model shown in Fig. 17. Strictly speaking, every individual wavelength section of an interdigital sensor has four electrical terminals: driven electrode, sensing electrode, ground electrode, and guard electrode. By means of an operational amplifier follower circuit, the guard electrode is always held at the same potential as the sensing electrode, so that any current between them is effectively eliminated. As long as the amplifier can provide the necessary current magnitude, the admittance between the guard electrode and the other three electrodes has no influence on the measurement. We may, therefore, leave the guard electrode out of the circuit model. The goal is to be able to calculate the admittances between these three terminals from the parameters of the layer structure.

The circuit model of the structure is shown in Fig. 17. Ideally, the admittance Y_{11} of the driven electrode to ground is the same as the admittance of the sensing electrode to ground because the two electrodes should have an identical geometry. In reality, especially when the total number of fingers is small, these two admittances may be somewhat different because the number of fingers is not always exactly the same. However, admittances per unit length are indeed the same. The parameter Y_{12} represents the transadmittance between the driven and sensing electrodes. It has much stronger dependence on the MUT properties than the other two equivalent circuit elements. The sensing electrode admittance Y_{11} primarily depends on substrate properties with some fringing field dependence on the MUT. The admittance Y_{12} primarily depends on the MUT properties with some fringing field dependence on substrate properties. The drive electrode admittance Y_{11} is usually unimportant for determining the sensor voltage when the voltage on the drive electrode is imposed.

One can calculate the admittances by applying test voltages at the terminals and calculating the resulting terminal currents. Since the equivalent circuit is independent of electrical terminal constraints, the simplest form of test circuit is to ground the sensing electrode and apply a voltage $\tilde{V}_D$ to the driven electrode as shown in Fig. 17. Then the unknown admittances can be calculated in the following way:

$$Y_{12} = -\left.\frac{\widehat{I_S}}{\widehat{V_D}}\right|_{V_S=0} \tag{14}$$

$$Y_{11} = \left.\frac{\widehat{I_D} + \widehat{I_S}}{\widehat{V_D}}\right|_{V_S=0}. \tag{15}$$

In order to calculate $\hat{I}_D$, we need to know the normal component of the total (displacement plus conduction) current density $j\omega\varepsilon^*\widetilde{E}_z(x)$, which is integrated over the area of the driven electrode to give the total terminal current. It is, therefore, necessary to solve for the electric field distribution.

The entire interdigitated structure is periodic in the x direction with a fundamental wavelength λ. This means that for every quantity that depends on x, we may use Fourier series expansions to write

$$\widetilde{\Phi}(x,z) = \sum_{n=-\infty}^{\infty} \widehat{\Phi}_n(z)e^{-jk_n x} \tag{16}$$

$$\widetilde{E}_z(x,z) = \sum_{n=-\infty}^{\infty} \widehat{E}_{\mathrm{zn}}(z)e^{-jk_n x} \tag{17}$$

where n is the Fourier mode number and

$$k_n = \frac{2\pi n}{\lambda}. \tag{18}$$

It is convenient to define the *complex surface capacitance density* $\widehat{C}_n$, which relates $\varepsilon^*\widehat{E}_{\mathrm{zn}}$ at a planar surface $z =$

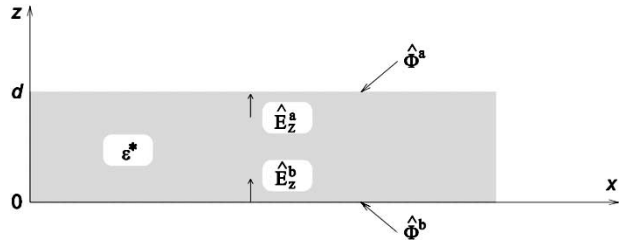

Fig. 18. A representative layer of homogeneous material [25], [50].

constant to the potential $\widehat{\Phi}_n$ at that surface for every Fourier mode n in the following way:

$$\widehat{C}_n = \frac{\varepsilon^* \widehat{E}_{\mathrm{zn}}}{\widehat{\Phi}_n}. \tag{19}$$

Since $\varepsilon^* \widehat{E}_{\mathrm{zn}}$ is continuous across interfaces without electrodes and $\widehat{\Phi}_n$ is continuous across interfaces, then $\widehat{C}_n$ is also continuous crossing from above to below an interface. Knowing $\widehat{C}_n$ at an electrode surface allows calculation of the terminal currents from the potential distribution at that surface

$$\begin{aligned}\hat{I}_t &= \sum_{n=-\infty}^{\infty} \oint_S j\omega\varepsilon^* \widehat{E}_{\mathrm{zn}} e^{-jk_n x} dxdy \\ &= \sum_{n=-\infty}^{\infty} \oint_S j\omega \widehat{C}_n \widehat{\Phi}_n e^{-jk_n x} dxdy \end{aligned} \tag{20}$$

where the integration is over an electrode surface. For the typical 50% metallization ratio, the integration in the x direction is over the quarter-wavelength width of the drive or sense electrode, and the integration in the y direction amounts to multiplication by the electrode length, since no quantity depends on the coordinate y. It is assumed here that each layer of material in Fig. 16 is homogeneous, so that within a layer, the complex permittivity $\varepsilon^* = \varepsilon - j\sigma/\omega$ is independent of the spatial coordinates. This means that Laplace's equation

$$\nabla^2 \Phi = 0 \tag{21}$$

is satisfied everywhere in space except at the interfaces between the layers due to discontinuity of ε^* and presence of a surface charge layer. At these interfaces, however, the boundary conditions require continuity of $\widehat{\Phi}$ (tangential component of $\overrightarrow{E}$ is continuous) and $\varepsilon^* \widehat{E}_{\mathrm{zn}}$ (normal component of conduction plus displacement current density is continuous). This means that at these interfaces, $\widehat{C}_n$ may be uniquely defined. Let $\widehat{C}_n^m$ be the complex surface capacitance density just above the $(m+1)$th interface (see Fig. 16), i.e., the surface at $z = \sum_{i=1}^{m-1} d_i$, with n referring to the Fourier mode. If we can express $\widehat{C}_n^m$ in terms of $\widehat{C}_n^{m+1}$, d_m, and ε_m^*, then we could apply this relationship recursively, beginning at the topmost layer N, to obtain $\widehat{C}_n^N$, then $\widehat{C}_n^{N-1}$, etc., and ultimately find $\widehat{C}_n^1$, the complex surface capacitance density at the electrode surface at $z = 0$.

Consider the slab of uniform material in Fig. 18. We would like to find $\widehat{C}_n^b = \varepsilon^* E_{\mathrm{zn}}^b / \Phi_n^b$ as a function of $\widehat{C}_n^a = \varepsilon^* E_{\mathrm{zn}}^a / \Phi_n^a$, ε^*, k_n, and d. Since (21) is satisfied, and since the potential is periodic in the x direction with a wave number of k_n, the z dependence of $\widehat{\Phi}_n$ must be exponential. We, therefore, choose the following form:

$$\widehat{\Phi}_n(z) = \widehat{A} \sinh k_n z + \widehat{B} \cosh k_n z. \tag{22}$$

We have the boundary conditions

$$\widehat{\Phi}_n(z=0) = \widehat{\Phi}_n^b \tag{23}$$

$$\widehat{\Phi}_n(z=d) = \widehat{\Phi}_n^a \tag{24}$$

which leads to the solution for $\widehat{\Phi}_n$

$$\widehat{\Phi}_n(z) = \frac{\widehat{\Phi}_n^a \sinh k_n z - \widehat{\Phi}_n^b \sinh k_n (z-d)}{\sinh k_n d}. \tag{25}$$

The z-directed electric field can be obtained from (25) by differentiation as follows:

$$\widehat{E}_{\mathrm{zn}} = \frac{-d\widehat{\Phi}_n}{dz} = k_n \left[\frac{-\widehat{\Phi}_n^a \cosh k_n z + \widehat{\Phi}_n^b \cosh k_n (z-d)}{\sinh k_n d} \right] \tag{26}$$

from which we obtain

$$\begin{aligned}\widehat{E}_{\mathrm{zn}}^a &= \widehat{E}_{\mathrm{zn}}(z=d) \\ &= -k_n \widehat{\Phi}_n^a \coth k_n d + k_n \widehat{\Phi}_n^b \frac{1}{\sinh k_n d} \end{aligned} \tag{27}$$

$$\begin{aligned}\widehat{E}_{\mathrm{zn}}^b &= \widehat{E}_{\mathrm{zn}}(z=0) \\ &= -k_n \widehat{\Phi}_n^a \frac{1}{\sinh k_n d} + k_n \widehat{\Phi}_n^b \coth k_n d \end{aligned} \tag{28}$$

$$\widehat{C}_n^a = \frac{\varepsilon^* \widehat{E}_{\mathrm{zn}}^a}{\widehat{\Phi}_n^a} = \varepsilon^* k_n \left(-\coth k_n d + \frac{\widehat{\Phi}_n^b}{\widehat{\Phi}_n^a \sinh} k_n d \right) \tag{29}$$

$$\widehat{C}_n^b = \frac{\varepsilon^* \widehat{E}_{\mathrm{zn}}^b}{\widehat{\Phi}_n^b} = \varepsilon^* k_n \left(-\frac{\widehat{\Phi}_n^b}{\widehat{\Phi}_n^a \sinh k_n d} + \coth k_n d \right). \tag{30}$$

From (29) we obtain

$$\frac{\widehat{\Phi}_n^b}{\widehat{\Phi}_n^a} = \left(\frac{\widehat{C}_n^a}{\varepsilon^* k_n} + \coth k_n d \right) \sinh k_n d \tag{31}$$

which we can then substitute into (30) to yield

$$\widehat{C}_n^b = \varepsilon^* k_n \left(\frac{\widehat{C}_n^a \cosh k_n d + \varepsilon^* k_n \sinh k_n d}{\widehat{C}_n^a \sinh k_n d + \varepsilon^* k_n \cosh k_n d} \right). \tag{32}$$

Let us test the validity of (32) in the limits $d = 0$ and $d = \infty$. For a layer of zero width, (32) reduces to $\widehat{C}_n^b = \widehat{C}_n^a$, as required. For $d \to \infty$ both the hyperbolic sine and cosine approach the exponential function, i.e.,

$$d \overset{\lim}{\to} \infty \left(\frac{\widehat{C}_n^a \cosh k_n d + \varepsilon^* k_n \sinh k_n d}{\widehat{C}_n^a \sinh k_n d + \varepsilon^* k_n \cosh k_n d} \right) = 1 \tag{33}$$

which reduces (32) to $\widehat{C}_n^b = \varepsilon^* k_n$. This is a useful result, as it directly applies to the semi-infinite topmost layer in Fig. 16. If its index number is N, then

$$\widehat{C}_n^N = \varepsilon_N^* k_n. \tag{34}$$

We now have the means of calculating $\widehat{C}_n^1$ from (32) and (34) by recursively descending down the layer structure. If on the bottom side of the electrode plane we had a similar set of

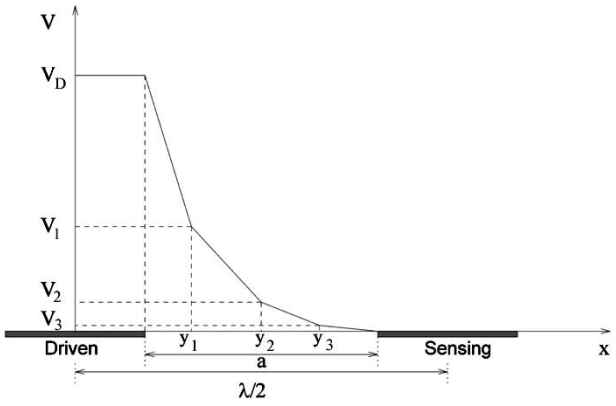

Fig. 19. Piecewise-smooth collocation-point approximation to the potential between the electrodes of an interdigitated structure. Three collocation points at y_1, y_2, and y_3 are shown [25].

layers, we would obtain a value for the surface capacitance density from that side also.

Instead of a structure of layers similar to the one in Fig. 16, the bottom side of the three-wavelength sensor has a single substrate layer of thickness h and permittivity ε_S which is typically purely real because the substrate's conductivity is negligible in typical substrate materials such as the polymers Kapton and Teflon. On the other side of the substrate, the metal backplane is deposited, which is typically grounded or guarded. We cannot use the equations developed so far to obtain the surface capacitance density due to the bottom side of the electrodes, because the potential of the back plane is forced to zero. We may, however, use (29) with $\widehat{\Phi}^b = 0$ to obtain

$$\widehat{C}_n^{-1} = \varepsilon_S k_n \coth k_n h \tag{35}$$

where the negative superscript indicates layers below the surface.

Since the surface capacitance density is known, it could be integrated over the areas of the driven and the sensing electrodes to obtain the currents $\hat{I}_D$ and $\hat{I}_S$ if the potential is known at the electrode plane. While the potential is indeed known along the electrodes, where it is constrained by them to be $\widehat{V}_D$ (driven electrode) or zero (grounded sensing electrode), in the space between the electrodes along the interface it is not known and must be determined by the conservation of charge boundary condition

$$\vec{n} \cdot \left[\vec{J}_1 - \vec{J}_2 + \varepsilon_1 \frac{\partial \vec{E}_1}{\partial t} - \varepsilon_2 \frac{\partial \vec{E}_2}{\partial t} \right] = 0. \tag{36}$$

The potential between the electrodes is approximated by a piecewise-linear function, which divides the space between drive and sense electrodes into $k_c + 1$ intervals, delimited by k_c *collocation points*, as shown in Fig. 19. In every interval the interfacial potential is assumed to vary linearly between the potentials at the two end points of the interval. The potential distribution is, thus, fully determined by the potential at the k_c collocation points. Now that we have a form for $\widetilde{\Phi}(y)$, we can use the Fourier integral to obtain an expression for $\widehat{\Phi}_n$, which is an algebraically linear function of the unknown potentials at the collocation points. In order to find these potentials $\widehat{\Phi}_j$, we need a set of k_c equations, which can be obtained by applying conservation of charge to k_c intervals centered at the collocation points. Reference [25] presents this process in detail, carrying out all integrations. References [37] and [91] provide additional details and improvements of this model. What is important to us is that this numerical process yields the potential distribution at the electrode surface and ultimately makes it possible to find Y_{11} and Y_{12}.

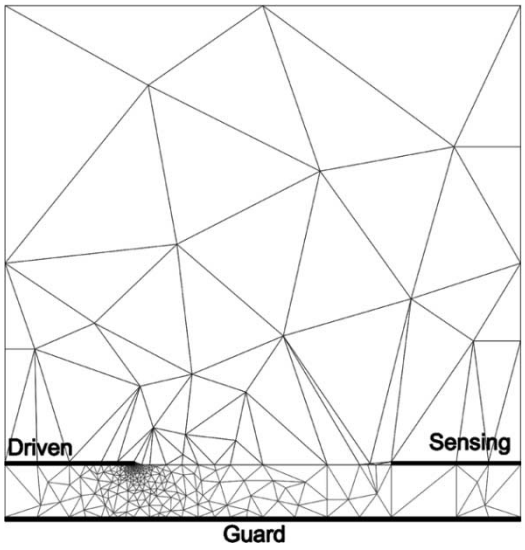

Fig. 20. An example of a triangular mesh used for computation of capacitance and conductance matrices associated with a half-wavelength section interdigital structure.

Finally, if the admittances in Fig. 17 are known and if the sensing electrode is loaded by an interface box of input admittance Y_L, the magnitude and phase of the voltage ratio are given by

$$\frac{\widehat{V}_S}{\widehat{V}_D} = \frac{Y_{12}}{Y_{12} + Y_{11} + Y_L}. \tag{37}$$

Sometimes, a metal plate is used to squeeze the materials under test against the surface of the interdigitated sensor. To account for its presence, the top layer can be modeled as a perfect conductor of infinite extent. If the conductor is present (e.g., to enhance shielding), the admittance values in Fig. 17 change, and this change must be included in the mathematical model (unless the top conducting plate is sufficiently far away from the sensor). The contribution of the higher order modes to the total capacitance value decays exponentially with the distance, but the contribution of the zero-order mode decays inversely to the distance to the top plate.

2) Finite-Element Calculations: The *Maxwell* finite-element method software package by Ansoft Corp. has been used extensively for calculation of capacitance and conductance matrices. Fig. 20 shows a typical half-wavelength cross section of an interdigital sensor with a triangular finite-element mesh superimposed with the electrode structure. The density of finite elements is higher in the higher electric field regions. Generally, a denser mesh results in a

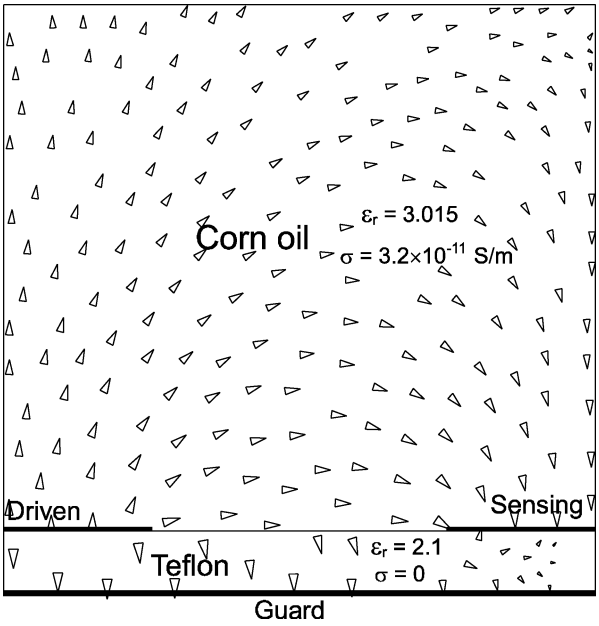

Fig. 21. Arrows indicate the direction and magnitude of the electric field at a low excitation frequency of 0.005 Hz in the half-wavelength section of the dielectrometry sensor. For the numerical case studies in this and the next five figures, the sensing electrode is grounded. The relative dielectric permittivity of the MUT (corn oil) has $\varepsilon_r = 3.015$ and conductivity $\sigma = 3.2 \cdot 10^{-11}$ S/m. Note that the direction of the conducting corn oil electric field arrow is essentially tangential above the oil–substrate interface.

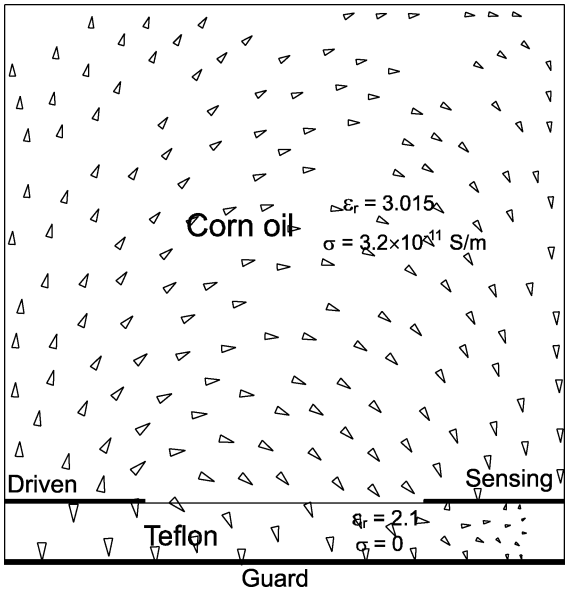

Fig. 22. Arrows indicate the direction and magnitude of the electric field at a high excitation frequency of 60 Hz. The relative dielectric permittivity of the MUT (corn oil) is $\varepsilon_r = 3.015$ and the conductivity is $\sigma = 3.2 \cdot 10^{-11}$ S/m. Note that the direction of the electric field arrows are obliquely incident to the oil–substrate interface.

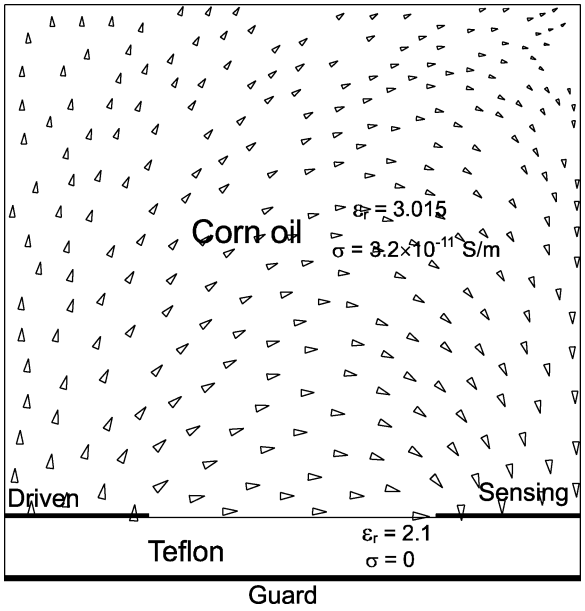

Fig. 23. Arrows indicate the direction and magnitude of conduction currents at an excitation frequency of 0.005 Hz. The relative dielectric permittivity of the MUT (corn oil) is $\varepsilon_r = 3.015$ and the conductivity is $\sigma = 3.2 \cdot 10^{-11}$ S/m.

more accurate solution; however, it is also more computationally expensive.

Figs. 21 –26 show the solution for electromagnetic quantities for two specific cases, at very low frequency and at high frequency, with respect to the ratio of conductivity and dielectric permittivity of the MUT. In all cases of this example, the driven electrode is held at 1-V peak sinusoidal excitation, and the sensing and guard electrodes are held at 0 V. This example is useful for developing intuition for correctness of computed field distributions and for visualization of physical processes in the bulk of material. The break frequency of $\omega_c \approx \sigma/\varepsilon \approx 5$ rad/s determines reasonable values for high $\omega \gg \omega_c$ and low $\omega \ll \omega_c$ frequency approximations.

By comparing Fig. 21 with Fig. 22, one can see that at a very low frequency in Fig. 21, the direction of electric field is essentially tangential to the substrate–corn oil interface above the interface and orthogonal to it below the interface. This happens because the low-frequency conduction currents, in this corn oil case, are much higher than the capacitive currents. In the high-frequency case of Fig. 22, the normal component of displacement field is continuous across the interface because both materials (corn oil and Teflon substrate) appear to be insulating. Thus, there is no surface charge at the interface in the high frequency limit. In both cases, the electric field intensity in the gap between the guard and sensing electrodes is very low because they are at the same potential. The scaling of the field line arrows with respect to field intensity is logarithmic; therefore, their size reduces approximately linearly, rather than exponentially, with the increase of the distance to the sensor electrodes in the upward direction. The field arrows are tangential to the left- and right-side boundaries due to the even periodicity of the electrode structure with respect to these boundaries.

Figs. 23 and 24 show the distribution of conduction currents for the same two cases. There are no conduction currents in the sensor substrate because it is assumed to be perfectly insulating. Similar observations can be made about the direction of the current density vector arrows as for the electric field arrows.

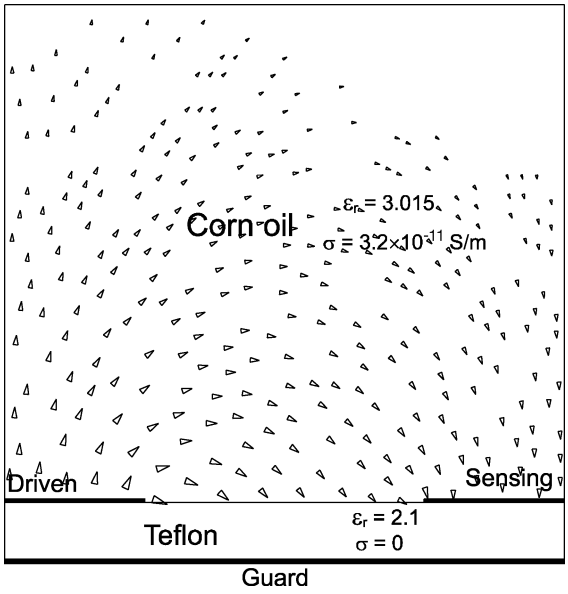

Fig. 24. Arrows indicate the direction and magnitude of conduction currents at an excitation frequency of 60 Hz. The relative dielectric permittivity of the MUT (corn oil) is $\varepsilon_r = 3.015$ and the conductivity is $\sigma = 3.2 \cdot 10^{-11}$ S/m.

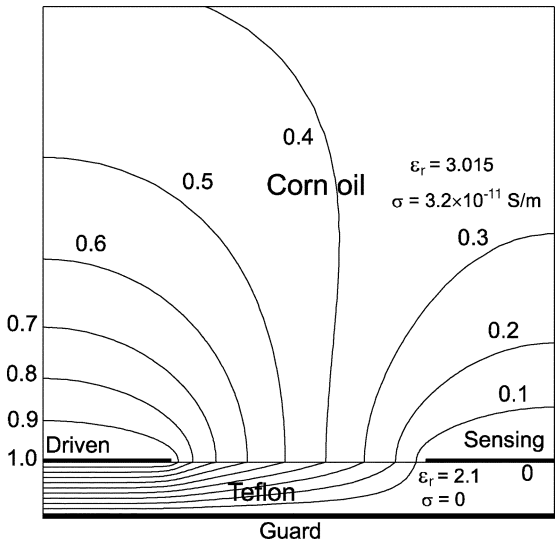

Fig. 25. Equipotential lines at an excitation frequency of 0.005 Hz. The relative dielectric permittivity of the MUT (corn oil) is $\varepsilon_r = 3.015$ and the conductivity is $\sigma = 3.2 \cdot 10^{-11}$ S/m.

Figs. 25 and 26 show the equipotential lines for the same two cases. Since the equipotential lines are perpendicular to the electric field lines, one can predict that they will come perpendicularly from above to the corn oil–Teflon interface at low frequency, at an angle to the same interface at high frequency, and perpendicular to the left and right region boundaries.

Finally, Fig. 27 shows the calculated distribution of the electric potential along the corn oil–Teflon interface. One can see that the slope of the potential is higher near the electrodes, which corresponds to higher intensity of the tangential electric field.

The distribution of electric potential above the interdigital electrodes can also be measured experimentally by using a needle probe. Naturally, the lateral and longitudinal electric field components can be computed from the potential distribution by partial differentiation. The highest spatial resolution of such measurements reported to date is in the submicrometer range [108].

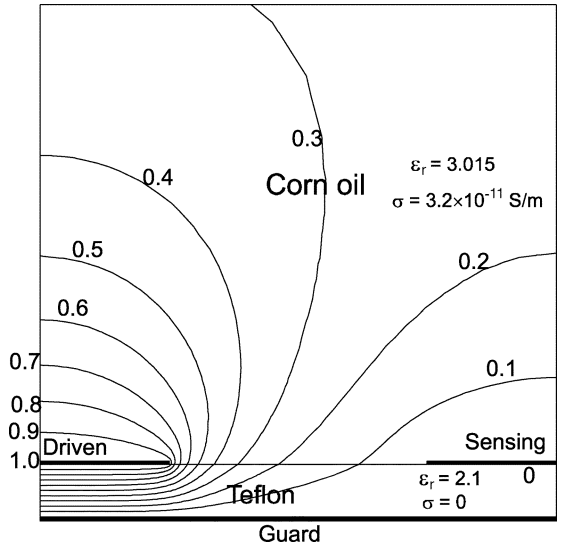

Fig. 26. Equipotential lines at an excitation frequency of 60 Hz for a corn oil dielectric.

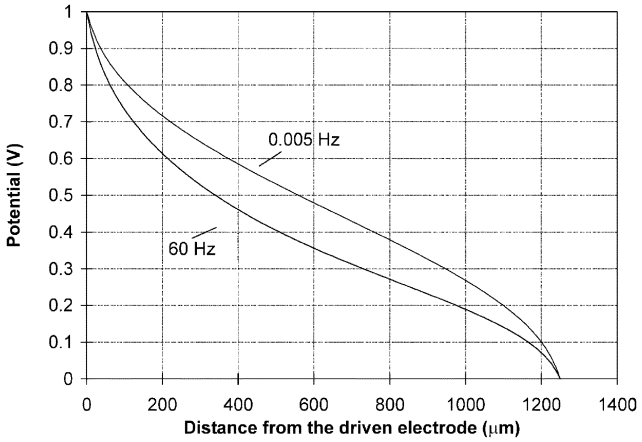

Fig. 27. Calculated distribution of the potential along the substrate–specimen interface between the driven and sensing electrodes for the cases shown in Figs. 21 –26.

3) Nondimensionalized Plot of Capacitances: Additional work was undertaken to produce a nondimensionalized plot of calculated capacitances between drive and sense and drive and backplane as a function of normalized substrate thickness d/λ and normalized dielectric constant $\varepsilon_m/\varepsilon_s$, where d is the substrate thickness, ε_m is the dielectric permittivity of the MUT of infinite thickness, and ε_s is the dielectric permittivity of the substrate. This required a *Maxwell* parametric sweep of two variables, one of which was spatial in varying the thickness of the substrate from 20 to 2000 μm. The total height of the simulated region was always maintained at 4000 μm. The other variable was the relative permittivity of the material, which was varied from 2 to 100, while the permittivity of the substrate was kept at ten to permit the ratio $\varepsilon_m/\varepsilon_s$ to have values above and below one. To save calculation time,

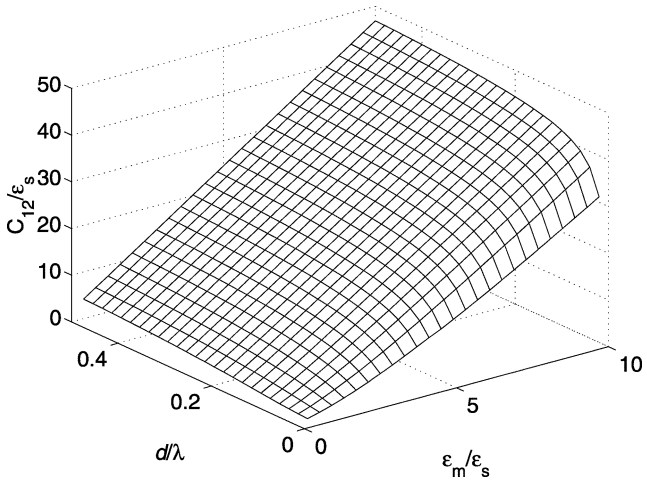

Fig. 28. C_{12}/ε_s versus normalized dielectric constant and normalized substrate thickness. This function can be used to predict the range of capacitance values in future sensor designs.

Table 5
Polynomial Coefficients a_{ij} for $x = d/\lambda$ (Substrate Thickness/Wavelength) and $y = \varepsilon_m/\varepsilon_s$ (Material Dielectric Constant/Substrate Dielectric Constant)

	x^3	x^2	x	1
y^3	3.8977676e-002	-8.5779518e-001	6.9341789e+000	4.3670077e+000
y^2	-7.6134189e-002	1.6695304e+000	-1.3413833e+001	-1.2547746e+001
y	4.6964771e-002	-1.0239383e+000	8.1446603e+000	1.3133535e+001
1	-9.2907431e-003	2.0048778e-001	2.8965208e+000	-1.5943268e+000

the permittivity sweep was done at each point in the distance sweep to prevent the calculation of a new mesh at every point. Once the data was simulated, it was processed within *Matlab* to produce 3-D mesh graphs shown in Fig. 28 as well as contour plots.

Table 5 lists the coefficients of the two-variable third-order polynomial fit of this data, according to

$$\frac{C_{12}}{\varepsilon_S} = \sum_{\substack{i=0,3\\ j=0,3}} x^i y^j \tag{38}$$

where $x = d/\lambda$ (substrate thickness/wavelength) and $y = \varepsilon_m/\varepsilon_s$ (material dielectric constant/substrate dielectric constant).

Of course, other numerical methods can be used for the calculation of capacitance and conductance matrices of interdigital sensors. Finite-difference simulation is treated in [109] and in [51]; a heat-conduction equivalence approach is used in [106]; another finite-element package, ANSYS, has been used in [110]; multiple-accelerated fast capacitance extraction is used in [111], and *RC* transmission line equivalency in [8].

4) Approximating Expressions: An approximate expression for the admittance of an interdigital structure (called lock and key device in the original source) was derived in the 1970s and later reported in [28]. The transadmittance Y between the drive and sense electrodes immersed in an infinitely thick layer of resin, as shown in Fig. 29, is

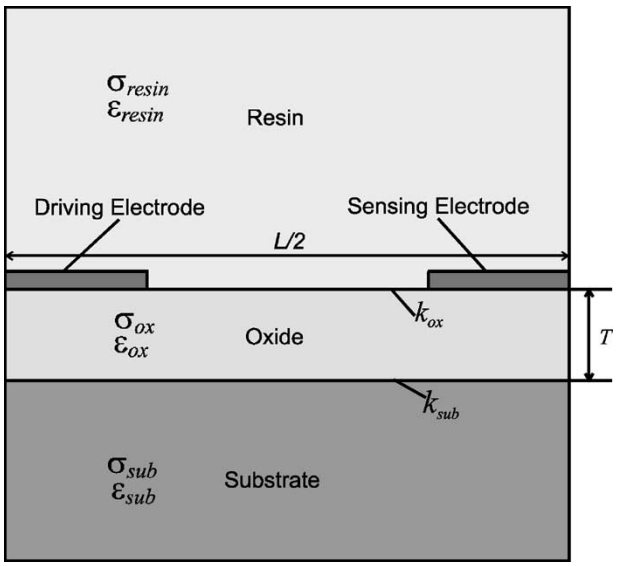

Fig. 29. Half-wavelength cross section of the interdigital electrode structure whose conductance and capacitance are approximated with (40) and (41).

$$Y = G + j\omega C \tag{39}$$

where

$$G = \frac{4\sqrt{2NW}}{\pi^2}\left[\sigma_{\text{resin}} + \sigma_{\text{sub}} + \frac{\pi T}{L}\sigma_{\text{ox}} + \frac{\pi}{L}(\kappa_{\text{ox}} + \kappa_{\text{sub}})\right] \tag{40}$$

$$C = \frac{4\sqrt{2NW}}{\pi^2}\left[\varepsilon_{\text{resin}} + \varepsilon_{\text{sub}} + \frac{\pi T}{L}\varepsilon_{\text{ox}}\right] \tag{41}$$

and N is a total number of gaps between individual fingers, W is the length of electrodes, L is the interelectrode separation, T is the oxide layer thickness, σ_{resin} is the conductivity of the resin, σ_{ox} is the conductivity of the oxide, σ_{sub} is the conductivity of the substrate, $\varepsilon_{\text{resin}}$ is the dielectric permittivity of the resin, ε_{ox} is the dielectric permittivity of the oxide, ε_{sub} is the dielectric permittivity of the substrate, k_{ox} is the surface conductivity at the oxide–resin interface, and k_{sub} is the surface conductivity at the substrate–oxide interface. This model is different from the sensor designs used in this paper, but is included here for future reference.

5) Conformal Mapping: Another potentially useful approach for the calculation of 2-D interdigital electrode capacitance stems from conformal mapping. Conformal mapping is one of the most frequently used approaches for calculation of the capacitance of interdigital structures, especially when the imaginary part of the complex dielectric permittivity of all materials is small enough to be neglected. Typical examples of such analysis are given in [95] and [112] for a case of interdigital electrodes of thickness h located on the boundary of two layers with relative permittivity $\varepsilon_{r1} = \varepsilon_1/\varepsilon_0$ and $\varepsilon_{r2} = \varepsilon_2/\varepsilon_0$ (no substrate). The layer of thickness h, with relative permittivity $\varepsilon_{r3} = \varepsilon_3/\varepsilon_0$, fills the gap due to the electrode thickness (see Fig. 30). Using a complete elliptic

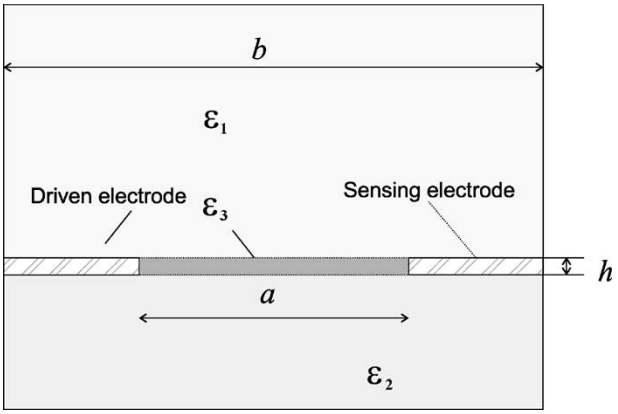

Fig. 30. Half-wavelength cross section of the interdigital electrode structure whose conductance and capacitance are approximated with (42) and (43).

integral of the first kind $K[x]$, the sum of the capacitances per unit length C_1 and C_2 due to relative dielectric permittivities ε_{r1} and ε_{r2} is found as

$$C_1 + C_2 = \varepsilon_0 \frac{\varepsilon_{r1} + \varepsilon_{r2}}{2} \frac{K\left[\sqrt{1 - \left(\frac{a}{b}\right)^2}\right]}{K\left[\frac{a}{b}\right]} \tag{42}$$

where a is the distance between inner edges and b is the distance between outer edges of electrodes in the half-wavelength representation of Fig. 30. The capacitance per unit length due to the volume of thickness h between the electrodes filled with relative dielectric permittivity ε_{r3} could be approximated as that of a parallel-plate capacitor

$$C_3 = \varepsilon_0 \varepsilon_{r3} \frac{h}{a}. \tag{43}$$

Then, the total capacitance between the driven and sensing electrodes is

$$C_{12} = C_1 + C_2 + C_3. \tag{44}$$

B. Force

The longitudinal electrostatic force (along the x axis, as shown in Fig. 31) in a comb drive is generated due to fringing fields at the ends of interdigital electrodes. This force is independent of the finger length and is proportional to electrode height. Ignoring fringing field effects, the capacitance of the interdigital finger with overlap length x is

$$C = \varepsilon_0 \frac{2nxb}{w} \tag{45}$$

where b is electrode height, w is the gap between electrodes, and n is the number of electrode fingers. Then the force developed by the finger interaction with application of voltage V is equal to [113]

$$F = \frac{1}{2} V^2 \frac{dC}{dx} = \frac{V^2 \varepsilon_0 bn}{w}. \tag{46}$$

This force becomes especially significant at micrometer and submicrometer scales.

While the longitudinal force is frequently employed in comb drives, sometimes other forces of Coulombic origin should be considered as well. The comb drives are often positioned above the substrate, which typically serves as a guard electrode. In the presence of nonsymmetry (guard plane at the bottom, but not at the top of the comb drive structure), the force orthogonal to the plane of electrodes (i.e., the force along the z axis) can reach a significant value. This levitation force (force along z axis) causes the electrodes to move with respect to each other. The force of levitation is also proportional to the square of the applied dc bias and the displacement between the electrode position and the stable equilibrium position [114]. In other words, the levitation force makes the electrode behave like an electrostatic spring. Normal displacements of over 2 μm for a comb bias of 30 V were observed [114]. To suppress this levitation, one can alternate the electrodes at every comb finger with a striped ground plane underneath the comb structure. The levitation effect can be further reduced by designing structures with vertically stiff suspensions. Controlled levitation can be realized by using soft suspensions and applying differential and common mode voltages with a specific ratio onto the two electrodes.

Mechanical engineering analysis of microscale interdigital structures typically uses classical approaches, developed for larger structures. An example of such a calculation is provided in [115]. The fundamental lateral resonance frequency f_r of the linear resonant plate, shown in Fig. 31, can be found using Raleigh's method

$$f_r = \frac{1}{2\pi} \left[\frac{k_{\text{sys}}}{(M_p + 0.3417M)}\right]^{\frac{1}{2}} \tag{47}$$

where M_p and M are the masses of the plate and of the supporting beams, respectively. For a linear resonant plate with the folded-beam structure as shown in Fig. 31, assuming the trusses joining the folded-beam segments are rigid, k_{sys} can be expressed as

$$k_{\text{sys}} = 24\frac{EI}{L^3} = 2Eh\left(\frac{W}{L}\right)^x 3 \tag{48}$$

where $I = (hW^3)/(12)$ is the moment of inertia of the beams, E is the Young's modulus, and h, W, L are the thickness, width, and length of each beam, respectively. In this case, the lateral resonance frequency can be found as [115]

$$f_r = \frac{1}{2\pi} \left[\frac{2Eh\left(\frac{W}{L}\right)^3}{(M_p + 0.3714M)}\right]^{\frac{1}{2}}. \tag{49}$$

The mechanical quality factor Q is estimated by assuming that Couette flow of air underneath the plate is the dominant dissipative process [115]

$$Q = \frac{d}{\mu A_p}(Mk_{\text{sys}})^{\frac{1}{2}} \tag{50}$$

where μ is the absolute viscosity of air $(1.8 \cdot 10^{-5}\ \text{Nsm}^{-2})$, A_p is the surface area of the plate, and d is the offset between the plate and the substrate. Quality factors for lateral motion are much higher than for motion normal to the substrate.

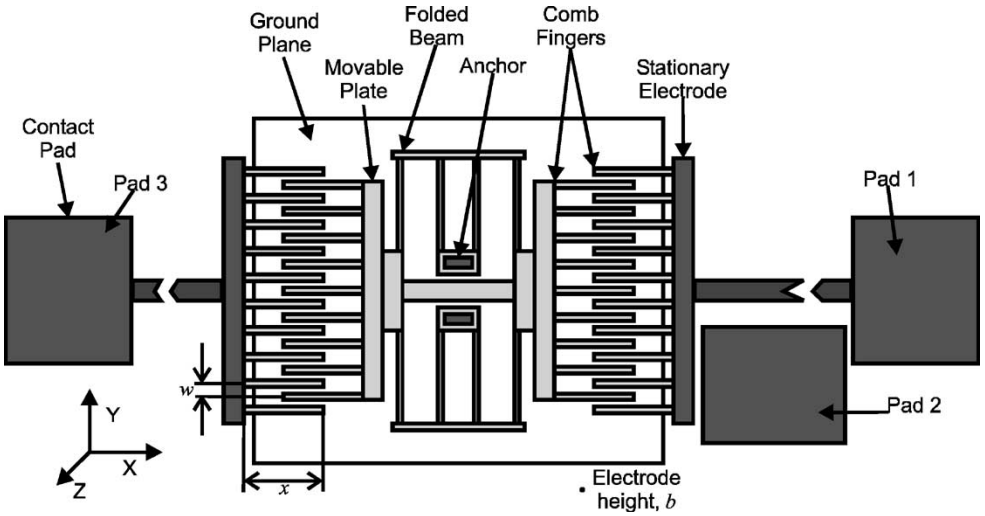

Fig. 31. Layout of a linear resonant plate [115].

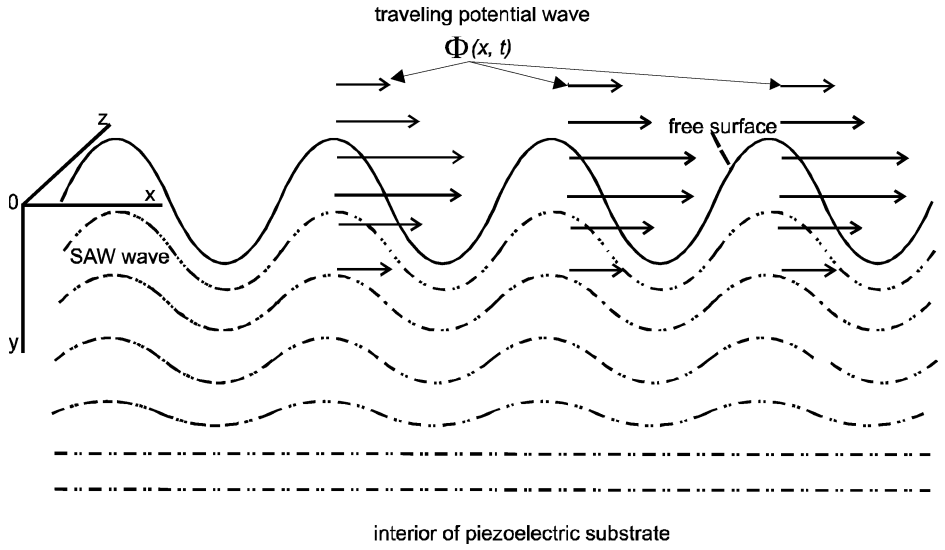

Fig. 32. Though the mechanism of the elastic wave propagation in a piezoelectric material is governed by equations of mechanical motion as well as Maxwell's electromagnetic equations, the mechanical solution dominates as the mechanical propagation occurs at a velocity that is on the order of 10^5 less than that of light. Even though the wave solution for the mechanical propagation of the surface wave is very complex, the electrical potential induced at the surface due to the mechanical propagation of the wave can be accurately modeled as a traveling wave of potential Φ [116].

C. Propagation of Acoustic Waves

The electrical potential Φ, which is induced by the surface wave at the surface of the piezoelectric substrate, can be modeled with a high degree of accuracy as a traveling wave of potential Φ (in volts)

$$\Phi = \Phi(x, y, t) \simeq \hat{\Phi} e^{j(\omega t - \beta x)} e^{-\beta |y|} \tag{51}$$

as sketched in Fig. 32 [116].

Here $\omega = 2\pi f$ is the angular frequency of the input signal in radians per second, β is the wave number in radians per meter, such that $\beta\lambda = 2\pi$ and $\lambda = v/f$ is the acoustic wavelength at SAW velocity v. The first term $e^{j(ax - \beta x)}$ shows the potential along the propagation direction on the surface. The second term $e^{-\beta |y|}$ is an approximate term that shows the decaying potential distributions along the y axis. Electric field E (volts per meter) is generated because of the variation of potential Φ on the surface. In the longitudinal direction, $E_x = -\partial\Phi/\partial x$ and the electric field in the vertical direction is given by $E_y = -\partial\Phi/\partial y$. Since many parameters contribute to frequency change of the SAW device, it is often difficult to determine the effect of a specific parameter on the change of frequency. The most common way to solve this problem is to utilize the reference element, which is equal to the original SAW sensor except for the layer of coated material that is highly sensitive to the parameter of interest. The diagram of such a device is shown in Fig. 33 [44]. The difference in frequency changes between these two elements reflects only the amount of change in the parameter of interest. The frequency change due to other influences is compensated through this reference element.

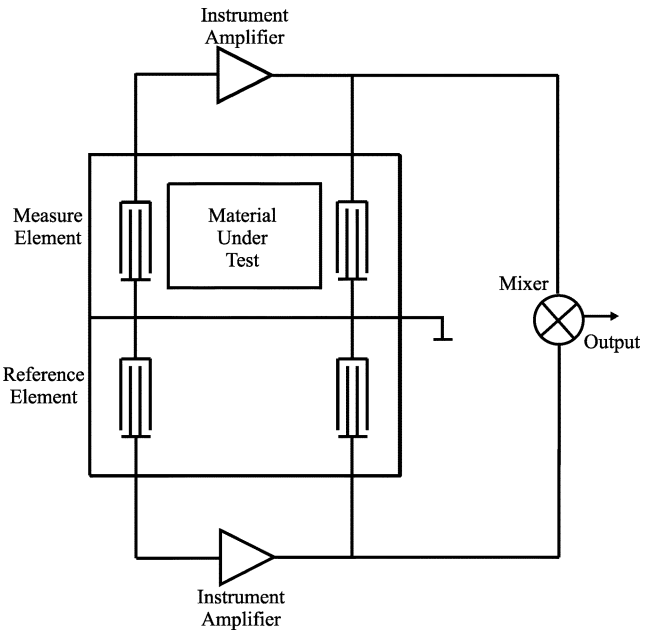

Fig. 33. SAW sensor using a reference element. The differential sensing scheme is implemented in hardware. External factors—for example, signal drift due to temperature—are canceled [44].

VI. Parameter Estimation Algorithms

Processing and interpretation of data from multiple sensor arrays is a research area that involves digital and analog signal processing, neural networks, wavelets, and statistical analysis. The full coverage of this topic is beyond the scope offered here; however, some general features related to most sensor array applications are described here.

A variety of interdigital sensors are used for a number of research and commercial applications to measure material properties [21], [117], control manufacturing processes [118], [119], monitor chemical and physical changes of fluid and solid dielectrics [79], [85], etc. In many cases, the interpretation of the sensor response depends on simple calibration procedures, yet in other cases, it requires sophisticated signal processing algorithms [120] and deep understanding of the physics and chemistry of the dynamic processes that are being monitored [121].

The task of interpreting sensor signals is fulfilled by parameter estimation algorithms, whose complexity, precision, accuracy, and reliability vary considerably depending on the experimental conditions and available computation time. The amount of information about material properties that can be extracted from dielectrometry measurements is limited by the number of independent equations and boundary conditions that can be solved using interdigital sensors and auxiliary instrumentation. The simplest experimental setup contains a single stationary interdigital sensor in contact with a studied material. In this case, one can only determine dielectric properties of permittivity and conductivity of a single homogeneous layer of known thickness; alternatively, one can determine the thickness of that layer if one of the dielectric properties is known in advance. In order to measure a larger number of unknown parameters, additional equations must be supplied to parameter estimation algorithms. These equations come from the auxiliary instrumentation, physical and numerical models of monitored processes (e.g., diffusion process), and, finally, from additional interdigital electrode pairs of different periodicities. Each independent sensor measures voltage gain magnitude and phase and, thus, can determine two unknown dielectric properties, permittivity, conductivity, or layer thickness.

To improve selectivity, reproducibility, and lifetime of interdigital sensors, two general approaches have been used to process the output signals of the chemical sensor array: 1) software with mathematical models and 2) conventional serial processing hardware.

Because of the nonlinear transfer characteristics of interdigital sensors, artificial neural networks (ANNs) are used for pattern recognition of multicomponent sensor systems [120]. It shows that the use of the reverse calibration technique supplies better results than the conventional method using an inverse model. On the other hand, a common disadvantage of ANNs is the immense amount of training data needed for the calibration. A new method, the dynamic test point distribution (DTPD), was invented to choose a higher density of test points in the region of interest and a modest density elsewhere [122]. This method achieves a significant reduction in the calibration time, together with a high accuracy in calculating the gas concentration. Mathematical models can also contribute to the improvement of signal processing. In an interdigital SO_2 sensor, the influence of humidity is eliminated by a mathematical model [123].

Compared with its software counterpart, serial processing hardware, although less easily modified, has the advantage of being faster and less expensive. A collective analog very large scale integration (VLSI) circuitry was designed and fabricated to process the outputs of an array of chemical sensors in a manner that allows robust chemical discrimination [124]. In testing, this circuitry chooses the winner (the maximum output) and the loser (the minimum output) in an array of tin oxide sensors. Then the locations of the winner and loser and their relationships with neighboring sensors have proven sufficient to discriminate among several types of alcohol and smoke.

VII. Applications

A. Humidity and Moisture Sensing

The idea of monitoring the surface conductance of thin dielectric films under changing environmental conditions was actively used in the development of several generations of capacitive humidity sensors [8]. The precision of measurement was limited by hysteresis of moisture adsorption. An accuracy of 7% of relative humidity in the range 17% to 65% relative humidity, and better accuracy at higher humidity values, was achieved. A shielding element is inserted between the fingers of a capacitance sensor in order to maximize the sensitivity due to the changes of dielectric properties in the sensitive layer deposited over the interdigital electrodes. The sensor was coated using chemical vapor deposition with a thin film of SiO_2. It is well known that the sheet resistance of silicon dioxide is a strong function

of ambient moisture. An interesting feature of measurements reported in [8] is so-called moisture hysteresis: the capacitance between the electrodes was dependent not only on the moisture level but also on the direction of moisture change. The capacitance at the same moisture level was lower when the moisture was increasing and higher when the moisture was decreasing. Most probably, the moisture dynamics in the bulk of the sensitive layer is responsible for this phenomenon. The equivalent circuit that was used to model changes in the sheet resistance of the sensitive layer was a classic distributed *RC* transmission line. Humidity-capacitance hysteresis has also been observed in another study [86], where a 1-μm-thick layer of crosslinked CAB polymer was used as a sensitive layer whose dielectric permittivity changes with relative humidity. An important application that developed from the original concept of the CFT [4] was a currently commercialized technique of microdielectrometry [11], [118].

An integrated design that combined the sensor, electrical buffer, oscillator, and decoder presented in [28] used different types of moisture-sensitive films, specifically, poly (p-aminophenylacetylene) (PAPA) and polyethylene oxide (PEO). Another moisture-sensitive material, aluminum oxide, being exploited as the sensitive layer exhibited a quicker response to the changes of the ambient relative humidity [125]. While this work demonstrated significant potential of the general approach, the reproducibility of measurements was quite low.

A typical frequency range for microdielectrometry measurements is from 1 Hz to 10 kHz. This range is appropriate for measuring sheet resistance in the range of 10^9 to $10^{16}\,\Omega/\text{square}$. The absorption of water on $MgCr_2O_4-TiO_2$ porous ceramic that results in rapid and reversible changes of electrical conductivity was investigated for high temperature applications (up to 550 °C) [126]. The electrical resistance of this multifunctional ceramic sensor decreases with an increase in relative humidity and increases with an increase in reducing gas content in the ambient atmosphere. A simultaneous and independent measurement of both ambient temperature and humidity is typically recommended.

Further advances in humidity measurement techniques involved the inclusion of moisture diffusion processes into the model of the Kapton sensor response [54]. The moisture diffusion coefficient was extracted from the dew point cycle measurements. The moisture diffusion coefficient in Kapton was evaluated to be on the order of $5.0\times10^{-9}\ \text{cm}^2/\text{s}$ at room temperature. A weak dependence of the diffusion coefficient on moisture concentration was observed as an asymmetry in the sorption and desorption kinetics. Design optimization of the moisture sensitive capacitance sensor is discussed in [127]. The advantages of linearity of sensor response had been investigated in [128].

An interesting analysis of moisture diffusion processes is described in [129], [130]. In this investigation, the moisture diffusion coefficients are measured in thin polymer films through monitoring changes in permittivity with microdielectric sensors. The dielectric properties are measured within the first 10 μm of the film thickness. The total film thickness is about 100 μm. By 1992, the frequency range of operation was extended over the range from 0.001 Hz to 100 kHz. The alternation of wet and dry environments allows measurement of diffusion coefficients for both absorption and desorption. Because of electrode polarization double-layer effects, the reported measurement was limited to the single frequency of 10 kHz. The dynamic analysis relies on the evidence available from the literature that the dielectric constant changes linearly with moisture content in polyimides [54] and epoxies [131]. A one-dimensional diffusion process is modeled with the traditional solution to Fick's law [132].

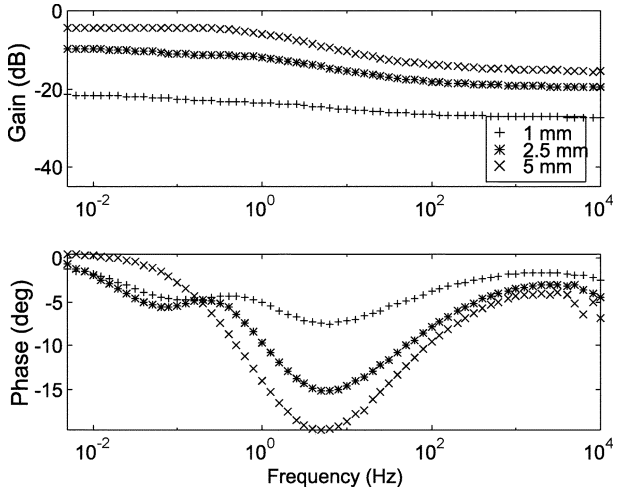

Fig. 34. Gain and phase for the three-wavelength paralyene-coated Kapton sensor of Fig. 11 with a thick layer (4 mm) of oil-free transformer pressboard in air pressed against the surface of the sensor. The load capacitances C_L were equal to 59.2, 23.3, and 23.3 pF for 1-, 2.5-, and 5-mm wavelengths, respectively.

An application of highly hydrophilic materials other than polyimide films opens doors for various biomedical applications. Usage of a water-swelling polymer as a sensitive layer over interdigitated electrodes that changes both conductivity and thickness with moisture absorption is discussed in [82]. The environmental stability and moisture effects related to various polyimide films, including Kapton, Upilex, and HQDEA/4-BDAF, are investigated in depth in [133]. Humidity detection in solar panel encapsulations with interdigital electrodes screen printed over glass and Tedlar films was accomplished by electrochemical impedance spectroscopy [93].

B. Electrical Insulation Properties Sensing

Results of experiments with oil-free transformer pressboard in air are shown in Figs. 34 –36. The shape of the phase curve in Fig. 34 differs from an ideal one-pole system primarily due to the dependence of the dielectric permittivity and conductivity of the pressboard on frequency. Estimation of the numerical values of the parasitic capacitance C_P due to finite electrode thickness and evaluation of its importance can be done based on the leftmost part of the gain curve in Fig. 34. Solution of the inverse problem and value of a complex dielectric permittivity for this material are shown in Figs. 35 and 36. For a homogeneous material, all three wavelengths should indicate approximately equal values of ε' and

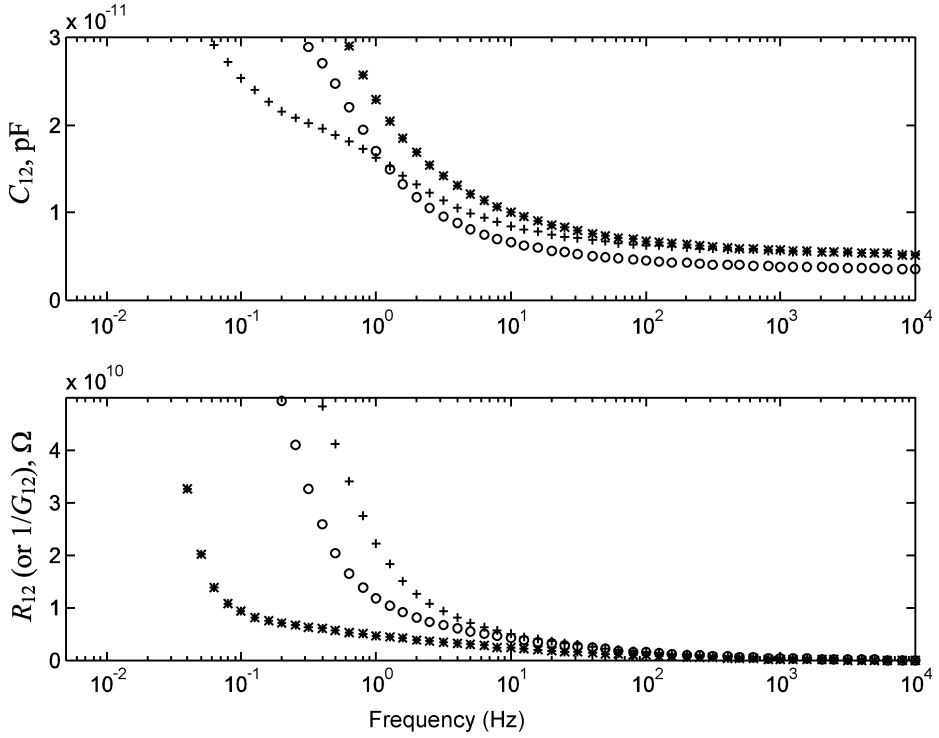

Fig. 35. Pressboard in air—solution of the inverse problem for a homogeneous material. $R_{12} = 1/G_{12}$ and C_{12} calculated values obtained from floating voltage gain/phase measurements of Fig. 34.

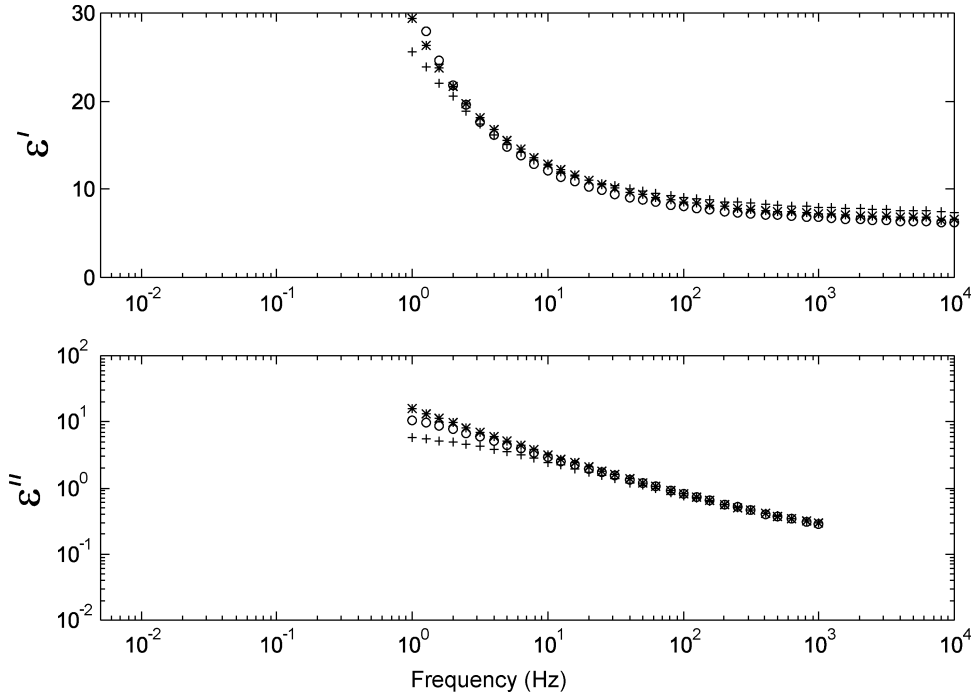

Fig. 36. Pressboard in air—the values of real part ε' and imaginary part ε'' of complex permittivity obtained using the data from Fig. 35. The electrode thickness has been taken into account by modeling it with finite-element software. The slope of $\log \varepsilon''$ versus $\log f$ is approximately -0.6, which indicates that pressboard is frequency dispersive.

ε''. The imaginary part of dielectric permittivity ε'' should have slope -1 as a function of frequency on a log–log plot for nondispersive material. Relative contribution of active and reactive parts of current flowing through the sample changes with frequency. It is easier to measure capacitance at high frequencies and conductance at low frequencies. Equivalently, it is easier to measure the real part of dielectric permittivity at high frequencies and the imaginary part at low frequency.

Calibration of complex geometry sensors can be executed by using simple parallel-plate or coaxial measurement cells where the relationship between the dielectric properties and terminal impedance is linear. The calibration of ε'' versus G_{12} has been done with a pressboard sample in a parallel-plate sensor. However, the results are not very reliable, partially due to low repeatability of the measurement. Only smooth, rigid, slightly compressible materials can be used for precise calibration for σ. In general, intimacy of contact, and, consequently, applied pressure, plays an important role and may potentially introduce very large errors in the parameter estimation process. In addition, surface contamination of the sensor itself may affect calibration, in which case it should be cleaned with solvents which easily evaporate with no residue.

C. Monitoring of Curing Processes

Dielectric properties change dramatically during the curing process of thermosetting resin matrix composite materials when the resin transforms from a monomeric liquid into a crosslinked insoluble solid material [106]. Advantages of using lower frequency excitation for dielectrometry measurements were explored in [134]. The core application of the microdielectrometer chip was to monitor the dielectric properties of thermosetting resin both during and after the curing process. The microdielectrometer chip uses the same principles as the more conventional parallel-plate measurement sensor. The advantages are smaller sensor size and on-chip amplification that eliminates the need for electrical shielding.

A parallel-plate capacitor is susceptible to expansion and contraction of the MUT [11]. The microdielectrometer chip is more reliable in this sense, as long as it stays in intimate contact with the MUT.

Using results of the 2-D numerical solution to Laplace's equation [109], one can calculate the sensor response in the entire range of possible values of the real and imaginary parts of complex dielectric permittivity. The sensor response is measured in terms of the gain and phase of the logarithm of the voltage ratio between the floating (sensing) and driving voltages.

The dielectric properties are found by plotting the gain/phase measurement point on the chart and interpolating using the nearest values of the real and imaginary parts of complex dielectric permittivity. Analysis of the experimental data has indicated an excellent fit with the Debye model for dipole orientation by using Cole–Cole plots with frequency as the plotting parameter [135]. An inherently low precision of measurement, the dielectric permittivity (ε') for high-loss materials and the dielectric loss factor (ε'') for low-loss materials are shown in terms of spacing between the lines of constant values.

A more advanced measurement approach involves simultaneous measurement of temperature as well as the complex dielectric permittivity [136]. On-chip amplifiers and off-chip electronic circuitry of the microdielectrometer sensor permit measurement of interelectrode capacitance down to 0.1 pF with acceptable accuracy. The authors point out that the separation of ε' and ε'' is always possible because the sensor dimensions are stable with respect to temperature and pressure variations. Interpretation of the dielectric analysis data is proposed based on the Debye model for dipole relaxation [137].

Another combination of sensing techniques, microdielectrometry and differential scanning calorimetry (DSC), has been used to study cure processes in epoxy resins [138]. In this study, the frequency sweep approach had been replaced by a so-called Fourier transform digital correlator, which allows interpretations of measurements in the frequency range from 0.005 Hz to 10 kHz. The domination of ionic conductivity in the early stage of the cure process had been observed (see also [139]). The ionic conduction can be correlated with viscosity during the early stages of resin cure. Later stages of cure can be analyzed using the loss factor as a sensitive measure of the crosslinking [140].

With the introduction of lower frequency measurements, the double-layer effects became particularly important. The role of the double layer in both parallel-plate measurements and microdielectrometry measurements was studied in [141]. Aluminum and gold electrodes in contact with commercial resins exhibited a drastic increase of apparent dielectric permittivity at low frequencies. A polarization model was developed to explain this phenomenon. An analytical treatment of the double-layer impedance based on the continuum-model simulations of [25] is presented in [77] and [142].

Mapping techniques are frequently used in microdielectrometry. An expression that relates viscosity and ionic conductivity has been proposed in [17]. Experiments demonstrated a high correlation between theory and measurements.

An industry-oriented overview of microdielectrometry given in [119] compares dielectrometry measurements with several other, more traditional, manufacturing process monitoring techniques, including DSC, rheological dynamic spectroscopy, and mechanical viscosity measurement. It also presents the critical point control (CPC) software designed for characterization of curing processes based on process phenomenology and correlation with other process monitoring techniques. Additional insights into correlation of data from various property estimation methodologies are presented in [98].

D. Chemical Sensing

Chemical sensors constitute a large portion of all interdigital sensors described in the literature. They are used in detection of various gases, chemicals, moisture, organic impurities, etc. A typical chemical interdigital sensor design is to deposit interdigital electrodes on an insulating substrate. The electrodes are coated with a thin layer of material that is sensitive to the concentration of chemicals present in the ambient atmosphere. The most common outputs of measurement are changes in resistance and capacitance between electrodes. The sensing mechanism is that when the sensor is exposed to ambient chemicals, the interaction of the chemicals with the sensitive material coating changes

the material's conductivity (σ), dielectric constant (ε), and/or the effective thickness (d) of the sensitive layer. The change in conductivity and effective thickness result in a resistance change, and the change of dielectric constant and effective thickness of the sensitive layer changes the capacitance. Interdigital chemical sensors are inexpensive to manufacture and can be integrated on a chip consisting of the sensor element and signal processing electronics.

1) Concentration of Gases and Vapors: A major application of interdigital sensors is to monitor the concentration of certain gases in ambient atmosphere. The adsorption of gases has to be reversible to reach a stable equilibrium with their concentration in the gas phase. The most important factor in gas monitoring is the sensing material. A wide variety of sensitive materials have been reported for chemical sensing. Two major classes of materials are inorganic semiconductor oxides and organic polymers that are conducting or insulating. Organic films have low melting points; therefore, they must be run at low temperatures, i.e., well below 100 °C for polymers. In contrast, semiconductor oxides are typically run at higher temperatures between 300 °C and 500 °C, depending on the target chemicals.

Detection of CO_2 has been given considerable attention due to recent concerns of CO_2 emissions as a global warming factor. A low-cost CO_2 sensor in thick-film technology has been developed using $BaTiO_3$ and various semiconducting oxides [76]. It is found that in this case the best composition of gas sensing material is $CuO\text{-}BaTiO_3 - La_2O_3 - CaCO_3$. Also the sensitivity increases with decreasing CO_2 concentration. A sodium carbonate-based CO_2 sensor has also been reported [143]. In this sensor, an encapsulated solid-state reference electrode is used to achieve a nearly drift-free response to CO_2 change (drift <0.5 mV/24 h).

Heteropolysiloxane exhibits a high sensitivity to SO_2 gas and so is used as the sensing material for SO_2 [45]. Co-condensation with the hydrophobic propyltrimethoxylane (PTMS) reduces response to humidity present in the air. This sensor was fabricated with gold thin-film technology on a silica glass substrate with nickel as an adhesive layer. A SAW transducer is included in the sensor system to reduce the overall cross sensitivity of the system to humidity.

Undoped, Pd-doped, and Pt-doped SnO_2-based thin-film chemical sensors have been used to determine quantitatively the concentration of NO_2, CO, CH_4, and H_2 [144]. The different contributions from contacts, surface, bulk, and grain boundaries to the sensor response were separated using different electrode configurations at different frequencies of electrical excitation.

Another example of an interdigital sensor used as a gas detector is the highly selective NO detection using Bi_2O_3-based materials. Doped and undoped Bi_2O_3 (a p-type semiconductor material) were used to detect NO. It has notable sensitivity and remarkable selectivity as compared to other components in exhaust gases, such as CO, CH_4, C_2H_6, C_3H_8, iso-C_4H_{10}, and H_2 [145]. Also the response time is very short, normally less than 2 to 3 min. The sensitivity for various test gases is monitored using simple two-terminal measurements.

Electrically conductive polymers poly(3-hexylthiophene) were investigated as ultrasensitive chemical sensors for hydrazine and monomethylhydrazine vapor [146]. It is demonstrated that concentrations in the 0.1–100 ppb range of these highly toxic species can be monitored with an accuracy of $\pm 20\%$. The sensor can be utilized for both dosimetric and real-time detection.

Cellulose derivatives such as ethylcellulose, cellulose–acetate, and cellulose–propionate were investigated to be used for detection of different organic compounds in the gas phase, e.g., ketones, alkanes, alcohols, aromatic, and chlorinated hydrocarbons [88]. A quartz microbalance (QMB) is coupled with an IDC to measure changes of masses (Δm) upon molecule/polymer interactions in this experiment. For different compounds, capacitance changes are mainly determined by the dipole moments of the analyte molecules.

The most commonly used sensor array is the planar structure, which consists of two planar lumped electrodes manufactured in conventional thin-film technology on an insulating substrate. The mechanism is based on the interaction between the surface of the layer and the gas molecules. Different electrode geometries and their relationship with sensor sensitivity are being investigated [95]. It is found that a very small electrode gap can achieve high sensitivity.

Three-dimensional interdigital structures are another very popular configuration. Gold electrodes with heights of 10 and 20 μm are produced through photolithography followed by an electroplating process [96]. This structure is used when the sensitive materials have to be applied by a spray or immersion process, which makes the coatings porous. The increased layer thickness results in bulk effects, which gives rise to a much higher sensitivity.

2) Measurement of Electrochemical Double Layer: A better understanding of boundary layer electrochemical processes can also be obtained from dielectrometry measurements. In ionic systems, oppositely charged ions effectively neutralize each other in the bulk, but at electrode boundaries, there is a preferential adsorption of one ion with the opposite polarity ion distributed over a thin boundary region. The degree of net charge and the depth to which charge penetrates into the liquid volume are related to the balance of ion diffusion and migration. In equilibrium, diffusion due to charge concentration gradients is balanced by the electric field of the separated charge forming a charge layer with thickness of order the Debye length, λ_D approximately equal to $\sqrt{\varepsilon D/\sigma}$ where D is the molecular diffusion coefficient. Such a charge layer acts like a large series capacitor which dominates the dielectric impedance at low frequencies. In room temperature transformer oil, D is approximately 2.5×10^{-11} m^2/s, $\varepsilon \approx 2.2\ \varepsilon_o$, and $\sigma \approx 10^{12}$ S/m, so that the Debye length is about 22 μm, resulting in a series capacitance per unit area of about 1 μF/m^2.

Transformer oil dielectric and electrical double-layer properties were determined by immersing an air-gap variable capacitor and measuring the impedance over a range of frequencies and temperatures. These impedances were then used to determine element values in an equivalent elec-

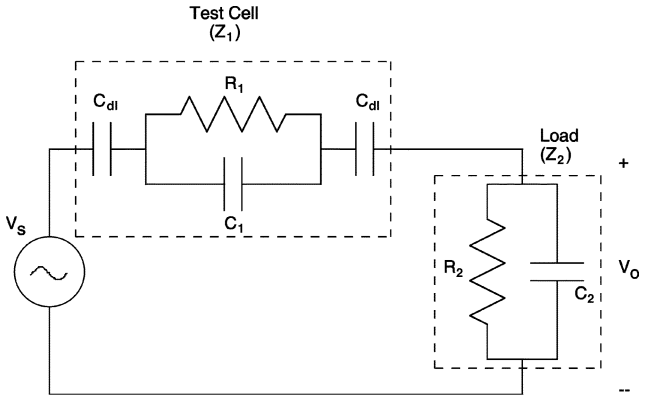

Fig. 37. An electrical circuit diagram for the liquid dielectric measurements. The electrode capacitances $C_{\rm dl}$ result from the space-charge polarization associated with the electrical double layer while the bulk properties of the liquid are given by R_1 and C_1.

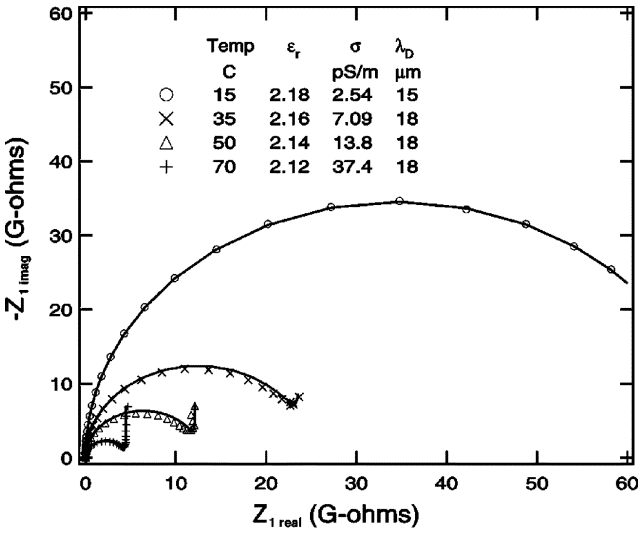

Fig. 38. Representative impedance measurements for Shell Diala A transformer oil at four temperatures. The lines give the calculated impedances for the listed estimated parameters [121].

trical circuit, where each element was a lumped parameter representation of the liquid dielectric properties.

The test cell impedance was determined by connecting the cell to the circuit shown in Fig. 37 and measuring the voltage gain across the circuit (v_o/v_s) as a function of frequency. The voltage source generated a sinusoidal signal having a peak amplitude of 1 V at a frequency that could be varied from 5 mHz to 10 kHz. The gain and the phase measurements were performed by a data acquisition unit designed to perform gain-phase measurements with interdigitated dielectric sensors [121].

The test cell impedance can be related to the measurements of the gain and the phase. With the circuit in sinusoidal steady state and the known load Z_2 composed of a resistor R_2 in parallel with a capacitor C_2, the real and imaginary parts of impedance Z_1 can be determined as

$$Z_{1r} = \frac{R_2\left[\left(\frac{1}{|G|}\cos\phi - 1\right) - \frac{\omega R_2 C_2}{|G|}\sin\phi\right]}{1+(\omega R_2 C_2)^2} \quad (52)$$

$$Z_{1i} = \frac{-R_2\left[\frac{1}{|G|}\sin\phi + \omega R_2 C_2\left(\frac{1}{|G|}\cos\phi - 1\right)\right]}{1+(\omega R_2 C_2)^2} \quad (53)$$

with ω the angular frequency, $|G|$ the magnitude and ϕ the phase of the complex voltage gain defined in (8), Z_{1r} the real part of the impedance, and Z_{1i} the imaginary part of the impedance. For these measurements the transition frequency $1/R_2C_2$ was chosen to be below the frequency range of the measurements by making the load the operational amplifier input impedance ($R_2 = 1000\ G\Omega$) and a capacitor ($\mathrm{C}_2 = 750$ pF).

A lumped element model for the impedance is then used to determine the bulk conductivity and permittivity of the liquid. While the simplest model for the dielectric is a resistor R_1 in parallel with a capacitor C_1, this model is inadequate for describing the data. If the unknown impedance were formed by a resistor in parallel with a capacitor, a plot of the imaginary part of the impedance against the real part of the impedance would be a semicircle. While this applies at the lower temperatures, the semicircular shape is lost at the higher temperatures, as illustrated by the Cole–Cole plots in Fig. 38. This is consistent with capacitive elements at the electrodes and motivates the form of the test cell impedance illustrated in Fig. 37. The electrode capacitances $C_{\rm dl}$ result from the space-charge polarization associated with the electrical double layer while the bulk properties of the liquid are given by R_1 and C_1. The lumped elements are related to the liquid dielectric properties by

$$C_1 = \frac{\varepsilon A}{d-2\lambda_D} \qquad R_1 = \frac{d-2\lambda_D}{\sigma A} \qquad C_{\rm dl} = \frac{\varepsilon A}{\lambda_D} \quad (54)$$

with A the area, d the electrode spacing, σ the liquid conductivity, ε the liquid permittivity and with λ_D the characteristic Debye length over which the space-charge is distributed. The geometric factor A/d is determined by measuring the capacitance of the structure in air $\mathrm{C_{air}}$.

In this model three material properties are unknown: the permittivity, the conductivity, and the Debye length. Estimating these properties requires a minimum of two impedance measurements. With the permittivity of the fluid obtained from a high-frequency measurement, a low-frequency measurement (such as 10 mHz, where the double-layer effects are apparent) can be used with (54) and the model test cell impedance to give

$$\sigma = \frac{\varepsilon_o}{C_{\rm air} Z_{1r}}(1+\omega\varepsilon_r C_{\rm air} Z_{1i}) \quad (55)$$

$$\frac{\lambda_D}{d} = -\frac{\omega\varepsilon_r C_{\rm air}}{2}\left(Z_{1\rm i} + \frac{\omega\varepsilon_r C_{\rm air} Z_{1r}^2}{1+\omega\varepsilon_r C_{\rm air} Z_{1i}}\right). \quad (56)$$

This approach was used to estimate the material properties and generate the Cole–Cole plot given in Fig. 38. This relatively simple approach fits the data well.

Representative results are listed in Table 6 of two other tests. The variation in the oil permittivity with temperature provides an indication for the accuracy of the measurements; since the relative permittivity $\varepsilon_r = \varepsilon/\varepsilon_0$ should be essentially constant at 2.2, the slight error is attributed to a small unmodeled parasitic capacitance.

Table 6 also includes the estimated Debye lengths and the associated values for the molecular diffusivity D, calculated from $\lambda_D = \sqrt{\varepsilon D/\sigma}$. These measurements show that the

Table 6
Representative Estimated Properties for the Oil Sample Used in Experiments Described in Figs. 37 and 38

Temp °C	ε_r 10 kHZ	σ (pS/m) 0.01 Hz	λ_D μm	D 10^{-11} m^2/s
15	2.18	2.54	15	3.0
35	2.16	7.09	18	12
50	2.14	13.8	18	24
70	2.12	37.4	18	65

Debye length varies from about 8 to 20 μm for typical transformer oil samples over the temperature range of 15 °C to 70 °C.

E. Biosensing

Biosensors are self-contained, portable electronic devices which utilize biological events at the molecular level to detect and quantify chemical and biological substances [80]. With recent advances in biotechnology, it is natural to expect an increasing number of applications of interdigital dielectrometry sensors for monitoring of physiological processes.

The lipid bilayer constitutes the basic structure of all biological membranes. Developed methods of formation of stable bilayer lipid membranes on top of the interdigital arrays make these membrane layers attractive candidates for biomolecular electronic devices and biosensor applications [90]. The interdigital arrays (made of Pt) serve as bilayer support.

Differential interdigital sensor design (when the active sensor signal is subtracted from the reference sensor design) results in particular high sensitivity. An acetylcholine receptor-based biosensor was reported to detect nanogram quantities of cholinergic ligands per milliliter [80]. The response of the sensor is measured through the percentage change in impedance between the control and reference chip. The possible mechanism is that the binding of a ligand to the immobilized receptor on the acetylcholine receptor biochip results in a conformational change, which changes the overall electrical properties of the biochip.

A simple miniature conductance biosensor is also built with interdigital electrodes [147]. It monitors the change in concentration of charged reaction products generated by the enzyme-catalyzed reactions by responding to changes in the electrode double-layer capacitance. Moreover, three sets of electrodes with different sensitive layers were used to determine concentration of three distinct reaction products. Fast response time of the device was achieved through careful choice of suitable enzyme immobilization regimes. It allows the construction of a flow cell with the incorporation of a urease-modified device to continuously measure urea in flowing systems.

An interdigital sensor array that uses conductivity, piezoelectricity, and voltage/current electrochemical sensing principles was reported in [90]. In addition to these principles, thin-film sensitive coatings of ZnO_x and lipid bilayers were used.

F. Transducer Applications

1) Capacitive Transducers: MEMS have recently gained considerable interest due to numerous potential benefits in sensing, mechanical, biomedical, automotive, military, and aerospace applications. Typical micromachined motors and actuators today occupy area less than 1 mm^2 and weigh a few milligrams. Conceptual overviews of MEMS technology are given in [100], [148]–[152]. The interdigital comb drive is one of the most common MEMS devices, mainly used in linear microactuators to produce linear movement of machine parts using fringing electric fields at the tips of the comb fingers.

In brief, the theory of operating the lateral resonant structure can be described as follows [153]. An ac drive voltage is applied between one of the side pads and the central structure. Because of the electrostatic attraction between interdigitated comb fingers, at the correct ac frequency, the central structure will be driven into a mechanical resonance at a frequency determined by the elastic modulus of the material, as well as by the geometry of the structure. In a typical layout of a linear comb drive of a lateral resonator, the IDCs perform a dual function: supplying force for linear movement of the load and sensing the current position of the load with respect to stationary parts.

Several properties of interdigital electrodes make them attractive for use as microelectromechanical resonators. The interelectrode capacitance changes linearly with displacement. Thus, electrostatic comb drives have linear electromechanical transfer functions for large displacement. Consequently, the electrostatic drive force is independent of the vibration amplitude, which can be significantly higher than those observed in the structures which move normal to the surface of the substrate [114]. Also, the gap between comb fingers is found to be the most important design parameter for both the quality factor and the drive efficiency for operation at atmospheric pressure [154]. The presence of a ground plane underneath the interdigital electrodes causes an asymmetry in the electric field distribution, which eventually leads to levitation induced by an electrostatic attraction force [114], [155]. The ground plane is necessary to shield the interdigital electrodes from external electric fields [156]. Interdigitated fingers and the mechanical structure are etched in a single low-pressure chemical vapor deposition (LPCVD) polysilicon film, which has been deposited on a patterned sacrificial oxide layer. A significant advantage of this technology is that all the critical structures are defined with one mask, eliminating errors due to mask-to-mask misalignment [115].

The major advantage of using electrostatic forces as opposed to magnetic forces is that a very high energy density can be achieved when the distance between the adjacent electrodes becomes small [157]. A further advantage of small electrode gaps is that the electrical breakdown strength increases as gap size decreases as given by the Paschen curve. Electrostatic excitation combined with capacitive detection is an attractive approach for resonant micromechanical transducers because of the simplicity

and compatibility with micromachining technology [115]. Interdigitated resonators also have less air damping on the structure, leading to higher quality factors. Linearity of the electrostatic-comb drive and flexibility in the design of the suspension for the resonator are also advantages of this technology [154].

Interdigital electrostatic combs can be built for linear electrostatic motors. The potential applications of them include friction test structures [158], microgrippers [159], force-balanced accelerometers [160], and positioning of components with submicrometer precision [161].

Accurate prediction of thin-film materials response has always been a challenging problem because a bulk testing method, such as a uniaxial tension test, is very difficult to apply directly to thin films. New methodologies for uniaxial tensile and cantilever bending testing of both micrometer and submicrometer scale freestanding specimens use interdigital MEMS actuators [162]. A lateral comb drive actuator with 3150 combs was designed to generate a total force of 382 μN at 40 V. Experimental results highlight the potential of interdigital actuators as a new tool for materials research. In another application, amplitude and phase response with respect to frequency are measured by an amplitude modulation technique and are used with the corresponding mechanical model to estimate various electromechanical properties [163].

An accelerometer with a sensitivity of 95 mV/g and a bandwidth of dc $\sim$ 1 kHz has been built [164]. When acceleration is applied in the lateral direction, the change in capacitance of the interdigital electrodes results from the overlap of area variation between the two capacitors and is measured using a charge amplifier. A mechanical holding system for a silicon wafer has been constructed using an electrostatic chuck, which consists of interdigitated electrodes and a dielectric thin film [165]. It has an advantage that the electrical connection to the wafer is not needed.

2) SAW Devices: SAW-based devices have the following advantages.

1) SAW devices can be designed to provide complicated signal processing functions with a fairly simple structure (a single piezoelectric substrate with normally two IDTs).
2) A broad range of response functions can be obtained through variation of electrode patterns.
3) Outstanding reproducibility and accuracy.
4) Most SAW devices are manufactured using single-stage lithography, which is ideal for mass production of low-cost devices.

SAW devices have extremely versatile and stable characteristics. They are developed for delay lines, bandpass filters, matched filters, resonators, and oscillators. All these modules are widely used in computer, automotive, telecommunication, industrial, military, space, and consumer applications. A large number of applications have been explored with SAW devices and similar interdigital sensors, including sensing and control of drag and skin friction in aerospace and underwater structures [100], aircraft flex beam deflection and acceleration, ice formation monitoring on aircraft wings [46], noise suppression in buildings [152], and early warning from collapsing bridges [100], [152].

The delay line is a very common application of SAW technology. It can store 2 to 3 μs of signals in 1 cm of length [43]. The operating frequencies for simple two-port delay lines range from 10 MHz to 2.5 GHz, corresponding to a state-of-the-art interdigital finger linewidth below 0.5 μm. Typical time delays are from 0.3 to over 100 μs, bandwidths from 1 to over 500 MHz, and losses from 10 to 35 dB. Extra IDTs can be added to the substrate along the propagation path. In this way multiple-port or tapped delay lines are developed. Delay lines can be packaged for surface protection and hermiticity in semiconductor packages, or integrated into hybrid circuitry.

Transducers with interdigital electrodes can also be used for bandpass filtering [166]. When apodization is applied to the transducer with constant electrode pitch, the bandpass filtering can be realized through controlling the frequency response. It can be designed simply by Fourier transformation of the required frequency response, using the resulting time-domain function to determine the electrode voltage weightings. This approach shows the enormous degree of flexibility available of this technique, because any kind of frequency response can be synthesized with this principle. SAW filters are used for TV, audio, and video consumer products. The military uses them for communication and for signal intelligence with frequency synthesis and frequency sorting. In 1998, about 350 million SAW filters were produced for consumer and telecommunication products [167].

Another major area of SAW applications is matched filtering. To extract useful information from a SAW device, it is essential to maximize the signal-to-noise ratio. The maximum signal-to-noise ratio is obtained when the receiver has a filter characteristic with the impulse response being the time inverse of the received signal. This type of a filter is called a matched filter. Matched filtering can be easily implemented by manipulating the interdigital electrode configurations on the substrate. In radar systems matched filters offer increasing range for a given resolution, without increasing peak transmitter power. In communication systems, this technique results in multipath resolution, improved immunity to interference, and capability of multiple addresses [168].

A typical SAW resonator is composed of two gratings and two IDTs between them. The gratings form a resonant cavity, and the two IDTs are used for input and output. There are two types of resonators: homogeneous and composite resonators. For the homogeneous resonator, the entire substrate is affected by environment changes. It is often used for temperature and stress measurement. Composite resonators normally include additional materials, usually a thin sensitive coating to perform a variety of tasks, such as measurement of mass density, film thickness, molecular weight of polymers, and viscosity of liquids [44]. The major advantage of SAW resonators is that they can operate at the fundamental frequencies 10 to 100 times higher than those of bulk acoustic wave resonators. SAW resonators are also used as frequency and time controlling parts in fiber optic data links, computers,

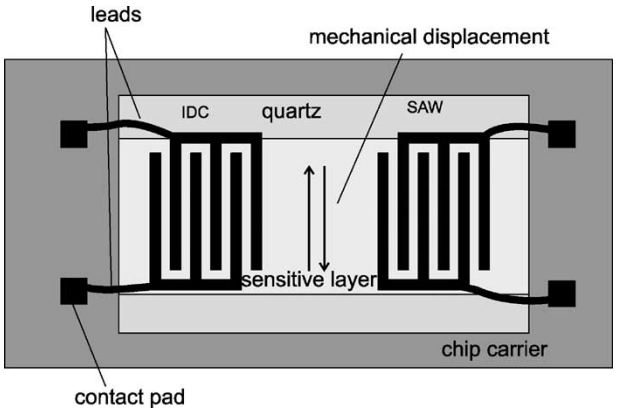

Fig. 39. A combined sensor that comprises a SAW transducer and an IDC on a single chip. (Adapted from [45].)

keyless entry systems, tags, and telecommunication applications. Recently they have been used for low-loss (<3 dB) high-frequency filters, by cascading resonators in ladder and lattice configurations.

G. Combination of SAW Devices and IDCs

Interdigital dielectrometry sensors and SAW devices have essentially identical electrode topology, but they use different mechanisms to measure changes in the material. Each technology has inherent advantages and drawbacks. In several studies SAW transducers demonstrated higher sensitivity to the changes in the mass absorption properties, compared to the changes in the dielectric permittivity of the sensitive layer [45].

The natural step in sensor development is to combine positive aspects of each sensing technology in a single design. In this case, SAW transducers and interdigital dielectrometry sensors demonstrated a different relative sensitivity to SO_2 and to H_2O. One such design combining both devices, shown in Fig. 39, used SO_2-sensitive material (heteropolysilaxane, NND/PTMS) to reduce the overall cross sensitivity of the sensor to humidity interference [45]. The combination of these two different types of transducers increases the performance of the sensor system.

H. Nondestructive Testing

NDT has received much attention in recent years due to the ever-increasing need for real-time quality monitoring. Acoustic sensing has been widely used for NDT [169]–[174]. NDT sensors can be broadly classified into two types: the conventional external scanning sensors, and the newer embedded sensors.

The conventional external sensors use a probe that is scanned over the whole area to be tested. In such a setup, bulk longitudinal waves or shear waves are generally used to detect subsurface faults. The acoustic waves are transmitted through the MUT and their propagation speeds are estimated [175]. The variation in the speeds of propagation is then mapped onto structural integrity [176] or material homogeneity [177]. This method requires a very good coupling between the probe and the surface of the MUT. The most reliable coupling is achieved by immersing the test material in a water bath and conducting the test on the immersed material [178]. This approach, however, cannot be used to test large test objects such as aircraft wings. An alternative coupling approach is to apply a liquid gel locally over the area to be tested. Acoustic reflectance characteristics have also been used to detect structural anomaly [179]. As can be seen, these methods are extremely time consuming and, hence, expensive when large areas are to be covered. Reference [180] discusses many important applications of NDT using SAW.

Embedded sensors are usually used to monitor large surfaces. The longitudinal and shear waves used in the conventional scanners propagate only in the region immediately around the transmitting transducer. This is not suitable for implementing embedded sensors, as it would require a large number of transducers to cover the entire surface, as the surface covered by each transducer is very small. Lamb waves are the special case of Raleigh waves when the thickness of the substrate is so small that it is comparable with the wavelength of the signal. Lamb waves are better suited for such applications, as they can propagate over long distances [181]. However, at any given frequency, there are at least two modes of propagation for Lamb waves that are dispersive. This tends to make the received signals complex and more difficult to interpret. Single-mode generation of Lamb waves can be achieved by controlling the frequency and the wavenumber bandwidths of the excitation source [182], [183]. The frequency bandwidth can be controlled by using the windowed tone burst excitation signals [182]. The transducer geometry and the angle between the transducer and the surface controls the wavenumber bandwidth [182]. By carefully controlling both these parameters, *in situ* monitoring of large structures using embedded sensors can be realized.

VIII. Future Trends

Sensor arrays. Small modifications of a basic design permit a variety of sensing principles to be combined within a single array. Functionalization of sensing surfaces with multiple compounds in a single-array chip is becoming increasingly widespread with all sensing principles, including electric, acoustic, and optical. Different thin films, layers of antibodies, or membrane structures can be built to have orthogonal response to a broad array of chemical and biological substances. With continuing miniaturization of electronics as well as sampling systems, the integration of all individual sensors in a single chip or a single sampling system is becoming easier. Information from different types of sensors integrated into a single monitoring system can be used to monitor, control, and predict performance of various systems.

An example of such a multisensor single chip technology is multicomponent gas chemical analysis [184]. A sensor array device (SAD) that includes six polymer-coated interdigital sensors on a silicone nitride membrane combined with

built-in thin-film thermometer/heaters has been manufactured to measure concentration of toluene, n-propanol, and n-octane [184]. An array of six interdigital sensors lying upon a micromachined 0.5-μm-thick silicon nitride membrane for detecting organic solvents was described in [79].

Array sensors. Interdigital and other fringing field electrode structures are a likely element in designing flexible array sensors, sometimes referred to as smart skin or sensitive skin. This concept has been pursued in a variety of applications, including robotics, biomedical devices, and wearable sensing [185], [186]. The idea is to build a flexible filmlike device with a comprehensive coverage of the surface by several types of sensors, similar in functionality to human skin. The numerous challenges on the path toward this goal include data processing for the huge number of sensor pixels; avoiding excessive wear and tear; implementation of useful sensing mechanisms on flexible substrates; and providing interconnections to all elements.

Complexity of electrode structures. Modifications to a classic interdigital sensor array structure are increasingly used to improve the sensor performance. Such modifications may include new apodization patterns for acoustic wave devices, combination of meandering and interdigital electrodes in a single structure, and dynamically changing geometry or field bias, especially in MEMS. For example, a second interdigital electrode was added above the sensing layer of an interdigital sensor to apply an electric field, which influences the charge carrier concentration and the surface potential at the grain boundaries [187]. Using this configuration, an enhancement in sensor selectivity can be expected. Somewhat analogous to customizing electric field patterns to the MUT is the approach of customizing wave propagation characteristics in acoustic sensors [188]. One may expect a transition from analog circuits to a mixed-signal circuits, where such customization would be achieved with digital circuitry. This approach is already taking place in acoustic RF identification (RFID) tag technology, for example.

Nondestructive testing. Although the applications of SAW devices in NDT have been under intensive development for a long time, many measurement-type modifications remain an open territory for future studies. Further deployment of array sensors and sensor networks is expected for measurement of multilayer properties (e.g., in composite materials [189]) and monitoring of distributed infrastructure [188]. Transition to autonomously operating power-harvesting nondestructive sensors is expected in such fields as avionics, power generation, and naval technology.

Sensor fusion. Monitoring of temperature of the MUT provides crucial information for a correct interpretation of the dielectrometry sensor response. For that reason, a temperature-sensitive resistor is often placed on the same chip with the dielectrometry interdigital sensor [51], [126].

Combination of interdigital sensors with auxiliary instrumentation provides numerous advantages. For example, wireless communication with an IDT can be implemented by connecting the transducer with a small microwave antenna [190], [191]. This duo is particularly advantageous when the sensor is placed on the moving part (such as an aircraft rotor), and wired communication with the rest of hardware is technically cumbersome.

Further miniaturization. Interdigital structures will be as useful in the nanotechnology research, as they were useful in the MEMS domain in the past decade. The optical gratings will be built to perform additional sensing functions, especially with fringing electric fields. In addition, dielectrophoretic forces generated on the nano scale are so significant that they are becoming a major instrument for manipulation of nanoparticles. Of course, not all dielectrophoretic devices use interdigital or fringing electric field structures. Other arrangements are also pursued to achieve the goal of precise nanoscale matter manipulation.

Parameter estimation. Soft-field tomography algorithms are mostly used with circular and spherical geometry and, thus, fall beyond the scope of this paper. However, the subject of this paper, interdigital structures, is an important special case for imaging algorithms. With the continuing increase of signal processing capabilities, the inverse problem theorists will soon have a test bed for particularly computationally intensive methods. At the same time, real-time parameter estimation in fairly simple geometries will lead to increased acceptance of fringing field devices for process control.

Wireless communication. Another important feature of process control applications is ease of access and installation. In this regard, wireless communication chips in megahertz and more recently, gigahertz domains will be used in conjunction with lightweight embeddable sensors. The other two important paradigms stemming from the wireless sensor applications are on-chip power harvesting and wireless sensor networks. Of course, they are a universal drive for all types of sensors, not only the ones discussed in this paper.

IX. Conclusion

Interdigital electrodes are key elements of capacitive sensors, dielectrometry imagers, bulk and SAW devices, tomographic profiles, and various MEMS. Applications of sensors and transducers that use interdigital electrodes include NDT, moisture imaging, chemical sensing, biosensing, microscale force and motion, and process control. Noninvasive measurements with gas, liquid, solid, and mixed systems are possible on distance scales from nanometers to meters and frequency of excitation from microhertz to gigahertz. Main advantages of interdigital electrode structure include one-side access to the MUT, convenience of application of sensitive coatings, a possibility of spectroscopy measurements through variation of frequency of electrical excitation, and material imaging capability through the variation of penetration depth.

This paper presented an overview of underlying principles, applications of interdigital sensors and transducers, modeling techniques, and limitations of existing sensor designs. Extensive references are provided to overview manuscripts in each application field. Examples of representative interdigital electrode applications are given for each class of sensors.

ACKNOWLEDGMENT

The authors would like to thank the researchers referenced throughout the paper, many of whom had fruitful discussions and collaboration with the authors. The authors would also like to thank Ansoft Corporation for their donation of software.

REFERENCES

[1] N. Tesla, "Electric condenser," U.S. Patent 464 667, 1891.

[2] E. H. Love, "Some electrostatic distributions in two dimensions," in *Proc. London Mathematical Soc.*, vol. 22, Apr. 1923, pp. 339–369.

[3] S. D. Senturia and C. M. Sechen, "The use of the charge-flow transistor to distinguish surface and bulk components of thin-film sheet resistance," *IEEE Trans. Electron Devices*, vol. ED-24, no. 9, p. 1207, Sept. 1977.

[4] S. D. Senturia, C. M. Sechen, and J. A. Wishneusky, "The charge-flow transistor: a new MOS device," *Appl. Phys. Lett.*, vol. 30, no. 2, pp. 106–108, Jan. 1977.

[5] S. D. Senturia, J. Rubinstein, S. J. Azoury, and D. Adler, "Determination of the field effect in low-conductivity materials with the charge-flow transistor," *J. Appl. Phys.*, vol. 52, no. 5, pp. 3663–3670, May 1981.

[6] W. S. Mortley, "Pulse compression by dispersive gratings on crystal quartz," *Marconi Rev.*, no. 59, pp. 273–290, 1965.

[7] I. G. Matis, "On multiparameter control of dielectric properties of laminate polymer materials," *Latvijas PSR Zinatnu Akademijas Vestis Fizikas un Tehnisko*, no. 6, pp. 60–67, 1966.

[8] R. S. Jachowicz and S. D. Senturia, "A thin-film capacitance humidity sensor," *Sens. Actuators*, vol. 2, no. 2, pp. 171–186, Dec. 1981.

[9] M. C. Zaretsky and J. R. Melcher, "Complex permittivity measurements of thin films using microdielectrometry," in *Proc. Conf. Electrical Insulation and Dielectric Phenomena*, 1986, pp. 462–471.

[10] N. J. Goldfine, A. P. Washabaugh, J. V. Dearlove, and P. A. von Guggenberg, "Imposed omega-k magnetometer and dielectrometer applications," in *Review of Progress in Quantitative Nondestructive Evaluation*. New York: Plenum, 1993, vol. 12, pp. 1115–1122.

[11] N. F. Sheppard, D. R. Day, H. L. Lee, and S. D. Senturia, "Microdielectrometry," *Sens. Actuators*, vol. 2, no. 3, pp. 263–274, July 1982.

[12] P. M. David, "History of SAW devices," in *Proc. 1998 IEEE Int. Frequency Control Symp.*, pp. 439–460.

[13] R. M. White and F. M. Voltmer, "Direct piezoelectric coupling to surface elastic waves," *Appl. Phys. Lett.*, vol. 7, pp. 314–316, 1965.

[14] I. N. Court, "Microwave acoustic devices for pulse compression filters," *IEEE Trans. Microwave Theory Tech.*, no. MTT-17, pp. 968–986, Nov. 1969.

[15] R. M. White, "Surface elastic waves," *Proc. IEEE*, vol. 58, pp. 1238–1276, Aug. 1970.

[16] ——, "Acoustic sensors for physical, chemical and biochemical applications," in *Proc. IEEE Int. Frequency Control Symp.*, 1998, pp. 587–594.

[17] J. O. Simpson and S. A. Bidstrup, "Modeling conductivity and viscosity changes during epoxy cure using TEA DMA and DSC," in *Proc. Amer. Chemical Soc. Division of Polymeric Materials: Science and Engineering Fall Meeting*, vol. 69, 1993, pp. 451–452.

[18] M. C. Zaretsky, P. Li, and J. R. Melcher, "Estimation of thickness, complex bulk permittivity and surface conductivity using interdigital dielectrometry," *IEEE Trans. Elect. Insulation*, vol. 24, pp. 1159–1166, Dec. 1989.

[19] M. C. Zaretsky, J. R. Melcher, and C. M. Cooke, "Moisture sensing in transformer oil using thin-film microdielectrometry," *IEEE Trans. Elect. Insulation*, vol. 24, no. 6, pp. 1167–1176, Dec. 1989.

[20] Y. K. Sheiretov and M. Zahn, "Dielectrometry measurements of moisture dynamics in oil-impregnated pressboard," *IEEE Trans. Dielect. Elect. Insulation*, vol. 2, pp. 329–351, June 1995.

[21] P. A. von Guggenberg and M. C. Zaretsky, "Estimation of one-dimensional complex-permittivity profiles: a feasibility study," *J. Electrostat.*, vol. 34, no. 2–3, pp. 263–277, Mar. 1995.

[22] P. Li, "Low frequency, millimeter wavelength, interdigital dielectrometry of insulating media in a transformer environment," M.S. thesis, Dept. Elect. Eng. Comput. Sci., Massachusetts Inst. Technol., Cambridge, 1987.

[23] A. V. Mamishev, B. C. Lesieutre, and M. Zahn, "Optimization of multi-wavelength interdigital dielectrometry instrumentation and algorithms," *IEEE Trans. Dielect. Elect. Insulation*, pp. 408–420, June 1998.

[24] J. Melcher, Y. Daben, and G. Arlt, "Dielectric effects of moisture in polyimide," *IEEE Trans. Elect. Insulation*, vol. 24, pp. 31–38, Feb. 1989.

[25] M. C. Zaretsky, "Parameter estimation using microdielectrometry with application to transformer monitoring," Ph.D. dissertation, Dept. Elect. Eng. Comput. Sci., Massachusetts Inst. Technol., Cambridge, 1987.

[26] M. C. Zaretsky, L. Mouayad, and J. R. Melcher, "Continuum properties from interdigital electrode dielectrometry," *IEEE Trans. Elect. Insulation*, vol. 23, pp. 897–917, Dec. 1988.

[27] A. V. Mamishev, B. A. Berdnikov, J. P. Rivenc, B. C. Lesieutre, and M. Zahn, "Surface contact effects in interdigital dielectrometry," in *Proc. 10th Int. Symp. High Voltage Engineering*, vol. 6, 1997, pp. 357–360.

[28] S. D. Senturia, N. F. Sheppard, S. Y. Poh, and H. R. Appelman, "The feasibility of electrical monitoring of resin cure with the charge-flow transistor," *Polym. Eng. Sci.*, vol. 21, no. 2, pp. 113–118, Feb. 1981.

[29] J. R. Melcher, "Electrohydrodynamic surface waves," in *Waves on Fluid Interfaces*. New York: Academic, 1983, pp. 167–200.

[30] S. M. Gasworth, J. R. Melcher, and M. Zahn, "Induction sensing of electrokinetic streaming current," in *IEEE Conf. Rec. Interfacial Phenomena in Practical Insulating Systems*, 1983, pp. 78–86.

[31] J. R. Melcher, "Charge relaxation on a moving liquid interface," *Phys. Fluids*, vol. 10, pp. 325–331, 1967.

[32] J. C. Zuercher and J. R. Melcher, "Double-layer transduction at a mercury-electrolyte interface with imposed temporal and spatial periodicity," *J. Electrostat.*, vol. 5, pp. 21–31, Oct. 1978.

[33] N. Goldfine, Y. Sheiretov, A. Washabaugh, V. Zilberstein, S. Kenny, and P. Crowther, "Materials characterization and flaw detection for metallic coating repairs," *Insight*, vol. 42, no. 12, pp. 809–814, Dec. 2000.

[34] N. Goldfine, M. E. Van Steenberg, and A. Washabaugh, "Inductive and capacitive sensor arrays for *in situ* composition sensors," in *Proc. IEEE Aerospace Conf.*, vol. 1, 2001, pp. 299–309.

[35] N. Goldfine, M. Zahn, A. V. Mamishev, D. Schlicker, and A. P. Washabaugh, "Methods for processing, optimization, calibration, and display of measured dielectrometry signals using property estimation grids," U.S. Patent 6 380 747, Dec. 2002.

[36] N. Goldfine, V. Zilberstein, J. S. Cargill, D. Schlicker, I. Shay, A. Washabaugh, V. Tsukernik, D. Grundy, and M. Windoloski, "Meandering winding magnetometer array eddy current sensors for detection of cracks in regions with fretting damage," *Mater. Eval.*, vol. 60, no. 7, pp. 870–877, July 2002.

[37] Y. Sheiretov, "Deep penetration magnetoquasistatic sensors," Ph.D. dissertation, Dept. Elect. Eng. Comput. Sci., Massachusetts Inst. Technol., Cambridge, 2001.

[38] S. Datta, *Surface Acoustic Wave Devices*. Englewood Cliffs, NJ: Prentice-Hall, 1986.

[39] B. A. Auld, *Acoustic Fields and Waves in Solids*. New York: Wiley, 1973.

[40] H. Matthews, *Surface Wave Filters*. New York: Wiley, 1977.

[41] A. A. Oliner, *Acoustic Surface Waves*. Berlin, Germany: Springer-Verlag, 1978.

[42] V. M. Ristic, *Principles of Acoustic Devices*. New York: Wiley, 1983.

[43] F. S. Hickernell, "Surface acoustic wave devices: a rewarding past, a significant present, and a promising future," in *Proc. 12th Int. Conf. Microwaves and Radar*, vol. 4, 1998, pp. 159–168.

[44] E. Benes, M. Gr, W. Burger, and M. Schmid, "Sensors based on piezoelectric resonators," *Sens. Actuators A, Phys.*, vol. 48, pp. 1–21, 1995.

[45] A. Leidl, R. Hartinger, M. Roth, and E. Endres, "A new SO_2 sensor system with SAW and IDC elements," *Sens. Actuators B, Chem.*, vol. B34, no. 2, pp. 339–342, Sept. 1996.

[46] V. K. Varadan, V. V. Varadan, and X. Q. Bao, "IDT SAW and MEMS sensors for measuring deflection, acceleration, and ice detection of aircraft," in *Proc. Smart Electronics and MEMS Conf.*, 1996, pp. 209–219.

[47] A. V. Mamishev, Y. Du, B. C. Lesieutre, and M. Zahn, "Development and applications of multi-wavelength interdigital dielectrometry sensors and parameter estimation algorithms," in *Proc. Joint Symp. Electrostatics*, 1998, pp. 169–181.

[48] P. A. von Guggenberg and J. R. Melcher, "An immersible relative saturation moisture sensor with application to transformer oil," in *Proc. 3rd Int. Conf. Properties and Applications of Dielectric Materials*, vol. 2, 1991, pp. 1258–1261.
[49] ——, "A three-wavelength flexible sensor for monitoring the moisture content of transformer pressboard," in *Proc. 3rd Int. Conf. Properties and Applications of Dielectric Materials*, vol. 2, 1991, pp. 1262–1265.
[50] P. A. von Guggenberg, "Application of interdigital dielectrometry to moisture and double layer measurements in transformer insulation," Ph.D. dissertation, Dept. Elect. Eng. Comput. Sci., Massachusetts Inst. Technol., Cambridge, 1993.
[51] J. M. Fouke, A. D. Wolin, K. G. Sanders, M. R. Neuman, and E. R. McFadden Jr, "Sensor for measuring surface fluid conductivity *in vivo*," *IEEE Trans. Biomed. Eng.*, vol. 35, pp. 877–881, Oct. 1988.
[52] L. Savio, "Managing overloads: The utility challenge," in *Proc. EPRI Workshop: Transformer Overload and Bubble Evolution*, 1987.
[53] "Kapton polyimide film: Summary of properties," Polymer Prod. Dept., Indus. Films Div., Du Pont Co., Wilmington, DE, 1998.
[54] D. D. Denton, D. R. Day, D. F. Priore, S. D. Senturia, E. S. Anolick, and D. Scheider, "Moisture diffusion in polyimide films in integrated circuits," *J. Electron. Mater.*, vol. 14, no. 2, pp. 119–136, 1985.
[55] P. J. Schubert and J. H. Nevin, "A polyimide-based capacitive humidity sensor," *IEEE Trans. Electron Devices*, vol. ED-32, no. 7, pp. 1220–1223, 1985.
[56] W. A. Clayton, P. J. Freud, and R. D. Baxter, "Contamination resistant capacitive humidity sensor," in *Proc. 1985 Int. Symp. Moisture and Humidity*, pp. 535–544.
[57] R. D. Baxter and P. J. Freud, "Humidity sensing element," U.S. Patent 4 564 882, Jan. 1986.
[58] G. Delapierre, H. Grange, B. Chambaz, and L. Destannes, "Polymer-based capacitive humidity sensor," *Sens. Actuators*, vol. 4, no. 1, pp. 97–104, 1983.
[59] "Polyflon," Polyflon Company, Norwalk, CT, 2000.
[60] A. M. Bishai, A. M. Ghoneim, A. A. M. Ward, and A. F. Younan, "Electrical conductivity of styrene-butadiene rubber/polyester short-fiber reinforced with different types of carbon black," *Polym.—Plastics Technol. Eng.*, vol. 42, no. 4, pp. 701–710, 2003.
[61] N. Dishovsky, F. El Tantawy, and R. Dimitrov, "Effect of bi-containing superconducting ceramic on the volume resistivity of butyl rubber composites," *Polym. Test.*, vol. 23, no. 1, pp. 69–75, 2004.
[62] A. Dhanabalan, J. K. J. van Duren, P. A. van Hal, L. J. van Dongen, and R. A. J. Janssen, "Synthesis and characterization of a low bandgap conjugated polymer for bulk heterojunction photovoltaic cells," *Adv. Funct. Mater.*, vol. 11, no. 4, pp. 255–262, Aug. 2001.
[63] C. Nunes de Carvalho, G. Lavareda, E. Fortunato, and A. Amaral, "Properties of ITO films deposited by R.f.-PERTE on unheated polymer substrates—Dependence on oxygen partial pressure," *Thin Solid Films*, vol. 427, pp. 215–218, 2003.
[64] G. T. A. Kovacs, *Micromachined Transducers Sourcebook*. New York: McGraw-Hill, 1998.
[65] B. Drafts, "Acoustic wave technology sensors," *IEEE Trans. Microwave Theory Tech.*, vol. 49, pp. 795–802, Apr. 2001.
[66] I. E. Kuznetsova, B. D. Zaitsev, S. G. Joshi, and I. A. Borodina, "Investigation of acoustic waves in thin plates of lithium niobate and lithium tantalate," *IEEE Trans. Ultrason., Ferroelect., Freq. Contr.*, vol. 48, pp. 322–328, Jan. 2001.
[67] Y. Jin and S. G. Joshi, "Propagation of a quasi-shear horizontal acoustic wave in Z-X lithium niobate plates," *IEEE Trans. Ultrason., Ferroelect., Freq. Contr.*, vol. 43, pp. 491–494, May 1996.
[68] P. H. Xiang, X. L. Dong, H. Chen, Z. Zhang, and J. K. Guo, "Mechanical and electrical properties of small amount of oxides reinforced PZT ceramics," *Ceram. Int.*, vol. 29, no. 5, pp. 499–503, 2003.
[69] H. Kawai, "The piezoelectricity of polyvinylidene fluoride," *Jpn. J. Appl. Phys.*, vol. 8, no. 7, pp. 975–976, July 1969.
[70] G. Sessler, "What's new in electroacoustic transducers," *IEEE ASSP Mag.*, vol. 1, pp. 3–13, Oct. 1984.
[71] H. Thomann, "Piezoelectric ceramics," *Adv. Mater.*, vol. 2, no. 10, pp. 458–463, Oct. 1990.
[72] M. Madou, *Fundamentals of Microfabrication*, 1st ed. Boca Raton, FL: CRC, 1997.
[73] Z. Surowiai, L. Kozielsei, B. Wodecka-Dus, E. G. Fesenko, O. N. Razumovskaya, L. A. Reznichenko, and I. N. Zakharchenko, "The influence of Pb vacancies on the properties of PZT-type ceramic transducers," *Arch. Acoust.*, vol. 25, no. 2, pp. 251–269, 2000.
[74] H. J. Hwang, M. Yasuoka, M. Sando, M. Toriyama, and K. Niihara, "Fabrication, sinterability, and mechanical properties of lead zirconate titanate/silver composites," *J. Amer. Ceram. Soc.*, vol. 82, no. 9, pp. 2417–2422, 1999.
[75] J. M. Bustillo, R. T. Howe, and R. S. Muller, "Surface micromachining for microelectromechanical systems," *Proc. IEEE*, vol. 86, pp. 1552–1574, Aug. 1998.
[76] A. Haeusler and U. Meyer, "A novel thick film conductive type CO_2 sensor," *Sens. Actuators B, Chem.*, vol. B34, pp. 388–395, Jan. 1996.
[77] N. F. Sheppard Jr, R. C. Tucker, and C. Wu, "Electrical conductivity measurements using microfabricated interdigitated electrodes," *Anal. Chem.*, vol. 65, pp. 1998–2002, May 1993.
[78] M. Nishizawa, T. Matsue, and I. Uchida, "Penicillin sensor based on microarray electrode coated with PH-responsive polypyrrole," *Anal. Chem.*, vol. 64, pp. 2642–2644, 1992.
[79] J. W. Gardner, "Intelligent gas sensing using an integrated sensor pair," *Sens. Actuators B, Chem.*, vol. 26–27, pp. 261–266, 1995.
[80] R. F. Taylor, I. G. Marenchic, and E. J. Cook, "An acetylcholine receptor-based biosensor for the detection of cholinergic agents," *Anal. Chim. Acta*, vol. 213, pp. 131–138, 1988.
[81] "Paratronix," Paratronix, Inc., Attleboro, MA, 1997.
[82] N. F. Sheppard Jr, "Design of a conductimetric microsensor based on reversibly swelling polymer hydrogels," in *Proc. 6th Int. Conf. Solid-State Sensors and Actuators (Transducers'91)*, pp. 773–776.
[83] V. K. Varadan and V. V. Varadan, "Smart electronics with interdigital electrodes, antennas, and MEMS for aerospace structures," in *Proc. Micromachined Devices and Components Conf.*, 1995, pp. 120–124.
[84] V. Tvarozek, I. Novotn, I. Cerven, J. Kova, and T. Lacko, "R. F. reactive sputtering of zinc oxide films on silicon and $Si - SiO_2 - TiN$ substrates," *Sens. Actuators A, Phys.*, vol. 30, pp. 123–127, 1992.
[85] E. S. Kolesar and J. M. Wiseman, "Interdigitated gate electrode field effect transistor for the selective detection of nitrogen dioxide and diisopropyl methylphosphonate," *Anal. Chem.*, vol. 61, pp. 2355–2361, 1989.
[86] M. Hijikigawa, T. Sugihara, J. Tanaka, and M. Watanabe, "Micro-chip FET humidity sensor with a long-term stability," in *Proc. Int. Conf. Solid-State Sensors and Actuators*, 1985, pp. 221–224.
[87] H. E. Endres, S. Drost, and F. Hunter, "Impedance spectroscopy on dielectric gas sensors," *Sens. Actuators B, Chem.*, vol. 22, pp. 7–11, 1994.
[88] R. Zhou, A. Hiermann, K. D. Schierbaum, K. E. Geckeler, and W. Gopel, "Detection of organic solvents with reliable chemical sensors based on cellulose derivatives," *Sens. Actuators B, Chem.*, vol. 24–25, pp. 443–447, 1995.
[89] A. Hierlemann, W. Gopel, J. Mitrovics, S. Schweizer-Berberich, and U. Weimar, "Polymer-based sensor arrays and the multicomponent analysis for the detection of hazardous organic vapors in the environment," *Sens. Actuators B, Chem.*, vol. 26–27, pp. 126–134, 1995.
[90] V. Tvarozek, H. T. Tien, I. Novotn, T. Hianik, J. Dlugopolst, W. Ziegler, A. Leitmannov, J. Jakabovi, V. Rehaucek, and M. Uhl, "Thin-film microsystems applicable in (bio)chemical sensors," *Sens. Actuators B, Chem.*, vol. 18–19, pp. 597–602, 1994.
[91] B. C. Lesieutre, A. V. Mamishev, Y. Du, E. Keskiner, M. Zahn, and G. C. Verghese, "Forward and inverse parameter estimation algorithms of interdigital dielectrometry sensors," *IEEE Trans. Dielect. Elect. Insulation*, vol. 8, no. 4, pp. 577–588, Aug. 2001.
[92] M. S. Tyagi, *Introduction to Semiconductor Materials and Devices*. New York: Wiley, 1991.
[93] G. Huyberechts and L. Frisson, "*In situ* formation of humidity-sensitive devices for the evaluation of solar panel encapsulations," *Sens. Actuators B, Chem.*, vol. 26–27, pp. 308–311, 1995.
[94] A. S. Tenney III, S. V. Silverthorne, and R. D. Baxter, "Integrated microsensors," in *Proc. Process Sensing and Diagnostics, AIChE Symp. Series*, vol. 85, 1989, pp. 14–18.
[95] E. Endres and S. Drost, "Optimization of the geometry of gas-sensitive interdigital capacitors," *Sens. Actuators B, Chem.*, vol. 4, pp. 95–98, 1991.
[96] J. Lin, S. Moller, and E. Obermeier, "Two-dimensional and three-dimensional interdigital capacitors as basic elements for chemical sensors," *Sens. Actuators B, Chem.*, vol. 5, pp. 223–226, 1991.
[97] K. Y. Lee, J. Frost, C. Stanley, W. Patrick, W. S. Mackie, S. P. Beaumont, and D. W. Wilkinson, "Fabrication of ultrasmall devices on thin active GaAs membranes," *J. Vac. Sci. Technol. B, Microelectron. Process. Phenom.)*, vol. 5, no. 1, pp. 322–325, 1988.

[98] S. D. Senturia, "Correlated methods for evaluating polymer properties, interfaces, and adhesion," *Int. J. Microelectron. Packag. Mater. Technol.*, vol. 1, no. 1, pp. 43–50, 1995.
[99] S. D. Senturia and S. L. Garverick, "Method and apparatus for microdielectrometry," U.S. Patent 4 423 371, Dec. 1983.
[100] V. K. Varadan and V. V. Varadan, "Smart electronics and sensors for IVHS and automobile collision warning antenna systems," in *Proc. Micromachined Devices and Components Conf.*, 1995, pp. 120–124.
[101] F. W. Smith, H. J. Neuhaus, S. D. Senturia, Z. Feit, D. R. Day, and T. J. Lewis, "Electrical conduction in polyimide between 20 and 350 °C," *J. Electron. Mater.*, vol. 16, no. 1, pp. 93–106, 1987.
[102] F. Bellucci, I. Khamis, S. D. Senturia, and R. M. Latanision, "Moisture effects on the electrical conductivity of Kapton polyimide," *J. Electrochem. Soc.*, vol. 137, no. 6, pp. 1778–1784, 1990.
[103] A. V. Mamishev, M. Zahn, B. C. Lesieutre, and B. A. Berdnikov, "Influence of geometric parameters on characteristics of an interdigital sensor," in *Proc. IEEE Conf. Electrical Insulation and Dielectric Phenomena*, 1996, pp. 550–553.
[104] V. Shtrauss, A. Kalpinsh, U. Lomanovskis, and J. Rotbahs, "Tomographic imaging by electrical methods," *Latvian J. Phys. Tech. Sci.*, no. 3, pp. 23–47, 1995.
[105] I. C. Shay and M. Zahn, "Cylindrical geometry electroquasistatic dielectrometry sensors," in *Proc. IEEE Conf. Electrical Insulation and Dielectric Phenomena*, 2002, pp. 126–129.
[106] J. S. Kim and D. G. Lee, "Analysis of dielectric sensors for the cure monitoring of resin matrix composite materials," *Sens. Actuators B, Chem.*, vol. B30, no. 2, pp. 159–164, Jan. 1996.
[107] M. Zahn, *Electromagnetic Field Theory: A Problem Solving Approach*. Malabar, FL: Krieger, 2003.
[108] A. Leyk and E. Kubalek, "MMIC internal electric field mapping with submicrometer spatial resolution and gigahertz bandwidth by means of high frequency scanning force microscope testing," *Electron. Lett.*, vol. 31, no. 24, pp. 2089–2091, 1995.
[109] H. L. Lee, "Optimization of a resin cure sensor," Ph.D. dissertation, Dept. Elect. Eng. Comput. Sci., Massachusetts Inst. Technol., Cambridge, 1982.
[110] P. C. Kohnke and C. Rajakumar, "General-purpose finite-element software for fluid-structure analysis," *Int. J. Comput. Appl. Technol.*, vol. 5, pp. 199–207, 1992.
[111] K. Nabors, S. Kim, J. White, and S. Senturia, "Fast capacitance extraction of general three-dimensional structures," in *Proc. IEEE Int. Conf. Computer Design: VLSI in Computers and Processors*, 1991, pp. 479–484.
[112] R. Y. Scapple, "A trimmable planar capacitor for hybrid applications," in *Proc. 24th Electronic Components Conf*, 1974, pp. 203–207.
[113] B. Diem, P. Rey, S. Renard, S. V. Bosson, H. Bono, F. Michel, M. T. Delaye, and G. Delapierre, "SOI 'SIMOX'; from bulk to surface micromachining, a new age for silicone sensors and actuators," *Sens. Actuators A, Phys.*, vol. 46–47, pp. 8–16, 1995.
[114] W. C. Tang, M. G. Lim, and R. T. Howe, "Electrostatic comb drive levitation and control method," *J. Microelectromech. Syst.*, vol. 1, pp. 170–178, Dec. 1992.
[115] C. T. William, T. H. Nguyen, and T. H. Roger, "Laterally driven polysilicon resonant microstructures," *Sens. Actuators*, vol. 20, pp. 25–32, 1989.
[116] C. Campbell, *Surface Acoustic Wave Devices and Their Signal Processing Applications*. New York: Academic, 1989.
[117] D. Vadasz and I. Sebestyen, "Comparison of the Newton–Raphson and the spectral expansion impedance tomography reconstruction algorithms," *IEEE Trans. Magn.*, vol. 32, pp. 1286–1289, May 1996.
[118] S. D. Senturia, N. F. Sheppard, Jr., H. L. Lee, and D. R. Day, "In-situ measurement of the properties of curing systems with microdielectrometry," *J. Adhesion*, vol. 15, no. 69, pp. 69–90, 1982.
[119] N. T. Smith and D. D. Shepard, "Dielectric cure analysis: theory and industrial applications," *Sensors*, vol. 12, no. 10, pp. 42–48, Oct. 1995.
[120] G. Niebling and A. Schlachter, "Qualitative and quantitative gas analysis with nonlinear interdigital sensor arrays and artificial neural networks," *Sens. Actuators B, Chem.*, vol. B26–B27, pp. 289–292, 1995.
[121] A. Washabaugh, A. V. Mamishev, Y. Du, and M. Zahn, "Dielectric measurements of semi-insulating liquids and solids," in *Proc. Int. Conf. Conduction and Breakdown in Dielectric Liquids*, 1996, pp. 381–384.
[122] E. Endres, W. G. Ottler, H. D. Jander, S. Drost, and G. Sberveglieri, "Improvements in signal evaluation techniques for semiconductor gas sensors," *Sens. Actuators B, Chem.*, vol. 27, pp. 267–270, 1995.
[123] J. Pichlmaier, "Compensation of the influence of humidity on the measurement of an SO_2 sensor by signal processing," *Sens. Actuators B, Chem.*, vol. 26–27, pp. 286–288, 1995.
[124] B. Denise and P. D. Stephen, "Smart chemical sensing arrays using tin oxide sensors and analog winner-take-all signal processing," *Sens. Actuators B, Chem.*, vol. 26–27, pp. 271–274, 1995.
[125] T. M. Davidson and S. D. Senturia, "The moisture dependence of the electrical sheet resistance of aluminum oxide thin films with application to integrated moisture sensors," in *Proc. Int. Reliability Physics Symp. 20th Annual Proc.*, 1982, pp. 249–252.
[126] S. L. Garverick and S. D. Senturia, "An MOS device for AC measurement of surface impedance with application to moisture monitoring," *IEEE Trans. Electron Devices*, vol. ED-29, no. 1, pp. 90–101, Jan. 1982.
[127] D. D. Denton, S. D. Senturia, E. S. Anolick, and D. Scheider, "Fundamental issues in the design of polymeric capacitive moisture sensors," in *Proc. Transducers: Int. Conf. Solid-State Sensors and Actuators*, 1985, pp. 202–205.
[128] C. W. Coln and S. D. Senturia, "The application of linear system theory to parametric microsensors," in *Proc. Transducers '85 Int. Conf. Solid-State Sensors and Actuators*, pp. 118–121.
[129] D. R. Day and D. D. Shepard, "Dynamic cure and diffusion monitoring in thin encapsulant films," in *Proc. Nondestructive Monitoring of Materials Properties Symp.*, 1988, pp. 227–232.
[130] D. R. Day, D. D. Shepard, and K. J. Craven, "A microdielectric analysis of moisture diffusion in thin epoxy/amine films of varying cure state and mix ratio," *Polym. Eng. Sci.*, vol. 32, no. 8, pp. 524–528, Apr. 1992.
[131] P. D. Aldrich, S. K. Thurow, M. J. M. Kennon, and M. E. Lyssy, "Dielectric relaxation due to absorbed water in various thermosets," *Polymer*, vol. 28, pp. 2289–2296, Dec. 1987.
[132] J. Crank, *The Mathematics of Diffusion*. Oxford, U.K.: Clarendon, 1956.
[133] R. K. Ralston, C. F. Klein, P. E. Thoma, and D. D. Denton, "A model for the relative environmental stability of a series of polyimide capacitance humidity sensors," *Sens. Actuators B, Chem.*, vol. B34, no. 1–3, pp. 343–348, Aug. 1996.
[134] N. F. Sheppard Jr, S. L. Garverick, D. R. Day, and S. D. Senturia, "Microdielectrometry: a new method for *in situ* cure monitoring," in *Proc. 26th SAMPE Symp.*, 1981, pp. 65–76.
[135] K. S. Cole and R. H. Cole, "Dispersion and absorption in dielectrics," *J. Chem. Phys.*, vol. 9, no. 4, pp. 341–351, Apr. 1941.
[136] S. D. Senturia, N. F. Sheppard Jr, H. L. Lee, and S. B. Marshall, "Cure monitoring and control with combined dielectric/temperature probes," in *Proc. 28th SAMPE Symp.*, 1983, pp. 851–861.
[137] P. Debye, *Polar Molecules*. New York: Chemical Catalog, 1929.
[138] N. F. Sheppard Jr, M. Colin, and S. D. Senturia, "A dielectric study of the time-temperature transformation (TTT) diagram of DGEBA epoxy resins cured with DDS," in *Proc. 29th SAMPE Symp.*, 1984, pp. 1243–1250.
[139] D. E. Kranbuehl, S. E. Delos, P. K. Jue, T. P. Jarvie, and S. A. Williams, "Dynamic dielectric characterization of thermosets and thermoplastics using intrinsic variables," in *Proc. 29th SAMPE Symp.*, 1984, pp. 1251–1257.
[140] M. L. Bromberg, D. D. Day, and K. R. Snable, "Measurement and application of dielectric properties," *IEEE Electr. Insul. Mag.*, vol. 2, pp. 18–23, May 1986.
[141] D. R. Day, T. J. Lewis, H. L. Lee, and S. D. Senturia, "The role of boundary layer capacitances at blocking electrodes in the interpretation of dielectric cure data in adhesives," *J. Adhesion*, pp. 73–90, 1984.
[142] P. A. von Guggenberg, "Experimental investigation of the heterogeneity of the double layer in transformer oil," in *Proc. Conf. Electrical Insulation and Dielectric Phenomena*, 1993, pp. 68–73.
[143] T. Lang, D. Wiemh, and W. G. Opel, "Carbonate based CO_2 sensors with high performance," *Sens. Actuators B, Chem.*, vol. B34, no. 2, pp. 382–387, Jan. 1996.
[144] K. D. Schierbaum, J. Geiger, U. Weimar, and W. G. Opel, "Specific palladium and platinum doping for SnO_2 based thin film sensor arrays," *Sens. Actuators B, Chem.*, vol. 13–14, pp. 143–147, 1993.
[145] K. Higaki, S. Kudo, and H. Ohnishi, "Highly selective NO detection using Bi_2O_3 based materials," *Electrochem. Solid-State Lett.*, vol. 1, no. 2, pp. 107–109, 1998.

[146] L. E. Diane, R. Z. Mitchell, L. S.Lawrence S. Bernstein, and F. R. Michael, "Conductive polymer films as ultrasensitive chemical sensors for hydrazine and monomethylhydrazine vapor," *Anal. Chem.*, vol. 68, no. 5, p. 817, Mar. 1996.
[147] D. C. Cullen, R. S. Sethi, and C. R. Lowe, "Multi-analyte miniature conductance biosensor," *Analytica Chimica Acta*, vol. 231, pp. 33–40, 1990.
[148] R. Feinman, "Infinitesimal machinery," *J. Microelectromech. Syst.*, vol. 2, pp. 170–178, Mar. 1993.
[149] J. Fluitman, "Microsystems technology: Objectives," *Sens. Actuators A, Phys.*, vol. 56, pp. 423–430, 1996.
[150] A. B. Frazier, R. O. Warrington, and C. Friedrich, "The miniaturization technologies: Past, present, and future," *IEEE Trans. Ind. Electron.*, vol. 42, pp. 423–430, Oct. 1995.
[151] S. D. Senturia, "The future of microsensor and microactuator design," *Sens. Actuators A, Phys.*, vol. 56, pp. 151–166, Mar. 1996.
[152] V. K. Varadan, V. V. Varadan, and X. Q. Bao, "Integration of interdigital transducers, MEMS and antennas for smart structures," in *Proc. Smart Electronics and MEMS Conf.*, 1996, pp. 95–106.
[153] H. Kahn, S. Stemmer, K. Nandakumar, A. H. Heuer, R. L. Mullen, and R. Ballarini, "Mechanical properties of thick, surface micromachined polysilicon films," in *Proc. Micro Electro Mechanical Systems (MEMS '96)*, pp. 343–348.
[154] C. T. William, H. N. Tu-chong, W. J. Michael, and T. H. Roger, "Electrostatic-comb drive of lateral polysilicon resonators," *Sens. Actuators*, vol. 21, pp. 328–331, 1990.
[155] S. Kumar, D. Cho, and W. N. Carr, "A proposal for electrically levitating micromotors," *Sens. Actuators A, Phys.*, vol. 24, pp. 141–149, 1990.
[156] M. Mehregany, P. Nagarkar, S. D. Senturia, and J. H. Lang, "Operation of micro-fabricated harmonic and ordinary side-drive motors," in *Proc. IEEE Micro Electro Mechanical Systems Workshop*, 1990, pp. 1–8.
[157] S. F. Bart, T. A. Lobar, R. T. Howe, J. H. Lang, and M. F. Schlecht, "Design considerations for micromachined electric actuators," *Sens. Actuators*, vol. 14, pp. 269–292, 1988.
[158] M. G. Lim, J. C. Chang, D. P. Schultz, R. T. Howe, and R. M. White, "Polysilicon micro-structures to characterize static friction," in *Proc. IEEE Micro Electro Mechanical Systems Workshop*, 1990, pp. 82–88.
[159] C. J. Kim, A. P. Pisano, R. S. Muller, and M. G. Lim, "Polysilicon microgripper," in *Tech. Dig. IEEE Solid-State Sensor and Actuator Workshop*, 1990, pp. 48–51.
[160] J. Yun, R. T. Howe, and P. R. Gray, "Surface micromachined, digitally force-balanced accelerometer with integrated CMOS detection circuitry," in *Tech. Dig. IEEE Solid-State Sensor and Actuator Workshop*, 1992, pp. 126–131.
[161] M. J. Daneman, N. C. Tien, O. Solgaard, A. P. Pisano, K. Y. Lau, and R. S. Muller, "Linear microvibromotor for positioning optical components," *J. Microelectromech. Syst.*, vol. 5, pp. 159–165, Sept. 1996.
[162] M. A. Haque and T. A. Saif, "Microscale materials testing using MEMS actuators," *J. Microelectromech. Syst.*, vol. 10, pp. 146–152, 2001.
[163] R. I. Pratt, G. C. Johnson, R. T. Howe, and J. C. Chang, "Micromechanical structures for thin film characterization," in *Proc. Int. Conf. Solid-State Sensors and Actuators (Transducers '91)*, pp. 205–208.
[164] B. Ha, Y. Oh, B. Lee, K. Y. Park, S. Baek, S. Ann, C. Song, and J. Lee, "A area variable capacitive microaccelerometer with force-balancing electrodes," in *Proc. IEEE 1998 Position Location and Navigation Symp.*, pp. 146–151.
[165] K. Asano, F. Hatakeyama, and K. Yatsuzuka, "Fundamental study of an electrostatic chuck for silicon wafer handling," in *Proc. Industry Applications Conf. 1997 32nd IAS Annu. Meeting*, vol. 3, pp. 1998–2003.
[166] P. Hartemann and E. Dieulesaint, "Acoustic surface-wave filters," *Electron. Lett.*, vol. 5, pp. 657–658, 1969.
[167] F. S.Fred S. Hickernell, "Surface acoustic wave devices: A rewarding past, a significant present, and a promising future," in *Proc. 12th Int. Conf. Microwaves and Radar*, vol. 4, 1998, pp. 159–168.
[168] D. P. Morgan, *Key Papers on Surface-Acoustic-Wave Passive Interdigital Devices*. Stevenage, U.K.: Peregrinus, 1976.
[169] D. W. Galipeau, J. F. Vetelino, and C. Feger, "Adhesion studies of polyimide films using a surface acoustic wave sensor," *J. Adhesion Sci. Technol.*, vol. 7, no. 12, pp. 1335–1345, 1993.
[170] G. Hayward, A. McNab, A. Gachagan, R. Farlow, B. Hailu, D. Atkinson, D. Girma, G. Smith, and S. Whiteley, "Embedded ultrasonic sensors for monitoring structural integrity," in *Proc. AIP Conf.*, 2001, pp. 1771–1778.
[171] K. Toda and A. Sawaguchi, "Ultrasonic system for detecting defects in IC package using leaky lamb wave device," *Nondestruct. Test. Eval. Int.*, vol. 10, no. 2, pp. 137–144, 1992.
[172] B. Chenni and J. Pouliquen, "Non-destructive evaluation of gradient properties of hardened steel by surface acoustic waves measurements," in *Proc. AIP Conf.*, 2002, pp. 1629–1636.
[173] S. P. Joshi, "Feasibility study on phased array of interdigital mesoscale transducers for health monitoring of smart structures," *Proc. SPIE*, vol. 2443, pp. 248–257, 1995.
[174] K. Toda, "Characteristics of interdigital transducers for mechanical sensing and nondestructive testing," *Sens. Actuators A, Phys.*, vol. A44, no. 3, pp. 241–247, Sept. 1994.
[175] T. Nomura, M. Wayashi, and T. Yasuda, "Measurement of SAW velocity using impulse system and its application on NDE," in *Proc. 1996 IEEE Int. Frequency Control Symp.*, pp. 296–299.
[176] H. Cho, S. Ogawa, and M. Takemoto, "Non-contact laser ultrasonics for detecting subsurface lateral defects," *Nondestruct. Test. Eval. Int.*, vol. 29, no. 5, pp. 301–306, 1996.
[177] S. A. Sakharov, A. N. Zabelin, O. A. Buzanov, A. V. Medvedev, V. V. Alenkov, S. N. Kondratiev, and S. A. Zhgoon, "Nondestructive investigation of 4-inch langasite wafer acoustic homogeneity," in *Proc. 2002 IEEE Ultrasonics Symp.*, vol. 1, pp. 227–230.
[178] R. S. C. Monkhouse, P. D. Wilcox, and P. Cawley, "Flexible interdigital PVDF transducers for the generation of lamb waves in structures," *Ultrasonics*, vol. 35, no. 7, pp. 489–498, Nov. 1997.
[179] H. Luo and S. Hanagud, "PVDF film sensor and its applications in damage detection," *J. Aerosp. Eng.*, vol. 12, no. 1, pp. 23–30, 1999.
[180] K. Toda, "Characteristics of interdigital transducers for mechanical sensing and nondestructive testing," *Sens. Actuators A, Phys.*, vol. A44, no. 3, pp. 241–247, Sept. 1994.
[181] R. S. C. Monkhouse, P. D. Wilcox, and P. Cawley, "Flexible interdigital PVDF transducers for the generation of lamb waves in structures," *Ultrasonics*, vol. 35, no. 7, pp. 489–498, Nov. 1997.
[182] D. N. Alleyne and P. Cawley, "Optimization of lamb wave inspection techniques," *Nondestruct. Test. Eval. Int.*, vol. 25, no. 1, pp. 11–22, 1992.
[183] R. S. C. Monkhouse, P. D. Wilcox, and P. Cawley, "Flexible interdigital PVDF transducers for the generation of lamb waves in structures," *Ultrasonics*, vol. 35, no. 7, pp. 489–498, Nov. 1997.
[184] J. W. Gardner, A. Pike, N. F. de Rooij, M. Koudelka-Hep, P. A. Clerc, A. Hierlemann, and W. G. Opel, "Integrated array sensor for detecting organic solvents," *Sens. Actuators B, Chem.*, vol. 26–27, pp. 135–139, 1995.
[185] V. J. Lumelsky, M. S. Shur, and S. Wagner, "Sensitive skin," *IEEE Sensors J.*, vol. 1, pp. 41–51, Mar. 2001.
[186] B. J. Kane, M. R. Cutkosky, and G. T. A. Kovacs, "A traction stress sensor array for use in high-resolution robotic tactile imaging," *J. Microelectromech. Syst.*, vol. 9, pp. 425–434, Dec. 2000.
[187] H. Martin, S. Uwe, K. Hermann, Z. Johannes, and B. Josef, "Air monitoring by a combined resistive and field effect sensor device," in *Proc. 1997 Int. Conf. Solid-State Sensors and Actuators*, 1997, p. 963.
[188] R. S. C. Monkhouse, P. D. Wilcox, M. J. S. Lowe, R. P. Dalton, and P. Cawley, "The rapid monitoring of structures using interdigital lamb wave transducers," *Smart Mater. Struct.*, vol. 9, no. 3, pp. 304–309, June 2000.
[189] T. Liu, M. Veidt, and S. Kitipornchai, "Single mode lamb waves in composite laminated plates generated by piezoelectric transducers," *Composite Struct.*, vol. 58, no. 3, pp. 381–396, Nov. 2002.
[190] H. Subramanian, V. V. Varadan, and V. K. Varadan, "Wireless remotely readable microaccelerometer," in *Proc. Smart Electronics and MEMS Conf.*, 1997, pp. 220–228.
[191] V. V. Varadan, V. K. Varadan, S. Ramanathan, and D. Piscotty, "Wireless passive IDT strain microsensor [and helicopter blade control application]," *Smart Mater. Struct.*, vol. 6, no. 6, pp. 745–751, Dec. 1997.
[192] J. P. Runt and J. J. Fitzgerald, Dielectric Spectroscopy of Polymeric Materials: Fundamentals and Applications, Amer. Chem. Soc., Washington, DC, ser. ACS Professional Reference Series, 1997.
[193] Dielectrics Newsletter (2001, Sept.). [Online]. Available: http://www.novocontrol.com
[194] *Parylene Conformal Coatings Specifications and Properties*, Specialty Coating Systems, Inc., Indianapolis, IN, 1994.

Alexander V. Mamishev (Member, IEEE) received the B.S. degree (equivalent certificate) in electrical engineering from the Kiev Polytechnic Institute, Kiev, Ukraine, in 1992, the M.S. degree in electrical engineering from Texas A&M University, College Station, in 1994, and the Ph. D. degree in electrical engineering from Massachusetts Institute of Technology, Cambridge, in 1999.

He is currently Director of the Sensors, Energy, and Automation Laboratory (SEAL), Department of Electrical Engineering, University of Washington, Seattle. He is the author of one book chapter, about 60 journal and conference papers, and one patent. His research interests include sensor design and integration, dielectrometry, electric power applications, bioengineering, MEMS, and robotics.

Prof. Mamishev is a recipient of the National Science Foundation CAREER Award, the IEEE Outstanding Branch Advisor Award, and the University of Washington EE Outstanding Research Advisor Award. He serves as an Associate Editor for the IEEE TRANSACTIONS ON DIELECTRICS AND ELECTRICAL INSULATION.

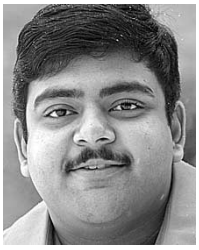

Kishore Sundara-Rajan (Student Member, IEEE) received the B.Eng. degree in electrical and electronics engineering from the University of Madras, Chennai, India, in 2001 and the M.S. degree in electrical engineering from the University of Washington, Seattle, in 2003.

Since 2002, he has been a Graduate Research Assistant at the Sensors, Energy, and Automation Laboratory (SEAL), Department of Electrical Engineering, University of Washington. His research interests include sensor design and integration, on-chip power scavenging, RFID, MEMS, and dielectric spectroscopy.

Mr. Sundara-Rajan is a recipient of the IEEE Dielectrics and Electrical Insulation Society's Graduate Fellowship. He is also a reviewer for IEEE SENSORS JOURNAL.

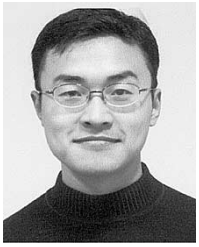

Fumin Yang (Student Member, IEEE) received the B.S. degree in polymer science and engineering from the University of Science and Technology of China (USTC), Hefei, in 2000 and the M.S.E.E. degree from the University of Washington, Seattle, in 2002. He is currently working toward the Ph.D. degree in electrical engineering at the University of Washington.

His research interests include sensors, optoelectronics, device physics, device modeling, and fabrication.

Yanqing Du (Member, IEEE) received the B.S. and M.E. degrees in electrical engineering from Northwestern Polytechnical University, China, in 1993 and 1994, respectively, and the E.E. and Ph.D. degrees in electrical engineering from MIT in 1999.

She was a consultant in the analysis and prevention of failures at Exponent Failure Analysis Associates. She is currently a Senior Project Engineer at Underwriters Laboratories, Santa Clara, CA, specializing in product safety and compliance issues. She has published over 24 papers in professional conferences and archival journals, including award papers and invited lectures. Her professional interests and areas of expertise include electrical insulation, thermistor-type devices, moisture dynamics in power equipment insulation, and failure analysis and prevention for electronics and electrical equipment.

Dr. Du is a Member of Sigma Xi. She is a Registered Professional Engineer in the state of California.

Markus Zahn (Fellow, IEEE) received the B.S.E.E., M.S.E.E., Electrical Engineer, and Sc.D. degrees from the Massachusetts Institute of Technology (MIT), Cambridge, MA, in 1968, 1968, 1969, and 1970, respectively.

Since 1980, he has been on the faculty of MIT, where he is currently a Professor of Electrical Engineering. He works in the Laboratory for Electromagnetic and Electronic Systems and in the MIT High Voltage Research Laboratory. He is also the Director of the MIT Course VI-A Electrical Engineering and Computer Science Internship Program, a cooperative work/study program with industry. He is the author of *Electromagnetic Field Theory: A Problem Solving Approach* (Malabar, FL: Krieger, 2003) and has codeveloped a set of educational videotapes on demonstrations of electromagnetic fields and energy. His broad areas of interest concern electromagnetic field interactions with materials.

Prof. Zahn has received numerous awards for excellence in teaching. He was the 1998 J.B. Whitehead Memorial Lecturer, and was the First James R. Melcher Memorial Lecturer in 2003. He is active in the IEEE Dielectrics and Electrical Insulation Society.